ISSN 1732-9353 (suspended)
eISSN 2543-7496

Scientific Review

Engineering and Environmental Sciences

Przegląd Naukowy
Inżynieria i Kształtowanie Środowiska

Vol. 32 (1) 2023 Issue 99
Quarterly

SCIENTIFIC REVIEW
ENGINEERING AND ENVIRONMENTAL SCIENCES
Quarterly

EDITORIAL OFFICE ADDRESS
Wydział Budownictwa i Inżynierii Środowiska SGGW, ul. Nowoursynowska 159, 02-776 Warsaw, Poland
tel. (+48 22) 59 35 363, 59 35 210, 59 35 302
e-mail: srees@sggw.edu.pl
https://srees.sggw.edu.pl

Electronic version of the Scientific Review Engineering and Environmental Sciences is primary version

All papers are indexed in the data bases as follows: AGRO(Poznań), BazTech, Biblioteka Nauki, **CrossRef**, **DOAJ**, **Google Scholar**, **Index Copernicus**, INFONA, POL-Index, **SCOPUS**, SIGŻ(CBR)

Scientific Review

Engineering and Environmental Sciences

Przegląd Naukowy

Inżynieria i Kształtowanie Środowiska

Vol. 32 (1) 2023 Issue 99

Contents

Wydawnictwo SGGW, Warsaw 2023

Wydawnictwo SGGW wydawnictwosggw

Editorial work – Anna Dołomisiewicz, Violetta Kaska

ISSN 1732-9353 (suspended) eISSN 2543-7496

Scientific Review Engineering and Environmental Sciences (2023), 32 (1), 3–17

Sci. Rev. Eng. Env. Sci. (2023), 32 (1) https://srees.sggw.edu.pl

ISSN 1732-9353 (suspended) eISSN 2543-7496 DOI 10.22630/srees.4535

Received: 26.10.2022
Accepted: 11.12.2022

Shahzinan J. ZAEZUE[1]✉ https://orcid.org/0000-0001-6376-724X

Waleed K. HADI[2]

[1]University of Thi-Qar, College of Engineering, 64001, Iraq
[2]Mazaya University College, Civil Engineering Department, Iraq

Effect of hybrid steel-polypropylene fiber on punching shear behavior of flat slab with an opening

Keywords: hybrid fiber, steel fiber, polypropylene fiber, punching shear, slab with opening

Introduction

Plain concrete is prone to punching failures because of its low tensile strength, poor toughness, low flexural strength, low shear strength and brittle nature (Barrera, Bonet, Romero & Miguel, 2011; Gu, Wu, Wu & Wu, 2012). Slab collapse, and particularly flat slab collapse when supported by columns, is typically attributed to a punching failure. Such failures occur in the slabs with little to no notice before they collapse, and they are frequently accompanied by bending, cracking and pronounced fluctuations in the post-peak behavior as a result of a decrease in the load following the peak stress point (Di Prisco & Felicetti, 1997). Standard practice calls for placing transverse stirrups at close intervals to strengthen concrete confinement, slowing the spread of cracks and improving the punching shear performance of reinforced concrete slabs (Paulay & Priestley, 1993; American Concrete Institution [ACI], 2005).

✉shazanan.j.z@utq.edu.iq

Fiber-reinforced concrete has become an innovative reinforcement option since the 1960s, when it started to replace the more traditional reinforcement approach of using stirrups. In order to prevent bond failure in extremely stressed areas of a structure (such as beam-column joints, column bases and beam midspans), fiber--reinforced concrete (FRC) has been widely adopted as a preventative measure (Mansour, Bakar, Ibrahim, Marsono & Marabi, 2015).

Due to its low cost, exceptional toughness and higher shrinkage cracking strength in concrete reinforced with this type of fiber (Alhozaimy, Soroushian & Mirza, 1996; Qian & Stroeven, 2000; Banthia & Gupta, 2006), polypropylene, the most common synthetic fiber, has received the most interest among the researchers. Though steel fiber has had numerous applications in the past few decades thanks to its ability to improve the performance of structural parts, new research is looking into the usage of fiber combinations in the cementitious composite. The primary objective of this multi-fiber approach is to minimize cracking in cementitious materials throughout a wide range of loading conditions and strain amplitudes (Brandt, 2008; Issa, Metwally & Elzeiny, 2011; Banthia, Majdzadeh, Wu & Bindiganavile, 2014; Chi, Xu & Yu, 2014). Steel-polypropylene hybrid fibers were conceptualized to combine the benefits of both fiber forms. In a hybrid fiber system, stronger steel fibers increase the ultimate strength and first crack stress, while flexible and ductile polypropylene fibers increase the ductility and toughness after cracking (Yao, Li & Wu, 2003). Numerous studies (Dry, 1994; Sivakumar, 2011; Xu, Xu, Chi & Zhang, 2011; Chi, Xu, Mei, Hu & Su, 2014; Afroughsabet & Ozbakkaloglu, 2015) have pointed out the benefits of combining steel with polypropylene fibers. Xu et al. (2011) observed the steel-polypropylene FRC's tensile strength. Their research revealed that the use of hybrid steel-polypropylene fibers can significantly increase the tensile strength of conventional concrete.

Sivakumar (2011) examined the toughness, ductility and flexural strength of a concrete specimen made up of combinations of hybrid polypropylene fibers and steel fibers, and found comparable findings.

Chi et al. (2014) studied the effects of the tri axial compression with steel-polypropylene hybrid fiber reinforced concrete (HFRC). The results revealed that the steel fibers, the triaxial strength of which significantly increased with the increase of the steel fiber volume fractions, were the primary contributors to the composite's improved strength.

Labib (2020) presented an experimental study to estimate the influence of the steel-polypropylene hybrid fiber on the punching shear capacity. The test results revealed that the hybrid fiber concrete mixtures have outdone normal and single fiber concrete mixtures in terms of punching shear capacity. Other concrete proprieties, such as compressive strength, flexural strength, cracking behavior, ductility and toughness, have also shown this improvement.

So far, no research has been conducted into the potential benefits of hybrid steel--polypropylene mixes in increasing the punching shear capacity of slab with opening.

This research aimed to quantify the influence of steel-polypropylene HFRC on improving the punching shear capacity of concrete slabs and to discuss the influence of fiber volume fraction on punching shear.

Material and methods

All slabs were reinforced with deformed bars in conformity with the ASTM A615/A615M-15a standard (ASTM International [ASTM], 2015) with a 10 mm diameter for flexural reinforcement. Hooked-end steel and polypropylene fibers were used in this study as shown in Figure 1. The properties of the steel reinforcement and the fiber are listed in Table 1. The usage of sulfate-resistant portland cement type (V) in conformity with to the ASTMC150/C150M-21 standard (ASTM, 2021) was required. In order to make the material more workable, high--range water-reducing Sika® ViscoCrete®-5930 super plasticizer (SP) consistent with the requirements of the ASTM C494/C494M-19 standard (ASTM, 2019) was used. In this study, the coarse aggregate that complied with the ASTM C33/ /C33M-13 standard (ASTM, 2013) and sand with a maximum size of 4.75 mm each were used. The materials were tested at the Labs of the College of Engineering – University of Thi-Qar. A steel reinforcement bar was placed horizontally inside the molds before pouring the concrete mixture into them. All samples were covered with a wet blanket for 28 days for curing after 48 h of casting.

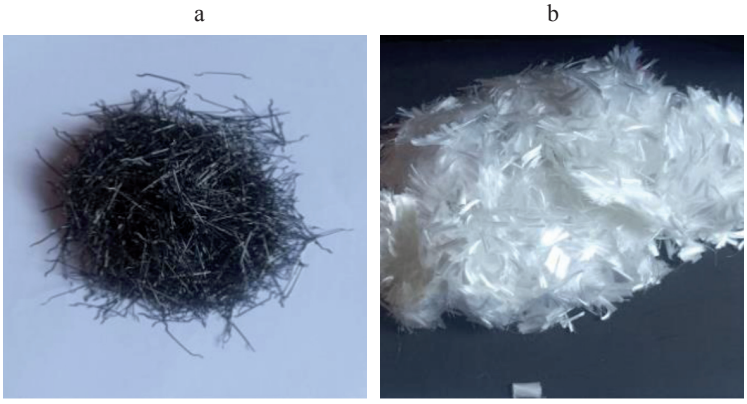

FIGURE 1. Types of fibers: a – steel fiber; b – polypropylene fiber
Source: own work.

TABLE 1. Steel reinforcement bar and fibers properties

Material	Property	Value/Description
Steel bar	Bar diameter [mm]	10
	Yield stress [MPa]	550
	Ultimate stress [MPa]	643
	Elongation [%]	11.87
Steel fiber	Length [mm]	30
	Diameter [mm]	0.5
	Aspect ratio length to diameter (L/D)	60
	Geometry	hooked-ends
	Tensile strength [MPa]	1 300
Polypropylene (PPF)	Length [mm]	12
	Diameter [mm]	0.032
	Aspect ratio length to diameter (L/D)	375
	Geometry	straight
	Tensile strength [MPa]	600–700

Source: manufacturers' specifications.

Mix designs

The reference mixture was intended to have a cube compressive strength of 35 MPa, in accordance with the BS 1881-116 standard (British Standards Institution [BSI], 1991). Each sample mix design is differentiated from the others using a different volumetric ratio of hybrid fibers. The workability of fiber reinforcement concrete mixtures was improved by using super plasticizers, a water-reducing addition. Table 2 lists the mix proportions that were employed in this study. All components were combined in a concrete mixer for around 10 min.

TABLE 2. Details of mix proportions

Mix	Cement content [kg·m^{-3}]	Sand content [kg·m^{-3}]	Coarse aggregate content [kg·m^{-3}]	Water content [kg·m^{-3}]	Super plasticizers content (by weight of cement) [%]	Steel fiber content [%]	Polypropylene fiber content [%]
S1	410	750	1 100	184.5	0.5	0	0
S2	410	750	1 100	184.5	0.5	0.75	0.15
S3	410	750	1 100	184.5	0.5	0.75	0.3
S4	410	750	1 100	184.5	0.5	1.5	0.15
S5	410	750	1 100	184.5	0.5	1.5	0.3

Source: own work.

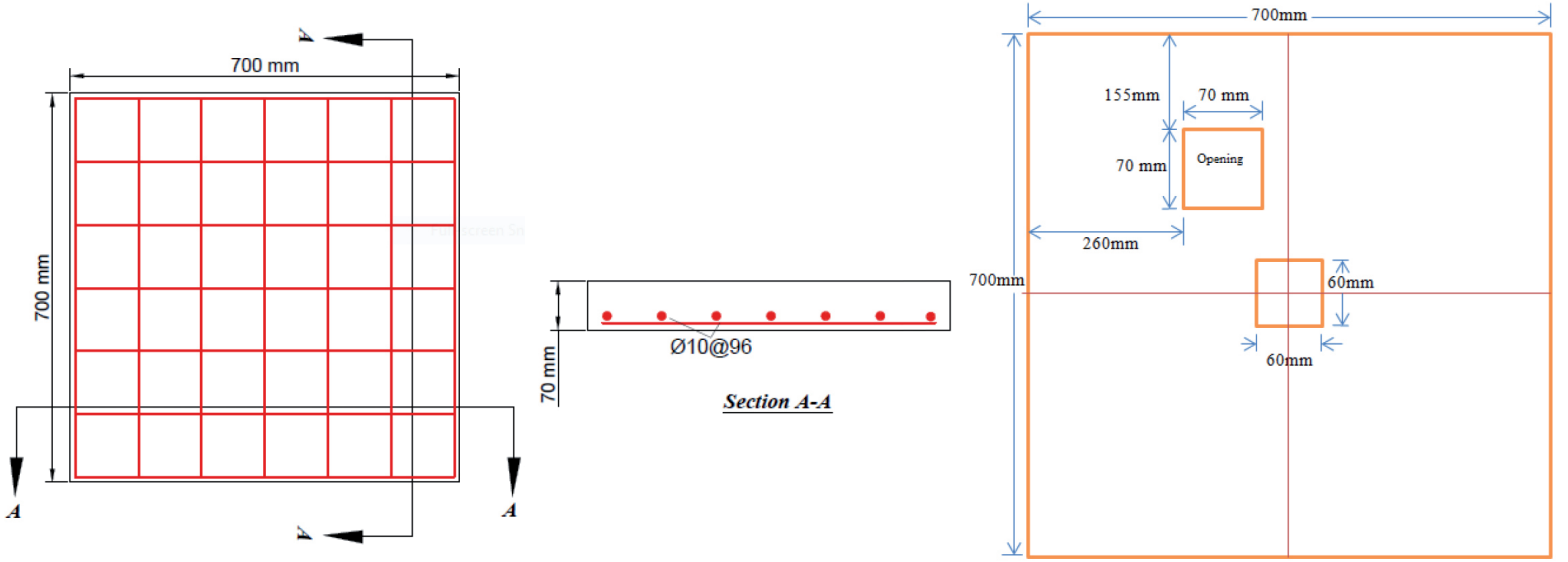

FIGURE 2. Details of reinforcement and specimen opening layouts

Source: own work.

Sample preparation

The dimensions of slab specimens were 700 × 700 × 70 mm. They were reinforced with Ø10 in both directions (seven bars in each direction) with the 15 mm concrete cover. The slab supported by a steel frame (600 × 600 mm) provided a 700 mm clear span in two directions. Figure 2 depicts the geometry and reinforcement of the slab sample. The slab had an opening (70 × 70 mm) at the panel corner as shown in Figure 2. The loads were applied on a solid square steel shaft (60 × 60 mm) at the center. A single dial gauge was used to measure the deflection at the center point of the slabs. Figure 3 displays the molds before casting concrete, the machine of applied load, the frame support of the slab and dial gage.

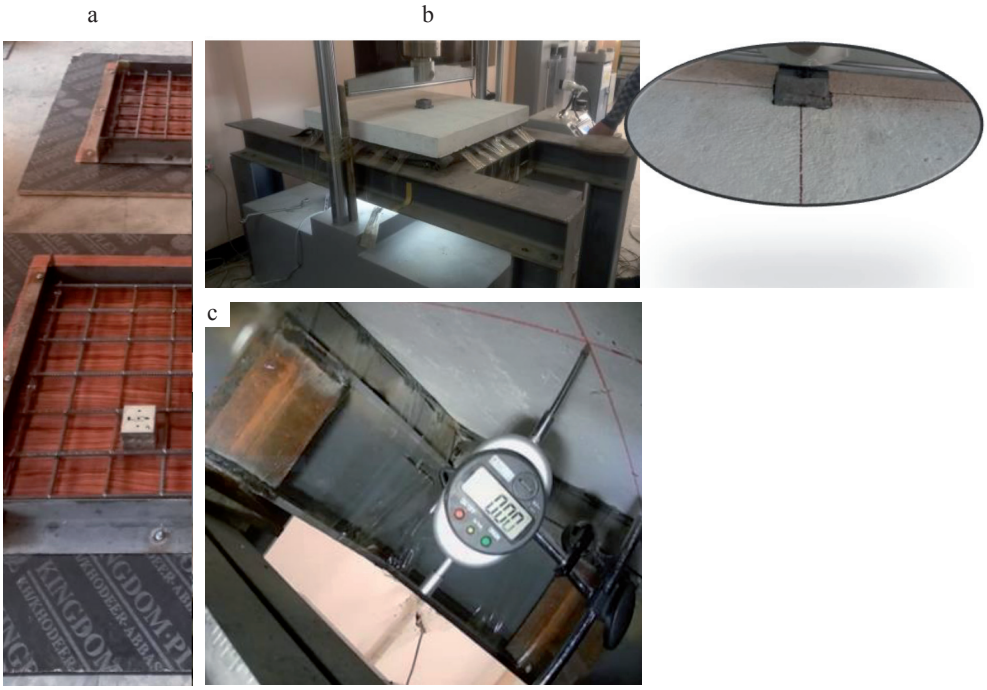

FIGURE 3. Slab testing: a – molds of slab; b – test device and loading plate; c – dial gages
Source: own work.

Results and discussion

Ultimate load and first crack load

The ultimate load capacity and first crack load values of slab samples are recorded in Table 3. It can be noted from the results that the addition of fibers led to an increase in the load capacity of about 52% for slabs without an opening

TABLE 3. Ultimate load and first crack load of slab specimens

Slab	First crack load [kN]	Ultimate load [kN]	Slab	First crack load [kN]	Ultimate load [kN]
S1-S	23.84	83.3	S1-O	20.63	81.2
S2-S	40.5	111.59	S2-O	35.95	107.47
S3-S	42.82	115.25	S3-O	38.48	108
S4-S	43.67	122.48	S4-O	40.7	109.4
S5-S	44.67	126.78	S5-O	41.9	115.92

and up to 42% for slabs with an opening. In slabs without openings, the increase in load capacity was more noticeable. For S2-S, S4-S, S2-O and S4-O slabs, the polypropylene fiber was constant at 0.15%, and the use of steel fiber with volume fractions of 0.75% and 1.5% enhances the ultimate load of the beam by approximately 33.96%, 52.19%, 32.35% and 42.75%, respectively. For S3-S, S5-S, S3-O and S5-O slabs, the polypropylene fiber was constant at 0.3%, and the steel fiber with volume fractions of 0.75% and 1.5% enhances the ultimate load of the beam by approximately 38.36%, 52.19%, 16.07% and 42.75%, respectively. Figure 5 clearly shows the influence of the hybrid fiber volume on the punching shear resistant of tested slabs. The ultimate loads of slabs with openings were decreased by 2.5–10.67% compared to similar slabs without openings.

The first crack load is significantly improved with fibers by 69–87%, for slabs without an opening and 74 to 103% for slabs with an opening. What is more, the presence of an opening decreases the first crack load between 6.2 and 13.46%, however, the influence of an opening was decreased as the hybrid fiber ratio increased. Figure 4 shows the ultimate load for different volume fraction of a hybrid fiber for the slab both with and without an opening.

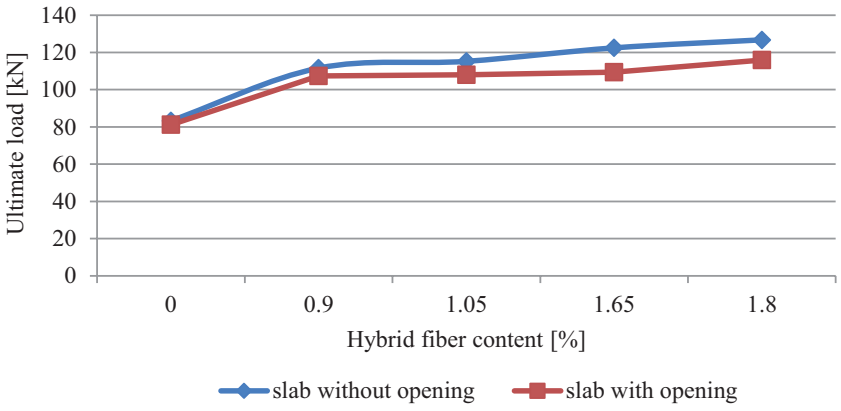

FIGURE 4. Ultimate load versus hybrid fiber content

Source: own work.

Zaezue, Sh. J., Hadi, W. K. (2023). Effect of hybrid steel-polypropylene fiber on punching shear behavior of flat slab with an opening. *Sci. Rev. Eng. Env. Sci.*, *32* (1), 3–17. DOI 10.22630/srees.4535

Load–deflection response

Figures 5–9 display the load–deflection curves for each two-way slab specimen. Typically, the elastic stage without cracks in the load–deflection curves begins with a linear behavior, followed by a nonlinear portion of the curve with an elastic cracking behavior. It is clear that the deflection obtained for specimens mixed with fibers is lower than for the control slab specimens (S1-S and S2-O), proving that the deflection was absorbed by the slab structure. Concrete mixtures using the hybrid fiber have better ductility and stiffness. The central deflections of slabs decreased slightly with increasing the volume fraction of hybrid fibers equivalent loads as demonstrated by Figures 10 and 11, from Figures 6–10 it can also be concluded that the slabs with openings develop higher deflections than the solid slabs.

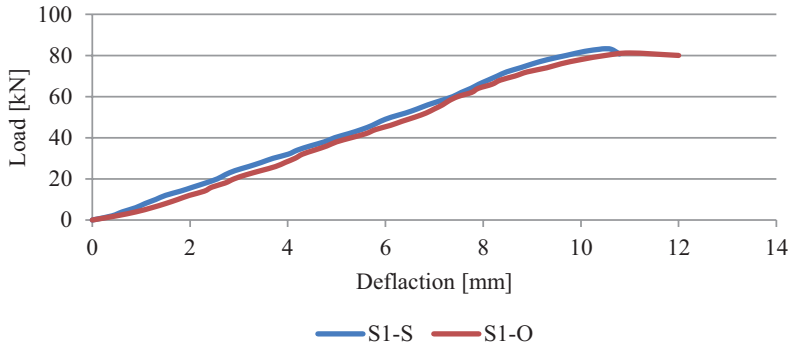

FIGURE 5. Load–deflection curves of control slab with and without opening
Source: own work.

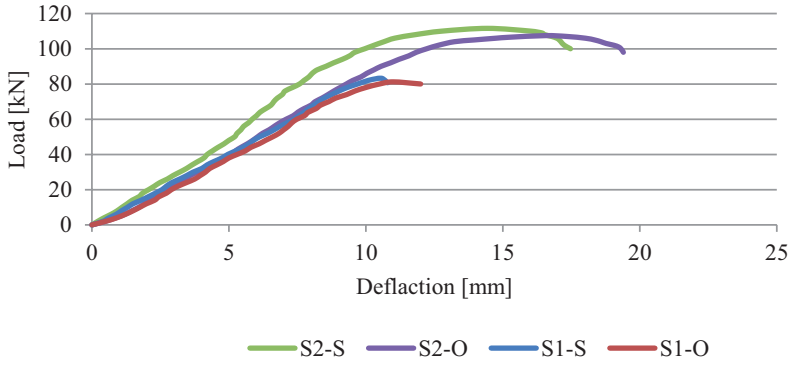

FIGURE 6. Load–deflection curves of slab with 0.9% of hybrid fibers
Source: own work.

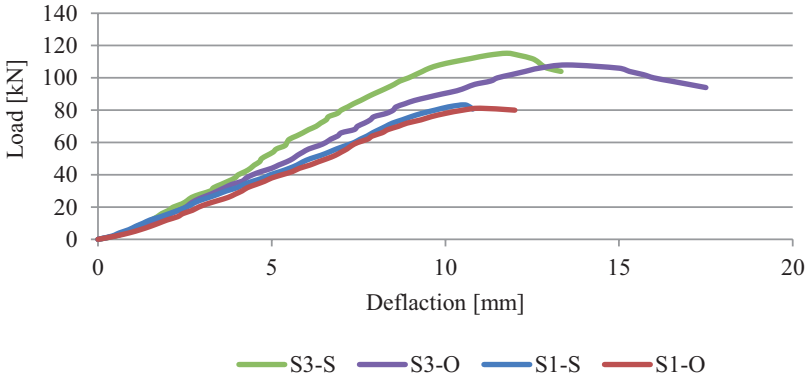

FIGURE 7. Load–deflection curves of slab with 1.05% of hybrid fibers
Source: own work.

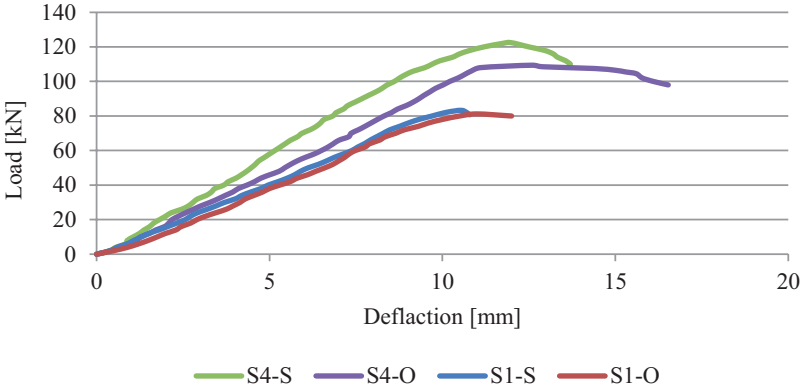

FIGURE 8. Load–deflection curves of slab with 1.65% of hybrid fibers
Source: own work.

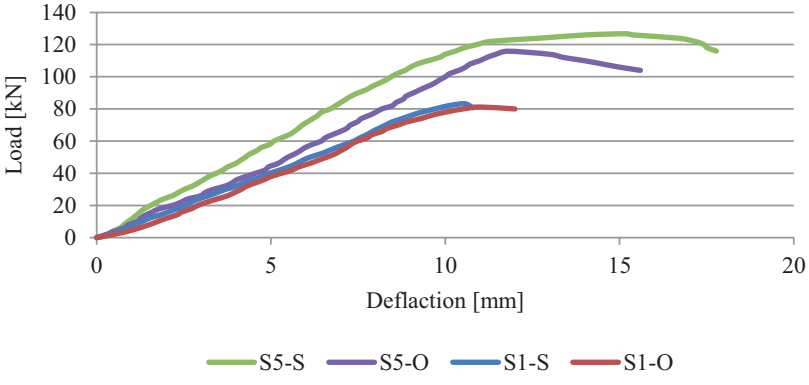

FIGURE 9. Load–deflection curves of slab with 1.8% of hybrid fibers
Source: own work.

Zaezue, Sh. J., Hadi, W. K. (2023). **Effect of hybrid steel-polypropylene fiber on punching** shear behavior of flat slab with an opening. *Sci. Rev. Eng. Env. Sci.*, *32* (1), 3–17. DOI 10.22630/srees.4535

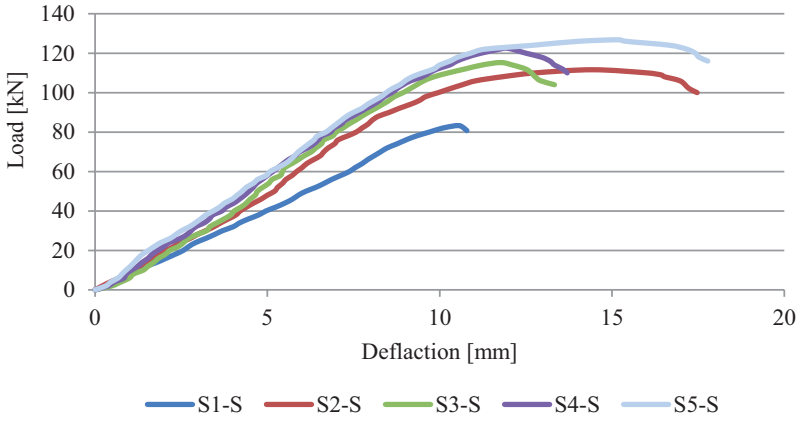

FIGURE 10. Load–deflection curves of solid slab with different ratio of hybrid fibers
Source: own work.

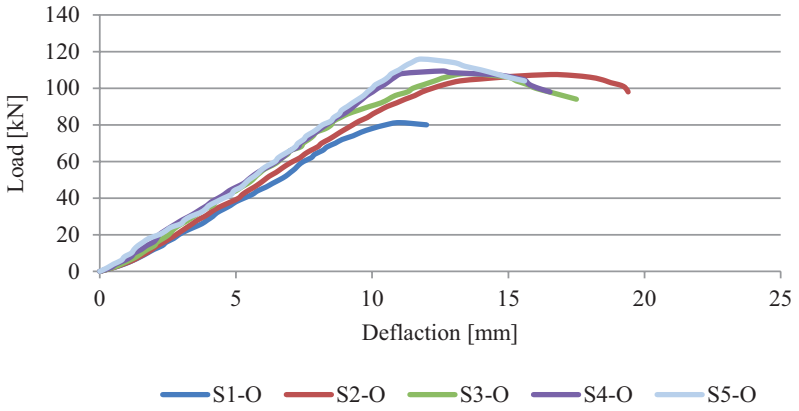

FIGURE 11. Load–deflection curves of slab with opening (different ratio of hybrid fibers)
Source: own work.

Modes of failure and crack patterns

Figure 12 shows all experimentally tested samples. In general, the slabs' tensile face is where the cracks first appeared, roughly under the laden area's boundaries, and then formed slowly across the whole slab. The cracks got steadily wider as the load got close to the slab's maximum shear strength. As the slabs began to fail, a loud noise was heard and the cut cone-shaped section of the slab was pushed under the load. This behavior was described by Kuang and Morley (1993).

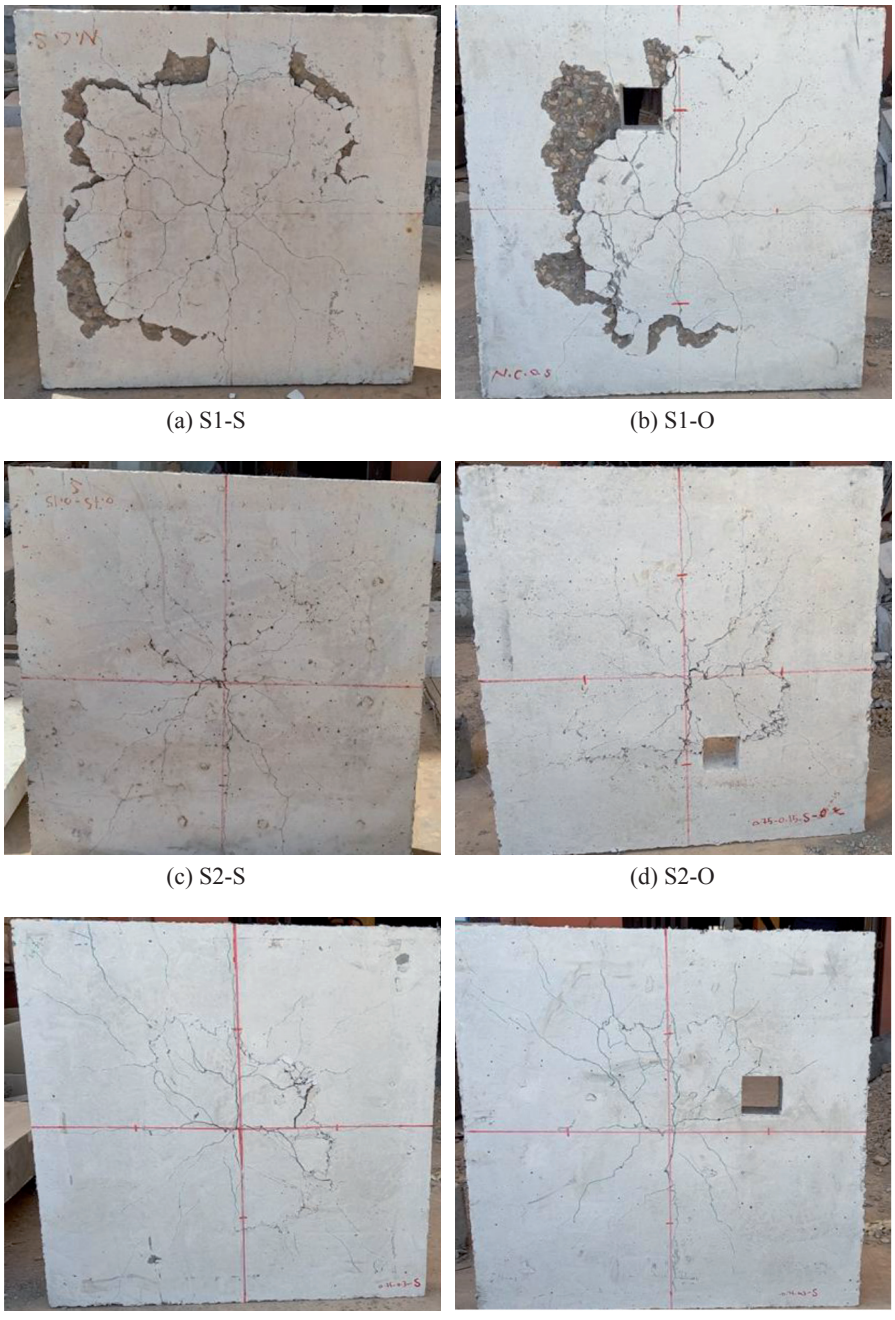

(a) S1-S (b) S1-O

(c) S2-S (d) S2-O

(e) S3-S (f) S3-O

FIGURE 12. Crack and failure pattern of tested slabs (a–f)
Source: own work.

Zaezue, Sh. J., Hadi, W. K. (2023). Effect of hybrid steel-polypropylene fiber on punching shear behavior of flat slab with an opening. *Sci. Rev. Eng. Env. Sci.*, *32* (1), 3–17. DOI 10.22630/srees.4535

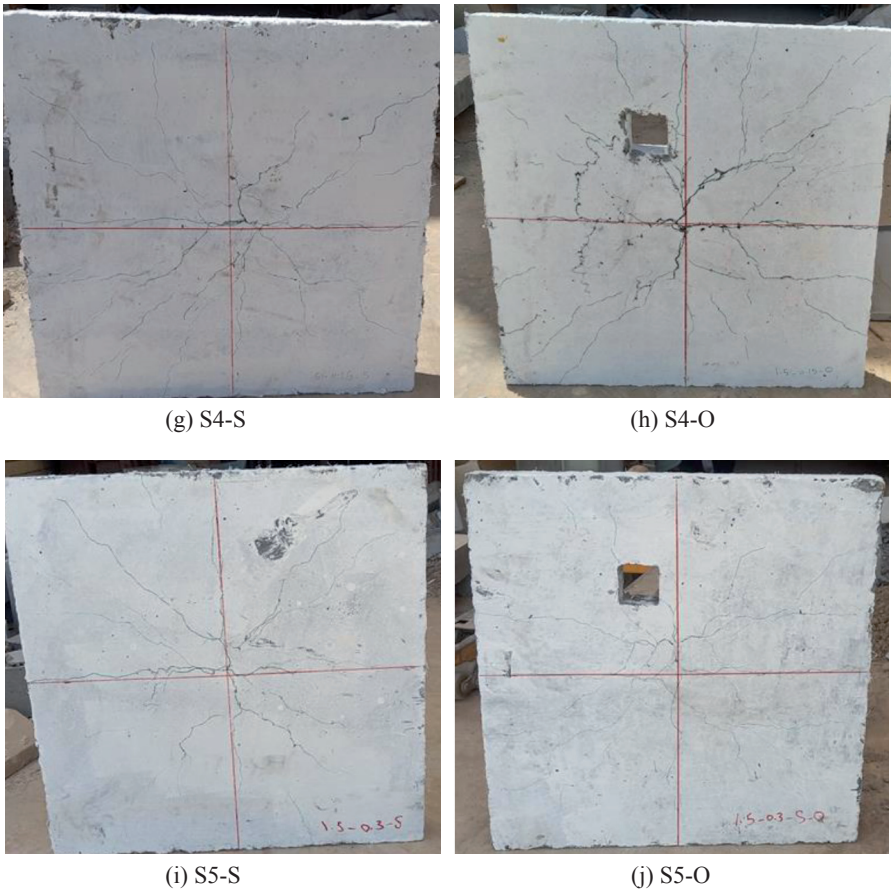

(g) S4-S (h) S4-O

(i) S5-S (j) S5-O

FIGURE 12 (cont.). Crack and failure pattern of tested slabs (g–j)

The control specimens without fibers failed in a more violent way and cracks spread widely. In other specimens with a hybrid fiber, there were more cracks in the slabs with greater fiber contents, and these were finer than the cracks in the slabs with minor values of volume fraction of steel fibers. Also, the cracks became closer to the punching zone by increasing fiber contents.

Conclusions

In general, the cracking and punching shear load increased together with the growth of the amount of hybrid fibers, just as the hybrid fiber ratio increased with the growth of the ultimate punching load. It was found that when add-

ing hybrid fibers to the solid slabs by ratios from 0 to 1.8%, the ultimate load increases from 33.96 to 52.19%, as compared with slabs without hybrid fibers. It was found that the hybrid fiber ratio in slabs with an opening is significant. The capacity of slabs was increased by about 32%, 33%, 34.73% and 42.75%, with the hybrid fiber ratio of 0.9, 1.05, 1.65 and 1.8, respectively, as compared with slabs without hybrid fibers.

In comparison to the similar solid test specimens, the presence of opening in slab specimens leads to a decrease in the ultimate load capacity. The ultimate load for slabs with an opening decreased by 13.46%, 11.23%, 10.13%, 6.8% and 6.2%, respectively.

References

American Concrete Institution [ACI] (2005). *Building code requirements for structural concrete and commentary* (ACI 318R-05). Farmington Hills: American Concrete Institution.

ASTM International [ASTM] (2013). *Standard specification for concrete aggregates* (ASTM C33/C33M-13). West Conshohocken, PA: ASTM International.

ASTM International [ASTM] (2015). *Standard specification for deformed and plain carbon-steel bars for concrete reinforcement* (ASTM A615/A615M-15a). West Conshohocken, PA: ASTM International.

ASTM International [ASTM] (2019). *Standard specification for chemical admixtures for concrete* (ASTM C494/C494M-19). West Conshohocken, PA: ASTM International.

ASTM International [ASTM] (2021). *Standard specification for portland cement* (ASTM C150/C150M-21). West Conshohocken, PA: ASTM International.

Afroughsabet, V. & Ozbakkaloglu, T. (2015). Mechanical and durability properties of high-strength concrete containing steel and polypropylene fibers. *Construction and Building Materials*, *94*, 73–82.

Alhozaimy, A., Soroushian, P. & Mirza, F. (1996). Mechanical properties of polypropylene fiber reinforced concrete and the effects of pozzolanic materials. *Cement and Concrete Composites*, *18* (2), 85–92.

Banthia, N. & Gupta, R. (2006). Influence of polypropylene fiber geometry on plastic shrinkage cracking in concrete. *Cement and Concrete Research*, *36* (7), 1263–1267.

Banthia, N., Majdzadeh, F., Wu, J. & Bindiganavile, V. (2014). Fiber synergy in Hybrid Fiber Reinforced Concrete (HyFRC) in flexure and direct shear. *Cement and Concrete Composites*, *48*, 91–97.

Barrera, A., Bonet, J., Romero, M. L. & Miguel, P. (2011). Experimental tests of slender reinforced concrete columns under combined axial load and lateral force. *Engineering Structures*, *33* (12), 3676–3689.

Brandt, A. M. (2008). Fibre reinforced cement-based (FRC) composites after over 40 years of development in building and civil engineering. *Composite Structures*, *86* (1–3), 3–9.

British Standards Institution [BSI] (1991). *Testing concrete. Part 116: method for determination of compressive strength of concrete cubes* (BS 1881-116). London: British Standards Institution.

Chi, Y., Xu, L., Mei, G., Hu, N., & Su, J. (2014). A unified failure envelope for hybrid fibre reinforced concrete subjected to true triaxial compression. *Composite Structures*, *109*, 31–40.

Chi, Y., Xu, L. & Yu, H. S. (2014). Constitutive modeling of steel-polypropylene hybrid fiber reinforced concrete using a non-associated plasticity and its numerical implementation. *Composite Structures*, *111*, 497–509.

Di Prisco, M. & Felicetti, R. (1997). Some results on punching shear in plain and fibre-reinforced micro-concrete slabs. *Magazine of Concrete Research*, *49* (180), 201–219.

Dry, C. (1994). Matrix cracking repair and filling using active and passive modes for smart timed release of chemicals from fibers into cement matrices. *Smart Materials and Structures*, *3* (2), 118.

Gu, D. S., Wu, Y. F., Wu, G. & Wu, Z. S. (2012). Plastic hinge analysis of FRP confined circular concrete columns. *Construction and Building Materials*, *27* (1), 223–233.

Issa, M. S., Metwally, I. M. & Elzeiny, S. M. (2011). Influence of fibers on flexural behavior and ductility of concrete beams reinforced with GFRP rebars. *Engineering Structures*, *33* (5), 1754–1763.

Kuang, J. S. & Morley, C. T. (1993). Punching shear behavior of restrained reinforced concrete slabs. *Structural Journal*, *89* (1), 13–19.

Labib, W. A. (2020). Evaluation of hybrid fibre-reinforced concrete slabs in terms of punching shear. *Construction and Building Materials*, *260*, 119763.

Mansour, F. R., Bakar, S. A., Ibrahim, I. S., Marsono, A. K., & Marabi, B. (2015). Flexural performance of a precast concrete slab with steel fiber concrete topping. *Construction and Building Materials*, *75*, 112–120.

Paulay, T. & Priestley, M. J. N. (1993). *Seismic design of reinforced concrete and masonry buildings*. Hoboken: John Wiley & Sons.

Qian, C. & Stroeven, P. (2000). Development of hybrid polypropylene-steel fibre-reinforced concrete. *Cement and concrete Research*, *30* (1), 63–69.

Sivakumar, A. (2011). Influence of hybrid fibres on the post crack performance of high strength concrete. Part I: experimental investigations. *Journal of Civil Engineering and Construction Technology*, *2* (7), 147–159.

Xu, L., Xu, H., Chi, Y. & Zhang, Y. (2011). Experimental study on tensile strength of steel-polypropylene hybrid fiber reinforced concrete. *Advanced Science Letters*, *4* (3), 911–916.

Yao, W., Li, J. & Wu, K. (2003). Mechanical properties of hybrid fiber-reinforced concrete at low fiber volume fraction. *Cement and Concrete Research*, *33* (1), 27–30.

Summary

Effect of hybrid steel-polypropylene fiber on punching shear behavior of flat slab with an opening. This research aimed to gain a better understanding of how the addition of fiber influences the punching shear capacity of two-way slabs by conducting an experi-

ment into the structural behavior of flat slabs with and without a square opening using different volume fractions of hybrid steel-polypropylene fiber (0%, 0.9%, 1.05% and 1.8%). Ten 700 × 700 × 70 mm slabs were divided into five pairs, with two samples used as control samples (with and without openings), and eight other samples with different volume fraction of fibers. Results showed that an increase in fiber content enhanced the shear strength of the slabs. For example, as the volume fraction of hybrid fiber increased from 0.0 to 1.8%, the ultimate load increased by 52% for slabs without an opening and up to 42% for slabs with an opening.

Scientific Review Engineering and Environmental Sciences (2023), 32 (1), 18–33

Sci. Rev. Eng. Env. Sci. (2023), 32 (1) https://srees.sggw.edu.pl

ISSN 1732-9353 (suspended) eISSN 2543-7496 DOI 10.22630/srees.4479

Received: 02.10.2022
Accepted: 10.12.2022

Socrates Pedro MUÑOZ PÉREZ[1]✉ https://orcid.org/0000-0003-3182-8735

Jorge Junior ATOCHE ZAMORA[2] https://orcid.org/0000-0002-3241-9856

[1]Cesar Vallejo University, Faculty of Engineering and Architecture, Peru
[2]Lord of Sipan University, Faculty of Engineering, Architecture and Urban Planning, Peru

Effects of incorporating granite powder in the mechanical properties of concrete

Keywords: concrete, granite powder, compressive strength, flexural strength, workability

Introduction

The use of recycled materials in the production of concrete is an issue that has generated interest among many researchers for the purpose of improving the environment (Najaf & Abbasi, 2022a).

The subject under study has been of interest to other authors, and engineering studies have been carried out internationally in Pakistan, the researchers focused on the problem of granite powder (GP) produced in the granite processing industry, which is fatal to humans and not disposable due to limited disposal sites (Zhang, Ji, He & He, 2019). Researchers propose that GP could be valuably incorporated as a partial replacement for sand in concrete so as not to harm the environment, health, and thus avoid shortages to meet the sand demand (Zafar, Javed, Khushnood, Nawaz & Zafar, 2020; Ghouchani, Abbasi & Najaf, 2022). Adding Iran to this, (Amani, Babazadeh, Sabohanian & Khalilianpoor, 2019), incorporating the GP at 10% as a partial replacement for sand increases its compressive strength by

✉mperezsp@ucvvirtual.edu.pe

up to 11% compared to its standard design of 210 kg·cm^{-2} (Prokopski, Marchuk & Huts, 2020). Similarly, in another study, GP was incorporated at 28.4% and 45% as a partial replacement for the sand for a design of 210 kg·cm^{-2} where the resistance was increased by 19% and 25% compared to the standard design, demonstrating an effect positive in both early strength and quality of concrete, as well as strength after 90 and 180 days of hardening (Ghorbani et al., 2019; Najaf & Abbasi, 2022b). Respect for the environment and the profitability of residual GP make it an acceptable and sustainable alternative construction material, indicating an enormous potential for GP as a replacement for natural fine aggregate (Singh, Khan, Khandelwal, Chugh & Nagar, 2016; Najaf & Abbasi, 2022a).

In Brazil, the GP produces a great environmental impact, due to the high demand for extraction of ornamental rocks, especially granite; the production of ornamental stones is at a very high level, reaching 9.3 M t in 2013; of this total, 4.6 M t are only granite; the final disposal of this waste has caused serious environmental problems; for this reason, the researchers are looking for ways to put this waste to use (Almeida, Soares & Matos, 2020). They carried out temperature tests incorporating the GP at 17% in a design of 210 kg·cm^{-2}, consequently, the fresh concrete is not affected by the incorporation of the GP, keeping it in the ambient temperature range. They also carried out high temperature tests illustrating a behavior of a higher the temperature and the faster the cooling process, resisting up to 600°C without affecting the concrete (dos Santos & Rodrigues, 2016). The workability was also analyzed with 30% and 50% GP in a 210 kg·cm^{-2} concrete, evidencing a reduction in water absorption; consequently, its workability was affected to the highest percentage, showing a dry consistency and a slump of 1″ at 50% GP (Cordeiro, de Alvarenga & Rocha, 2016).

In India the GP is proposed as a good alternative to using natural sand in the preparation of concrete, obtaining up to a 10% increase in flexural strength for 210 kg·cm^{-2} concrete containing 50% GP (Singh, Nagar & Agrawal, 2016). Researchers recommend that concrete incorporated with the GP by natural fine aggregate up to 30% for use in all structural applications, added GP at 10%, 20%, 30%, 40% and 50% by weight of sand in the concrete 210 kg·cm^{-2}, obtaining an optimal result at 30% GP, because it improves the mechanical properties of the concrete by up to 20% in the compressive strength, and even the results obtained for the GP at 50% are also acceptable, but they observe a reduction in other properties, mainly in its resistance to bending and workability (Jain & Sancheti, 2022). In Thailand, researchers incorporated the GP at 20%, 30% and 50% as a partial replacement for sand for a 254 kg·cm^{-2} concrete, obtaining losses of 8%, 12% and 20%, respectively, in its flexural strength, evidencing that increasing the percent-

Muñoz Pérez, S. P., Atoche Zamora, J. Jr. (2023). Effects of incorporating granite powder in the mechanical properties of concrete. *Sci. Rev. Eng. Env. Sci*., *32* (1), 18–33. DOI 10.22630/srees.4479

age of GP decreases the resistance to bending (Tangaramvong, Nuaklong, Khine & Jongvivatsakul, 2021). In another study, the tests for the incorporation of granite powder at 4%, 10% and 15% GP also achieved this tendency to decrease its resistance by up to 8% with respect to its standard design of 210 kg·cm^{-2} (Shwetha, Kumar, Dalawai, Anadinni & Sowjanya, 2022). Regarding its workability, the GP was incorporated at 20% and 40% in a 210 kg·cm^{-2} concrete, the results of slump reduced from 3″ to 1″, therefore they indicate that the workability of the concrete was also proportionally affected when incorporating higher amount of the GP (Gupta & Vyas, 2018; Taji et al., 2019). Consequently, finding the percentage of optimal substitution of sand by the GP can open new paths in sustainable construction techniques and reduce the detrimental effect on the environment due to waste disposal (Özcan & Koç, 2018; Najaf, Orouji & Ghouchani, 2022).

This study aims to analyze the impact of the incorporation of the granite powder (GP) as a partial replacement of the sand in the concrete in the following percentages 10%, 15%, 20% and 30% to carry out a mixed design of 210 kg·cm^{-2} and density of 2.4 kg·m^{-3} since it is the design mostly used in conventional constructions, seeking to find an optimal proportion to increase its mechanical properties where the geotechnical characteristics of the aggregates were identified, beams and concrete specimens were elaborated; the results of bending and compression tests were compared at 7, 14 and 28 days of setting between the standard concrete and the concrete incorporated with GP. It is concluded that the optimal result was at 20% GP, where the compressive strength increases by 13%, while its flexural property and workability are in an optimal range according to the stipulated parameters, allowing an important use regarding this waste in the construction industry, thus contributing to recycling, environmental quality and the development of using new materials.

Material and methods

For this research, the study population covered the set of concrete design specimens according to the established construction standard f'_c = 210 kg·cm^{-2}. The sample consisted of 45 specimens and 45 concrete beams, with 9 samples per design. Standard concrete specimens and beams f'_c = 210 kg·cm^{-2}, concrete incorporated with GP at 10%, 15%, 20% and 30%. The fine GP was obtained from the granite cutting factories, Lima, the 1/2 stone and sand for the design of test tubes was obtained from the Cantera la Cría in Lambayeque (Peru) and the cement used in the present investigation is the cement portland type MS (Peru). Figure 1 shows the flowchart of processes carried out in research.

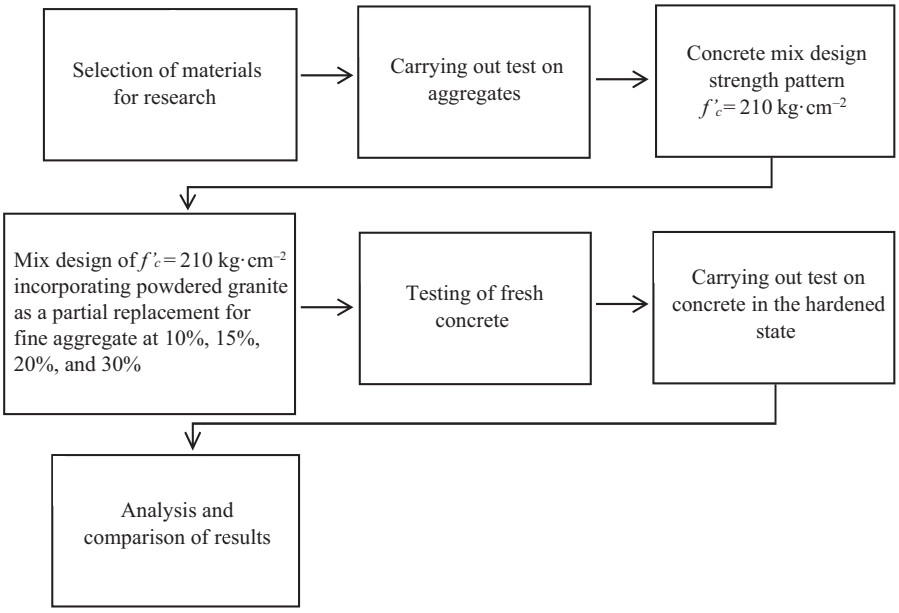

FIGURE 1. Process flow diagram
Source: own work.

Tests

Fine, coarse and GP aggregates geotechnical characteristics

To determine the geotechnical characteristics of the aggregates to be used in the mixed design (ASTM International [ASTM], 2015c), the following tests were carried out in the laboratory.

The fine aggregate is produced in a natural or artificial manner, it is the rocky material that passes through the standard 3/8-inch mesh and is retained in No 200; while the coarse aggregate is the rock material that does not pass through the No 4 mesh, this aggregate is produced by the natural or mechanical crushing of the stones; these have to comply with all the specifications mentioned in the current regulations (ASTM, 2015e). The aggregates for this study were obtained from natural quarries in Peru. Table 1 shows the results of the tests carried out to find the physical properties of the fine aggregates, coarse aggregates and GP.

Muñoz Pérez, S. P., Atoche Zamora, J. Jr. (2023). Effects of incorporating granite powder in the mechanical properties of concrete. *Sci. Rev. Eng. Env. Sci*., *32* (1), 18–33. DOI 10.22630/srees.4479

TABLE 1. Aggregate geotechnical characteristics

Parameter	Coarse aggregate	Fine aggregate	Granite powder
Nominal maximum size	1″	1/4″	1/4″
Fineness module	–	–	0.53
Moisture content	0.0087	0.039	0.0032
Dry loose unit weight [g·cm^{-3}]	1 419	–	–
Compacted unit weight [g·cm^{-3}]	1 504	–	–
Percent wear [%]	0.211	–	–
Salt content [%]	0.0004	–	–
Chloride content	0.000106	–	–
Sulfate content	0.000068	–	–
PE bulk (dry basis)	2 678	2 574	2 798
PE bulk (base saturated)	2 705	2 609	2 808
Pe apparent (dry basis)	2 752	2 667	2 828
Percentage of absorption [%]	0.0101	0.0135	0.0037
Sand equivalent	–	0.364	–
Salt content [%]	–	0.0007	–
Chloride content	–	0.000134	–
Sulfate content	–	0.000087	–
Fineness module	–	2.78	–

Source: own work.

The GP used in this study was obtained from the granite ornamental stone cutting factories, Figure 2 shows the GP with 0.53 fineness modulus used for the study before being incorporated into the mix.

FIGURE 2. Granite powder

Source: own work.

Specimens and beams preparation for a standard mix design

After the analysis of the aggregates, the mixture design was carried out for the resistance of 210 kg·cm^{-2} of the standard concrete, the data of which are shown in Table 2, which illustrates the content of materials to be used according to the weight proportion.

TABLE 2. Proportion in weight standard design

Resistance [kg·cm^{-2}]	Cement [bag]	Fine aggregate	Coarse aggregate	w/c
210	1	2.2	2.4	0.53

Source: own work.

Concrete mixture preparation with GP addition

Taking the standard design, 10%, 15%, 20% and 30% fine granitic aggregate is incorporated as a partial replacement for the sand in the concrete. Table 3 shows the mix designs in weight proportion incorporating the fine granite.

TABLE 3. Weight ratio of granite as a partial replacement for fine aggregate

Mix design	Resistance [kg·cm^{-2}]	Cement [bag]	Fine aggregate	Coarse aggregate	w/c	Aggregate granite
Design + 10% GP	210	1	1.98	2.4	0.53	0.22
Design + 15% GP	210	1	1.87	2.4	0.53	0.33
Design + 20% GP	210	1	1.76	2.4	0.53	0.44
Design + 30% GP	210	1	1.54	2.4	0.53	0.66

Source: own work.

Tests on fresh concrete

Abrams cone – slump test

The Abrams cone is an instrument that is applied to fresh concrete in order to obtain its fluidity or plasticity, the test consists of filling a cone-shaped metal mold with standardized dimensions, the process consists of forming three layers that will later be rammed with rods giving 25 blows, so that later the mold can be removed and the settlement of the fresh concrete can be measured (ASTM, 2015a).

Muñoz Pérez, S. P., Atoche Zamora, J. Jr. (2023). Effects of incorporating granite powder in the mechanical properties of concrete. *Sci. Rev. Eng. Env. Sci*., *32* (1), 18–33. DOI 10.22630/srees.4479

Temperature

It consists of determining the temperature in the fresh concrete, it is influenced by the mixing energy, the environment and the heat released due to the reaction of the cement. The temperature must be between 10° and 32°C, an increase in the temperature will make the mixture mature faster, so it is one of the most important parameters (ASTM, 2015f; ASTM 2015g).

Tests on concrete in hardened state

Compression strength test

It is carried out to verify if the prepared mixture meets the f'_c requirements for which it was designed, where a vertical force is applied until the concrete specimen fails. It is performed after 7, 14 and 28 days (ASTM, 2015b). For this study, the compression test was carried out on cylindrical concrete specimens, with standard measurements of 150 × 300 mm. Figure 3 shows the compressive strength test using the hydraulic press.

FIGURE 3. Compressive strength concrete test
Source: own work.

Flexural strength test

The test consists of testing concrete beams, but without reinforcement where a vertical load is applied in the center in order to find the rupture modulus of the concrete, this is determined according to the type of failure that originates in the

sample and generally ranges between 10% and 20% of the compressive strength (ASTM, 2016). For this study, concrete joists measuring 545 × 120 × 120 mm were made. Figure 4 shows the flexural strength test applied to the concrete joists.

FIGURE 4. Flexural strength concrete test
Source: own work.

Results and discussion

Comparison of the physical properties of standard concrete and concrete incorporating GP as a partial replacement for sand

The test results on the standard concrete of 210 kg·cm^{-2} and the designs incorporating the GP at 10%, 15%, 20% and 30% in its fresh and hardened state were compared.

In its fresh state, the slump test was carried out in order to analyze the workability of the concrete (ASTM, 2015f). Figure 5 shows the average results of each design, the settlement is reduced to a higher percentage of the GP making it less workable, up to 20% has the optimal workability necessary for molding and its use in various structures, while at 30% it has a very low workability and dry consistency. Table 4 shows the consistency classification according to its workability.

The results obtained are in line with Sharma, Kumar, Kumar, Thomas and Gupta (2017) who incorporated the GP at 20% and 40% for a design of 210 kg·cm^{-2}, their slump results reduced from 3″ to 1″, the decreasing trend in the slump was also noted by Cordeiro et al. (2016). The workability was analyzed with 30% and 50%

Muñoz Pérez, S. P., Atoche Zamora, J. Jr. (2023). Effects of incorporating granite powder in the mechanical properties of concrete. *Sci. Rev. Eng. Env. Sci.*, *32* (1), 18–33. DOI 10.22630/srees.4479

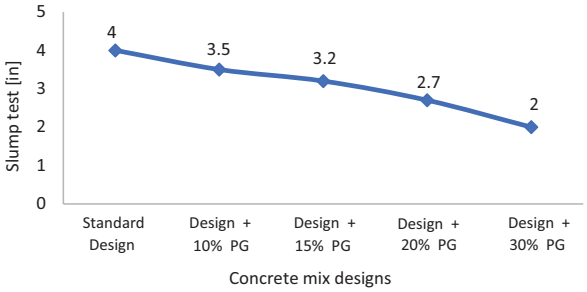

FIGURE 5. Slump test to determine workability
Source: own work.

TABLE 4. Consistency rating

Consistency	Slump	Workability
Dry	0″ to 2″	little workable
Plastic	3″ to 4″	workable
Fluid	> 5″	very workable

Source: ASTM (2015a).

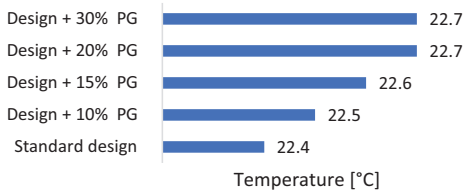

FIGURE 6. Temperature test
Source: own work.

GP in a 210 kg·cm^{-2} concrete, demonstrating a reduction in water absorption, getting a dry consistency and a slump of 1″ at 50% GP.

The temperature test was performed in its fresh state with a digital thermometer at the time of pouring the concrete (ASTM, 2015f). Figure 6 shows the temperature of different designs, demonstrating that there is no negative effect when incorporating granite powder.

The maximum temperature reached by this study was observed for the concrete incorporated with the GP and is linked to the time of pouring and ambient temperature, and according to the ACI it mentions that in order to make a mixture design we have to have an adequate temperature that is not too high, in which the temperature used did not reach 25°C, which is within an acceptable range (ASTM, 2015d). The same behavior is obtained by Calmeiro and Rodrigues (2016), who carried out temperature tests incorporating the GP at 17% in a design of 210 kg·cm^{-2}. As a consequence, fresh concrete is not affected by the incorporation of the GP, maintaining the ambient temperature range. What is more, they also carried out high temperature tests showing a behavior where the higher the temperature, the faster the cooling process, resisting up to 600°C without affecting the concrete.

In its hardened state, the compressive strength test was applied, where 9 concrete specimens were made for each design, where its average strength was determined in kg·cm^{-2} afer 7, 14 and 28 days from setting; all the designs with the GP obtained a higher resistance with respect to the standard concrete, reaching

275.4 kg·cm^{-2} after 28 days as the highest average compressive strength in the design incorporated with 30% GP as partial replacement of the sand, subsequent 20% GP with 268.6 kg·cm^{-2}, Figure 7 shows the means of compressive strength versus time, where it can be seen that the higher the percentage of granite, the higher the compressive strength.

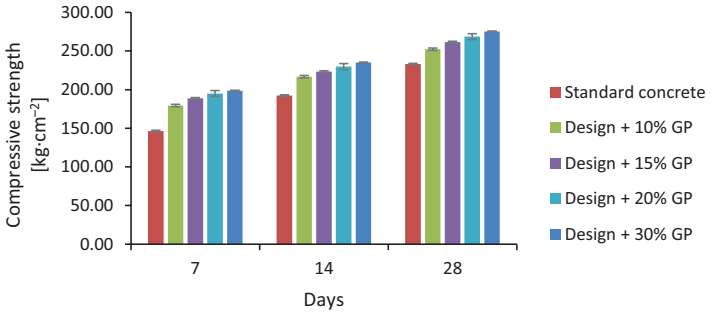

FIGURE 7. Variability of compressive strength at 28 days according to 7, 14, 28 days
Source: own work.

The results obtained are in line with Ghorbani et al. (2019) who achieved an improvement in their compressive strength by incorporating the GP at 10%, increasing up to 11% with respect to their standard design, as well as Prokopski et al. (2020) incorporated the GP at 28.4% and 45% as a partial replacement for sand for a 210 kg·cm^{-2} design, increasing resistance by 19% and 25% compared to the standard design; confirming the trend, Jain and Sancheti (2022), added the GP at 10%, 20%, 30%, 40% and 50% by weight of sand in the concrete 210 kg·cm^{-2}, obtaining an optimal result at 30% GP because it improves the mechanical properties of the concrete up to 20% of its resistance to compression and even the results obtained for the GP at 50% are acceptable, but a reduction in other properties can be observed, the results reaffirm an improvement directly proportional to a higher percentage of GP.

The flexural strength test was applied, where 9 concrete joists measuring 15 × 15 cm were made for each design, determining their rupture modulus in kg·cm^{-2} after 7, 14 and 28 days from setting, the results showed that a higher percentage of the GP incorporated in the design reduces the bending, complying with the parameters of minimum bending in the concrete up to the design of 20% GP, while the 30% design does not meet the parameters because the minimum rupture modulus must be between 10 and 15% of the compressive strength of the concrete (ASTM, 2016; National Ready Mixed Concrete Association [NRMCA], 2021).

Muñoz Pérez, S. P., Atoche Zamora, J. Jr. (2023). Effects of incorporating granite powder in the mechanical properties of concrete. *Sci. Rev. Eng. Env. Sci.*, *32* (1), 18–33. DOI 10.22630/srees.4479

Figure 8 shows the rupture modulus averages after 28 days of curing with respect to each design carried out, where a tendency to decrease with a higher percentage of the GP can be seen, with the lowest result being 26 kg·cm^{-2} belonging to the 30% GP design.

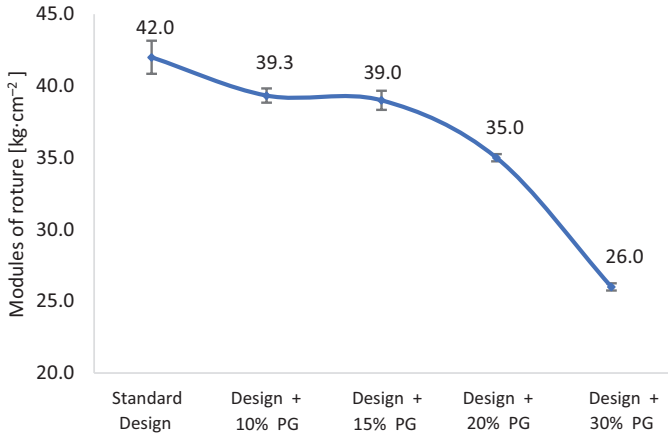

FIGURE 8. Flexural strength standard concrete vs concrete incorporated with GP after 28 days from setting

Source: own work.

The trend is also manifested in the results of Tangaramvong et al. (2021) who incorporated 20%, 30% and 50% of the GP as a partial replacement of the sand for a 254 kg·cm^{-2} concrete, obtaining losses of 8%, 12% and 20%, respectively, in its resistance to bending, thus evidencing that increasing the percentage of the GP decreases the resistance to bending. Shwetha et al. (2022) carried out tests of GP incorporation at 4%, 10% and 15% GP in a 210 kg·cm^{-2} concrete and also achieved this tendency of decreasing its resistance by up to 8% with respect to its standard design. All results contradict the reports made by Singh et al. (2016), who demonstrated a 10% increase in flexural strength for 210 kg·cm^{-2} concrete containing 50% GP.

Optimal dosage for the incorporation of GP as a partial replacement for sand

After evaluating the properties of the concrete of the different designs made, the proposed tests and results were obtained using standards such as ACI and ASTM. Concrete incorporating fine granite powder at 20% as a partial replacement for

sand in concrete has been proposed as the optimal design, due to its results being within the ranges established by different regulations, the proportions of the materials are shown in Table 5. After 28 days, the 20% GP design obtained a compressive strength of 268.6 kg·cm^{-2} growing by 13% with respect to the standard concrete, a 3″ slump entering the workable mix range with a plastic consistency and a flexural strength within the ranges recommended by the ASTM C293 standard (ASTM, 2016), the modulus of rupture being 13.04% of its compressive strength.

TABLE 5. Design optimal 20% GP

Mix design	Resistance [kg·cm^{-2}]	Cement content	Fine aggregate content	Coarse aggregate content	Aggregate granite content	Water content
Design + 20% GP	210	1	1.76	2.4	0.44	19.9

Source: own work.

However, the 30% GP design obtained a higher compressive strength, reaching 275.4 kg·cm^{-2} after 28 days from setting, increasing the compressive strength by 18.2% with respect to the standard concrete, but this result is overshadowed by its other properties, such as the 2″ slump, which is not very practical, having a dry consistency, and a modulus of rupture of 26 kg·cm^{-2}, being a result smaller than the minimum recommended flexural strength, by the ASTM C293 standard, which recommends that it should be between 10% and 15% of the compressive strength (ASTM, 2016; Sharma et al., 2017). For this reason, the 20% GP design has been proposed as the optimal dosage since it meets all the parameters stipulated in this study.

Conclusions

When evaluating the properties of the 210 kg·cm^{-2} standard concrete and the designs incorporating GP as a partial replacement of the sand in the following percentages: 10%, 15%, 20% and 30% in its fresh state, a reduction in slump with a greater amount of GP was indicated, resulting in slumps of 3.5″ to 2″ compared to the 4″ obtained with the standard concrete; the temperature has not been affected since it was maintained according to the time of pouring, reaching a maximum temperature of 24°C.

The tests carried out in its hardened state show an increase in the compressive strength with a higher percentage of GP, where an increase of up to 17% was

obtained in the 30% GP design with an average strength of 272.5 kg·cm^{-2} and an average of 262.33 kg·cm^{-2} at 20% compared to the 233 kg·cm^{-2} standard concrete increasing up to 13%; in its flexural strength the standard concrete obtained an average rupture modulus of 40 kg·cm^{-2},while the concrete with granite powder up to the 20% GP design complies with the recommended ranges of flexural strength of 35 kg·cm^{-2}, illustrating that the higher the percentage of granite powder, the lower the flexural strength.

It is proposed as a 20% optimal GP design with a water-cement ratio of 0.53, since it managed to improve the compressive strength up to 13%, with respect to the flexural strength an average rupture modulus of rupture of 35 kg·cm^{-2} was evidenced complying with the parameters of the minimum flexural strength in structures where it is recommended that the bending should be between 10–15% of the compressive strength. What is more, good results in its workability were indicated, and according to its temperature characteristics, this design can be applied in the development of structural elements without having an adverse effect on them.

References

Almeida, K. S. D., Soares, R. A. L. & Matos, J. M. E. D. (2020). Efeito de resíduos de gesso e de granito em produtos da indústria de cerâmica vermelha: revisão bibliográfica [Effect of gypsum and granite residues on products from the red ceramic industry: literature review]. *Matéria (Rio de Janeiro)*, *25* (1), e-12568. https://doi.org/10.1590/s1517-707620200001.0893

Amani, A., Babazadeh, A., Sabohanian, A. & Khalilianpoor, A. (2019). Mechanical properties of concrete pavements containing combinations of waste marble and granite powders. *International Journal of Pavement Engineering*, *22* (12), 1531–1540. https://doi.org/10.1080/10298436.2019.1702662

ASTM International [ASTM] (2015a). *Slump of portland cement concrete* (ASTM C143). West Conshohocken: ASTM International.

ASTM International [ASTM] (2015b). *Standard test method for compressive strength of cylindrical concrete specimens* (ASTM C39/C39M). West Conshohocken: ASTM International.

ASTM International [ASTM] (2015c). *Standard test method for particle-size analysis of soils* (ASTM D422). West Conshohocken: ASTM International.

ASTM International [ASTM] (2015d). *Standard test method for relative density (specific gravity) and absorption of coarse aggregate* (ASTM C127-15). West Conshohocken: ASTM International.

ASTM International [ASTM] (2015e). *Standard test method for sieve analysis of fine and coarse aggregates* (ASTM C136). West Conshohocken: ASTM International.

ASTM International [ASTM] (2015f). *Standard test method for temperature of freshly mixed hydraulic cement concrete* (ASTM C1064). West Conshohocken: ASTM International.

ASTM International [ASTM] (2015g). *Standard test method for temperature of freshly mixed hydraulic cement concrete* (ASTM C1064/C1064M-08). West Conshohocken: ASTM International.

ASTM International [ASTM] (2016). *Standard test method for flexural strength of concrete (using simple beam with center-point loading)* (ASTM C293). West Conshohocken: ASTM International.

Cordeiro, G. C., Alvarenga, L. M. S. C. de & Rocha, C. A. A. (2016). Rheological and mechanical properties of concrete containing crushed granite fine aggregate. *Construction and Building Materials*, *111*, 766–773. https://doi.org/https://doi.org/10.1016/j.conbuildmat.2016.02.178

Ghorbani, S., Taji, I., Brito, J. de, Negahban, M., Sahar, G., Tavakkolizadeh, M. & Davoodi, A. (2019). Mechanical and durability behaviour of concrete with granite waste dust as partial cement replacement under adverse exposure conditions. *Construction and Building Materials*, *194*, 143–152. https://doi.org/10.1016/j.conbuildmat.2018.11.023

Ghouchani, K., Abbasi, H. & Najaf, E. (2022). Some mechanical properties and microstructure of cementitious nanocomposites containing nano-SiO_2 and graphene oxide nanosheets. *Case Studies in Construction Materials*, *17*, e01482. https://doi.org/10.1016/j.cscm.2022.e01482

Gupta, L. K. & Vyas, A. K. (2018). Impact on mechanical properties of cement sand mortar containing waste granite powder. *Construction and Building Materials*, *191*, 155–164. https://doi.org/10.1016/j.conbuildmat.2018.09.203

Jain, K. L. & Sancheti, G. (2022). Effect of granite fines on mechanical and microstructure properties of concrete. *Advances in Concrete Construction*, *13* (6), 461–470. https://doi.org/10.12989/acc.2022.13.6.461

Najaf, E. & Abbasi, H. (2022a). Impact resistance and mechanical properties of fiber-reinforced concrete using string and fibrillated polypropylene fibers in a hybrid form. *Structural Concrete Journal of the fib*, *2022*, 1–14. https://doi.org/10.1002/suco.202200019

Najaf, E. & Abbasi, H. (2022b). Using recycled concrete powder, waste glass powder, and plastic powder to improve the mechanical properties of compacted concrete: cement elimination approach. *Advances in Civil Engineering*, *2022*, 9481466. https://doi.org/10.1155/2022/9481466

Najaf, E., Orouji, M. & Ghouchani, K. (2022). Finite element analysis of the effect of type, number, and installation angle of FRP sheets on improving the flexural strength of concrete beams. *Case Studies in Construction Materials*, *17*, e01670. https://doi.org/10.1016/j.cscm.2022.e01670

National Ready Mixed Concrete Association [NRMCA] (2021). *CIP 16 – Flexural strength of concrete. Alexandria, VA: National Ready Mixed Concrete Association*. Retrieved from: https://eaglerockconcrete.com/wp-content/uploads/concrete-in-practice-16pr.pdf [accessed 30.09.2022].

Özcan, F. & Koç, M. E. (2018). Influence of ground pumice on compressive strength and air content of both non-air and air entrained concrete in fresh and hardened state. *Construction and Building Materials*, *187*, 382–393. https://doi.org/10.1016/j.conbuildmat.2018.07.183

Prokopski, G., Marchuk, V. & Huts, A. (2020). The effect of using granite dust as a component of concrete mixture. *Case Studies in Construction Materials*, *13*, e00349. https://doi.org/10.1016/j.cscm.2020.e00349

Santos, C. C. dos & Rodrigues, J. P. C. (2016). Calcareous and granite aggregate concretes after fire. *Journal of Building Engineering*, *8*, 231–242. https://doi.org/10.1016/j.jobe.2016.09.009

Sharma, N. K., Kumar, P., Kumar, S., Thomas, B. S. & Gupta, R. C. (2017). Properties of concrete containing polished granite waste as partial substitution of coarse aggregate. *Construction and Building Materials*, *151*, 158–163. https://doi.org/10.1016/j.conbuildmat.2017.06.081

Shwetha, K. G., Kumar, C. M., Dalawai, V. N., Anadinni, S. B. & Sowjanya, G. V. (2022). Comparative study on strengthening of concrete using granite waste. *Materials Today: Proceedings*, *62*, 5317–5322. https://doi.org/https://doi.org/10.1016/j.matpr.2022.03.389

Singh, S., Khan, S., Khandelwal, R., Chugh, A. & Nagar, R. (2016). Performance of sustainable concrete containing granite cutting waste. *Journal of Cleaner Production*, *119*, 86–98. https://doi.org/https://doi.org/10.1016/j.jclepro.2016.02.008

Singh, S., Nagar, R. & Agrawal, V. (2016). A review on Properties of Sustainable Concrete using granite dust as replacement for river sand. *Journal of Cleaner Production*, *126*, 74–87. https://doi.org/10.1016/j.jclepro.2016.03.114

Taji, I., Ghorbani, S., De Brito, J., Y. Tam, V. W., Sharifi, S., Davoodi, A., & Tavakkolizadeh, M. (2019). Application of statistical analysis to evaluate the corrosion resistance of steel rebars embedded in concrete with marble and granite waste dust. *Journal of Cleaner Production*, *210*, 837–846. https://doi.org/10.1016/j.jclepro.2018.11.091

Tangaramvong, S., Nuaklong, P., Khine, M. T. & Jongvivatsakul, P. (2021). The influences of granite industry waste on concrete properties with different strength grades. *Case Studies in Construction Materials*, *15*, e00669. https://doi.org/https://doi.org/10.1016/j.cscm.2021.e00669

Zafar, M. S., Javed, U., Khushnood, R. A., Nawaz, A. & Zafar, T. (2020). Sustainable incorporation of waste granite dust as partial replacement of sand in autoclave aerated concrete. *Construction and Building Materials*, *250*, 118878. https://doi.org/10.1016/j.conbuildmat.2020.118878

Zhang, H., Ji, T., He, B. & He, L. (2019). Performance of ultra-high performance concrete (UHPC) with cement partially replaced by ground granite powder (GGP) under different curing conditions. *Construction and Building Materials*, *213*, 469–482. https://doi.org/10.1016/j.conbuildmat.2019.04.058

Summary

Effects of incorporating granite powder in the mechanical properties of concrete. This study analyzes the effects of the incorporation of the granite powder (GP) as a partial replacement of the sand in the concrete in percentages of 10%, 15%, 20% and 30% to carry out a mix design of 210 $kg \cdot cm^{-2}$. Seeking to find an optimal proportion to increase its mechanical properties where the geotechnical characteristics of the aggregates were identified, workability, temperature, beams and concrete specimens were elaborated. The results of bending and compression tests were compared after 7, 14 and 28 days from

setting between the standard concrete and the concrete incorporated with the GP. It is concluded that the optimal result was at 20% GP with 268.6 $kg \cdot cm^{-2}$, where the compressive strength increases by 13%, while its flexural property rupture modulus of 35 $kg \cdot cm^{-2}$ and workability are in an optimal range according to the stipulated parameters, thus allowing an important application for this waste in the construction industry, therefore contributing to recycling, environmental quality and the development of the usage of new materials.

Scientific Review Engineering and Environmental Sciences (2023), 32 (1), 34–52

Sci. Rev. Eng. Env. Sci. (2023), 32 (1) https://srees.sggw.edu.pl

ISSN 1732-9353 (suspended) eISSN 2543-7496 DOI 10.22630/srees.4478

Received: 26.09.2022
Accepted: 01.12.2022

Rachid BAKHTI[1]✉

Baizid BENAHMED[2] https://orcid.org/0000-0003-4924-0059

Abdelghani LAIB[3]

[1, 3]University of Bouira, Faculty of Science and Applied Science, Algeria
[2]University of Djelfa, Development Laboratory in Mechanics and Materials, Algeria

Investigation for stress–strain curves of the plastic damage model for concrete

Keywords: plastic damage model, Barcelona model, concrete structures, nonlinear finite element method, stress–strain correlations

Introduction

Concrete is a material conventionally used for construction that is of major importance in the field of civil engineering. Mastering concrete structural design involves full control of the finite element analysis, which required using an appropriate numerical constitutive law to describe the real behavior of the concrete material. Several numerical constitutive laws were provided in the last few decades in order to describe the behavior of concrete. The linear and nonlinear elastic models are the simplest constitutive laws for describing the behavior of concrete. This category of models presumes a linear/nonlinear relationship between the stresses and the strains for the tension and the compression cases, the correlation between stresses and strains is governed by Hooke's law for the linear case, what is more, this category of models is characterized by elastically returning to the "unloaded" state after loading. This kind of model is quite accurate and sufficient to forecast

✉r.bakhti@univ-bouira.dz

the behavior of concrete for minor strain values, but it shows an important error margin when the strain values are significant. To overcome this issue a second category of models was developed using the plasticity theory in order to improve the accuracy of the outcomes for significant strain values. For the plasticity models, various constitutive laws were developed specifically for concrete, such as Ottosen (1977), and Menetrey and Willam (1995), where multiple modifications into the plasticity theory were provided in order to compute the strain and the stress. In addition, Han and Chen (1986), Dvorkin, Cuitiño and Gioia (1989) advised using the Drucker and Prager's yield function as a potential function to estimate the plastic strain, in the same manner, Vermeer and De Borst (1984) employed the constitutive equation of Mohr and Coulomb to provide a new potential function, in which substituting the internal friction angle with the dilatancy angle was suggested. The category of plasticity models can perfectly address small and large strains, but, unfortunately, this category of models cannot handle the concrete degradation which provides a large margin of error specifically after the peak point; furthermore, the concrete behavior is not the same for tension and compression cases. As recapitulation, the use of plasticity models to presume the behavior of concrete structures provides inaccurate outcomes, especially after the peak point. Several papers (Lubliner, Oliver, Oller & Oñate, 1989; Paliwal, Hammi, Moser & Horstemeyer, 2017; Poliotti & Bairán, 2019; Bhartiya, Sahoo & Verma, 2021; Xiao, Chen, Zhou, Leng & Xia, 2021; Liu, Zhang, Zhao, Wu & Guo, 2022; Lu, Meng, Zhou, Wang & Du, 2022) combine the damage of concrete with the plasticity theory to provide yet another category of models referred to as plastic damage models. One of the most innovative models in this category was developed by Lubliner et al. (1989) called the damage plastic model (DPM) also known as the Barcelona model. This model was upgraded by Lee and Fenves (1998) to address the cyclic loading. The recent form of this model was used by Javanmardi and Maheri (2019) to predict the crack propagation paths. Furthermore, Ahmed, Voyiadjis and Park (2020) suggested a new finite element implementation of this model through a novel stress decomposition. The new form of this model (Lee & Fenves, 1998) was implemented in the commercial finite element code ABAQUS under the name of concrete damaged plasticity model (CDPM). The CDPM has been widely used in various research papers, such as the work of Silva, Gamage and Fawzia (2019) where they used it to simulate the concrete damage. Likewise, Ren, Sneed, Yang and He (2015) used CDPM in the numerical simulation of prestressed precast concrete bridge deck panels. In addition, Othman and Marzouk (2018) used the CDPM to simulate ultra-high-performance fiber reinforced concrete material under impact loading rates at different damage stages. In the same manner, Meng,

Bakhti, R., Benahmed, B., Laib, A. (2023). Investigation for stress–strain curves of the plastic damage model for concrete. *Sci. Rev. Eng. Env. Sci.*, *32* (1), 34–52. DOI 10.22630/srees.4478

Yang and Yang (2022) used ABAQUS to evaluate the damage evolution of double--tube concrete column under axial force.

Various parameters are required to simulate the behavior of concrete using CDPM; the stress–inelastic strain diagram for compression and tension cases, the damage parameters evolution for compression and tension cases, the ratio of the second stress invariants on tensile and compressive meridians, the eccentricity, the ratio of biaxial compressive yield stress to uniaxial compressive yield stress, and the dilation angle. Minh, Khatir, Wahab and Cuong-Le (2021) suggested multiple enhancements of CDPM in order to eliminate several parameters where the softening phase in the compressive stress–strain curve has been modified and each of the tensile damage variables and the compressive damage variables was evaluated through an exponential function. To avoid those parameters, a local computer program was developed by the author called Concrete v. 2.0, where only the concrete strength is required for modeling concrete structures (Bakhti, Benahmed, Laib & Alfach, 2022).

This work examined the effect of the hardening function used in the finite element implementation of DPM on the final outcomes by comparing the generated stress–strain diagrams with the analytical solutions of Lubliner and also with other formulas suggested, respectively, by Desayi and Krishnan (1964) and Krätzig and Pölling (2004) for the compression case, and Thorenfeldt (1987) for the tension case. The outcomes of the Barcelona model presented in this paper are calculated by Concrete v. 2.0 using the methodology proposed in Bakhti et al. (2022), where the Lubliner's formulas (Lubliner et al., 1989) have been selected as a hardening function in the finite element implementation of DPM. For the compression case, this paper compared the stress–strain diagrams generated according to the Barcelona model with the stress–strain diagrams of Desayi and Krishnan (1964), Lubliner et al. (1989), and Krätzig and Pölling (2004). For the tension case, the stress–strain curves were compared with the stress–strain curves of Thorenfeldt et al. (1987) and Lubliner et al. (1989). This study helped select five values of concrete strengths, namely: 20 MPa, 25 MPa, 30 MPa, 35 MPa and 40 MPa.

Plastic damage model for concrete

The main concept of DPM is to substitute the hardening variable in the overall form of classical plasticity with the plastic damage variable. The value of the damage variable varies between zero and one, where the zero value represents the undamaged concrete and the value of one represents the totally damaged concrete with a full loss of cohesion. The fundamental equations of this model are as follows.

a) For the yield function

$$F = \frac{1}{1-\alpha}\left(3\alpha p + \sqrt{3}J + \beta\left\langle \sigma_{\max}\right\rangle - \gamma\left\langle -\sigma_{\max}\right\rangle\right) - c, \tag{1}$$

with α, β and γ are dimensionless parameters given by:

$$\alpha = \frac{\left(\frac{f_{b0}}{f_{c0}} - 1\right)}{\left(2\frac{f_{b0}}{f_{c0}} - 1\right)}, \tag{2}$$

$$\beta = R\left(1-\alpha\right) - \left(1+\alpha\right) \text{ with } R = \frac{f_{c0}}{f_{t0}}, \tag{3}$$

$$\gamma = 3(1 - r_{oct}^{\max}) / (2r_{oct}^{\max} - 1), \tag{4}$$

where: p – mean total stress, J – deviatoric stress, $\sigma_{\max}$ – maximum principal effective stress, c – cohesion, $\frac{f_{b0}}{f_{c0}}$ – ratio of biaxial and uniaxial compressive yield strengths. In SIMULIA (2010), the default value is 1.16, f_{t0} – initial uniaxial tensile yield stress, $r_{oct}^{\max}$ – constant takes a value of 0.65, according to Oller, Oñate, Oliver and Lubliner (1990), <*X*> – Macaulay's bracket and takes the form: $\left\langle \pm X\right\rangle = \frac{X \pm |X|}{2}$.

b) For the potential function

Lubliner et al. (1989) suggested a non-associated potential plastic flow. The potential function takes the same form as the classic Mohr–Coulomb constitutive equation with replacing the friction angle with the dilation angle. The potential function suggested by Lubliner et al. (1989) takes the following form:

$$G = p\,\sin\psi + J\left(\cos\theta - \frac{\sin\theta\sin\psi}{\sqrt{3}}\right), \tag{5}$$

where: p – mean total stress, ψ – dilation angle, J – deviatoric stress, θ – lode angle.

The second form of this model was developed by Lee and Fenves (1998) to address the dynamic loading where the following modifications were proposed, as follows.

Bakhti, R., Benahmed, B., Laib, A. (2023). Investigation for stress–strain curves of the plastic damage model for concrete. *Sci. Rev. Eng. Env. Sci.*, *32* (1), 34–52. DOI 10.22630/srees.4478

a) For the yield function substituting cohesion c by effective compressive cohesion stress $\overline{\sigma_c}$, or new formulas for β and γ parameters, given as:

$$\beta = \frac{\overline{\sigma_c}}{\sigma_t}(1-\alpha) - (1+\alpha), \tag{6}$$

$$\gamma = \frac{3(1-K_c)}{2K_c - 1}, \tag{7}$$

where: $\overline{\sigma_c}$ – effective compressive cohesion stress, $\overline{\sigma_t}$ – effective tensile cohesion stress, K_c – ratio of second stress invariants on tensile and compressive meridians.

As a result, the second form of the yield function suggested by Lee and Fenves (1998) is written as:

$$F = \frac{1}{1-\alpha}\left(3\alpha\, p + \sqrt{3}J + \beta\langle\sigma_{\max}\rangle - \gamma\langle-\sigma_{\max}\rangle\right) - \overline{\sigma_c}; \tag{8}$$

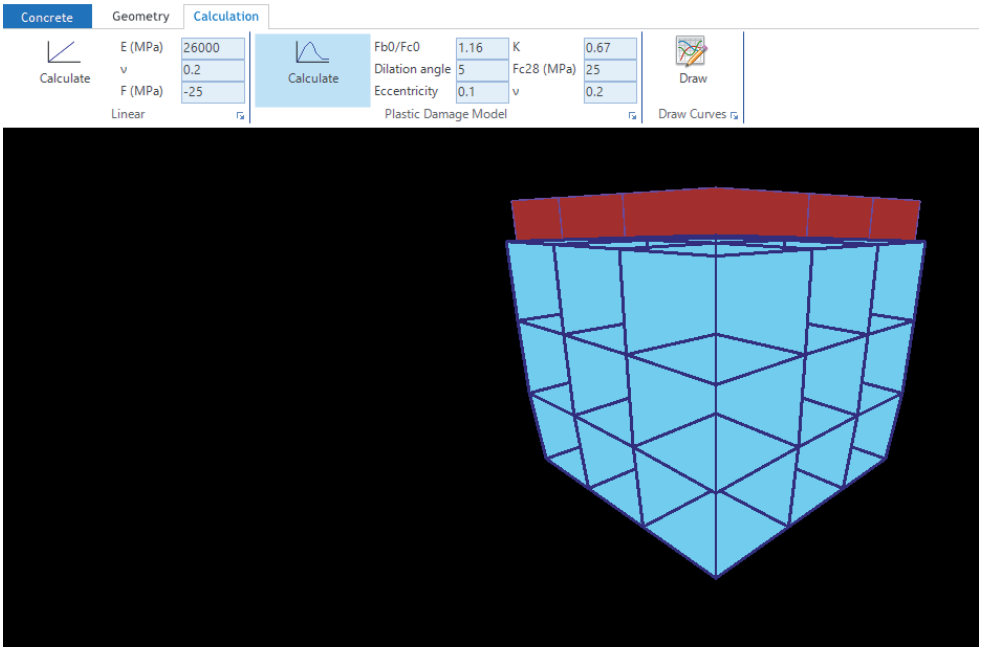

FIGURE 1. Modeling cubical concrete sample using Concrete v. 2.0 (dimensions: 300 × 300 × × 300 mm)

Source: own work.

b) For the potential function, suggested by Lee and Fenves (1998), takes the form:

$$G = \sqrt{(\varepsilon\sigma_{t_0}\tan\psi)^2+3J^2} + p\tan\psi, \tag{9}$$

where: ε – flow potential eccentricity – 0.1 in SIMULIA (2010), σ_{t0} – uniaxial tensile stress at failure.

Bakhti et al. (2022) developed a finite element program under the name Concrete v. 2.0 to model concrete behavior using DPM as a constitutive model and object-oriented programming paradigm (OOP) as a coding technique. All DPM curves presented in this paper were calculated by Concrete v. 2.0 for a cubical element with dimensions: 300 × 300 × 300 mm and by hiring the 8 nodes cubical element to generate 27 elements (Fig. 1).

Stress–strain correlations

Lubliner's stress–strain correlation

In 1989, Lubliner et al. (1989) suggested general correlations between the compressive and tensile stresses and the inelastic strain. Those correlations are used by Bakhti et al. (2022) as a hardening function in the finite implementation of DPM. According to the suggested correlations, the compressive and tensile stresses depend on the values of the coefficients a_c, a_t, b_c and b_t. The values of these coefficients were evaluated by Bakhti et al. (2022) according to the CEB-FIP Model Code recommendations (Comité euro-international du béton & Fédération internationale du béton [CEB-FIP], 2010) and presented in Tables 1 and 2. The stress–strain correlations suggested by Lubliner for tension and compression take the following forms:

$$\begin{cases} \sigma_c = f_{c0}\left[(1+a_c)e^{-b_c\varepsilon_c^{in}} - a_c e^{-2b_c\varepsilon_c^{in}}\right] \\ \sigma_t = f_{t0}\left[(1+a_t)e^{-b_t\varepsilon_t^{ck}} - a_t e^{-2b_t\varepsilon_t^{ck}}\right] \end{cases}. \tag{10}$$

For the stress–strain correlations, Bakhti et al. (2022) divided these curves into two parts for the compression and tension cases as shown in Figure 2. The first part represents the linear segment where the stress is evaluated according to Hooke's law. The second one represents the non-linear part where the stress is evaluated according to Lubliner's formulas.

Bakhti, R., Benahmed, B., Laib, A. (2023). Investigation for stress–strain curves of the plastic damage model for concrete. *Sci. Rev. Eng. Env. Sci.*, *32* (1), 34–52. DOI 10.22630/srees.4478

TABLE 1. Values of coefficients a_c, a_t, b_c and b_t for different concrete strength – Part 1

Coefficient	f_{ck} [MPa]						
	12	16	20	25	30	35	40
a_c	7.873	7.873	7.873	7.873	7.873	7.873	7.873
a_t	637.077	636.468	638.065	641.894	646.876	652.439	658.218
b_c	1.00	1.00	1.00	1.00	1.00	1.00	1.00
b_t	6 122.778	6 059.292	6 107.316	6 240.193	6 412.655	6 604.052	6 803.804

Source: own work.

TABLE 2. Values of coefficients a_c, a_t, b_c and b_t for different concrete strength – Part 2

Coefficient	f_{ck} [MPa]						
	45	50	55	60	70	80	90
a_c	7.873	7.873	7.873	7.873	7.873	7.873	7.873
a_t	663.972	669.533	674.783	679.639	687.945	698.146	794.836
b_c	1.00	1.00	1.00	1.00	1.00	1.00	1.00
b_t	7 005.913	7 206.661	7 403.612	7 595.106	7 957.263	8 334.567	9 769.134

Source: own work.

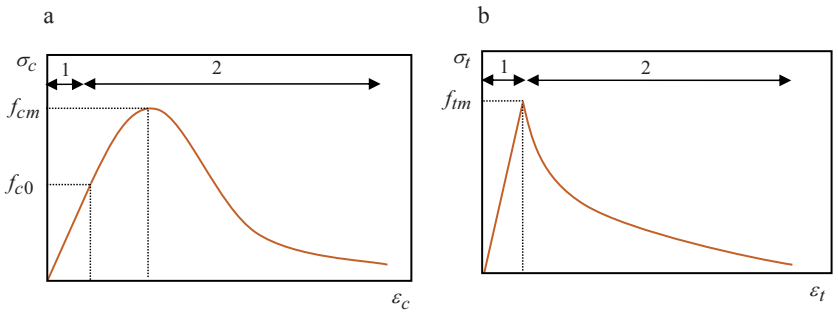

FIGURE 2. Decomposition of stress–strain curve in compression (a) and tension (b)
Source: own work.

Desayi and Krishnan's correlation

Using a series of experimental tests, several researches attempted to provide correlations between the stress and strain for both cases of compression and tension where the experimental outcomes are used to develop functions that can describe the material behavior. The simplest relationship was developed by Desayi and Krishnan (1964) that takes the following form:

$$\sigma = \frac{E\varepsilon}{1+(\frac{\varepsilon}{\varepsilon_p})^2}, \tag{11}$$

where: σ, ε – stress and strain tensors, E – Young's modulus, ε_p – strain at peak stress.

Krätzig and Pölling's correlation

This approach was adopted in the multiple research work to evaluate the compressive stress–strain diagrams. For instance, Alfarah, López-Almansa and Oller (2017) used the correlations of Krätzig and Pölling (2004) in their algorithm to auto-evaluate the stress–strain diagrams in ABAQUS. In this approach, the stress–strain curve is divided into three parts as shown in Figure 3, where the stress values are evaluated by:

– first part (linear till f_{c0}):

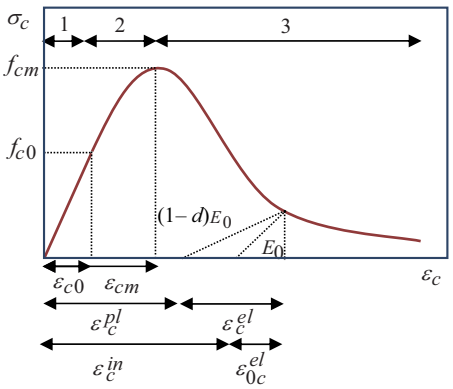

FIGURE 3. Krätzig's decomposition of the compressive stress–strain curve

Source: own work.

$$\sigma_{c(1)} = E_0 \varepsilon_c, \tag{12}$$

– second part (ascending between f_{c0} and f_{cm}):

$$\sigma_{c(2)} = \frac{E_{ci}\frac{\varepsilon_c}{f_{cm}} - \left(\frac{\varepsilon_c}{\varepsilon_{cm}}\right)^2}{1 + \left(E_{ci}\frac{\varepsilon_{cm}}{f_{cm}} - 2\right)\frac{\varepsilon_c}{\varepsilon_{cm}}} f_{cm}, \tag{13}$$

– third part (descending), given by:

$$\sigma_{c(3)} = \left(\frac{2+\gamma_c f_{cm}\varepsilon_{cm}}{2f_{cm}} - \gamma_c \varepsilon_c + \frac{\varepsilon_c^2 \gamma_c}{2\varepsilon_{cm}}\right)^{-1} \text{ with } \gamma_c = \frac{\pi^2 f_{cm}\varepsilon_{cm}}{2\left[\frac{G_{ch}}{L_{eq}} - 0.5 f_{cm}\left(\varepsilon_{cm}(1-b) + b\frac{f_{cm}}{E_0}\right)\right]^2}; \; b = \frac{\varepsilon_c^{pl}}{\varepsilon_c^{in}}, \tag{14}$$

where: f_{c0} – compressive stress that correspond to zero crushing, f_{cm} – peak compressive stress, ε_{cm} – strain at the peak compressive stress, E_0 – undamaged modulus of deformation, E_{ci} – initial tangent modulus of deformation of concrete, G_{ch} – crushing energy per unit area, L_{eq} – mesh size (characteristic length), ε_c^{pl} – compressive plastic strain, ε_c^{in} – compressive inelastic strain.

Bakhti, R., Benahmed, B., Laib, A. (2023). Investigation for stress–strain curves of the plastic damage model for concrete. *Sci. Rev. Eng. Env. Sci.*, *32* (1), 34–52. DOI 10.22630/srees.4478

Thorenfeldt's correlation

According to the Thorenfeldt's approach (Thorenfeldt, 1987), the tensile stress–strain curve can be divided into two parts. In the first part (till the peak point), the stress value is evaluated according to the Hooke's law. In the second part, the tensile stress is calculated in accordance with the following formula:

$$\sigma_t = f_{tm}\left(\frac{\varepsilon_{tm}}{\varepsilon_t}\right)^{\left(0.7+1{,}000\varepsilon_t\right)}, \tag{15}$$

where: f_{tm} – peak tensile stress, ε_{tm} – strain at the peak tensile stress.

Comparing the stress–strain curves of the barcelona model and several analytical correlations

Five values of concrete strengths are chosen to examine the outcomes of the Barcelona model compared to three stress–strain correlations for the compression case, namely: Desayi and Krishnan (1964), Lubliner et al. (1989), and Krätzig and Pölling (2004), and two stress–strain correlations for the tension case, that is: Thorenfeldt et al. (1987) and Lubliner et al. (1989). The selected values of concrete strengths are: 20 MPa, 25 MPa, 30 MPa, 35 MPa and 40 MPa. Each of Young's moduli and the strain value at peak stress that needed to calculate the stress value according to Desayi and Krishnan's correlation (Desayi & Krishnan, 1964) for each value of concrete strength are delivered in Table 3.

For Krätzig and Pölling's correlation (Krätzig & Pölling 2004), all curves are calculated the based on the mesh size of 300 mm. In addition, we used the model code recommendations (CEB-FIP, 2010) to calculate the following parameters:

– initial tangent modulus of deformation of concrete $E_{ci} = 10\,000\, f_{cm}^{1/3}$, (16)

– undamaged modulus of deformation $E_0 = E_{ci}\left(0.8 + 0.2\frac{f_{cm}}{88}\right)$, (17)

– compressive stress that corresponds to zero crushing $f_{c0} = 0.4\, f_{cm}$, (18)

– value of the strain at the peak stress $\varepsilon_{cm} = 0.5\, f_{cm}^{0.31} \le 2.8 \cdot 10^{-3}$, (19)

– crushing/fracture energy $G_{ch} = \left(\frac{f_{cm}}{f_{tm}}\right)^2 G_F$ [N·mm^{-1}], where $G_F = 0.073 f_{cm}^{0.18}$. (20)

Table 4 summarizes the values of the peak tensile stress and the strain at the peak tensile stress for each value of concrete strength that are required to evaluate the stress value according to Thorenfeldt's correlation. For Lubliner's correlations, we used the values of coefficients a_c, a_t, b_c and b_t that were calculated by Bakhti et al. (2022) and are presented in Tables 1 and 2. Moreover, according to this approach, the compressive and tensile stress–strain curves were divided into two parts. The first one represents the linear segment where the stress is evaluated according to Hooke's law. The second one represents the non-linear part where the stress is evaluated according to Lubliner's formulas.

For the compression case and according to Figures 4–8, the following observations can be outlined:

– The curves of the Barcelona model that were generated by Concrete v. 2.0 are completely in harmony with the stress–strain curve generated, according to the Lubliner's formula; this observation can be justified by the fact that the hardening function used in the implementation of DPM is identical to Lubliner's formulas.
– For the concrete strengths less than 25 MPa, the outcomes of the Barcelona model calculated using Concrete v. 2.0 are partly consistent with the stress–strain curve generated according to the Krätzig's formula. For values more than 25 MPa and using the Krätzig decomposition (Fig. 3), we observed that the curves of the Barcelona model diverge from the Krätzig's curve depending on the concrete strengths, especially in the third part.
– Using the Krätzig decomposition (Fig. 3), the outcomes of the Barcelona model are partly consistent with the stress–strain curve generated according to the Desayi's formula in the first and the second part (Fig. 3). As for the third part, the difference between both curves is significant.

TABLE 3. Input data of Desayi and Krishnan's curve

f_{cm} [MPa]	ε_p ($\times 10^{-3}$) [-]	E [MPa]
20	1.8	22 890
25	1.9	26 130
30	2	29 910
35	2.1	32 890
40	2.2	35 940

Source: own work.

TABLE 4. Input data of Thorenfeldt's curve

f_{cm} [MPa]	ε_{tm} ($\times 10^{-4}$) [-]	f_{tm} [MPa]
20	0.68	1.58
25	0.79	1.99
30	0.87	2.37
35	0.93	2.71
40	0.98	3.04

Source: own work.

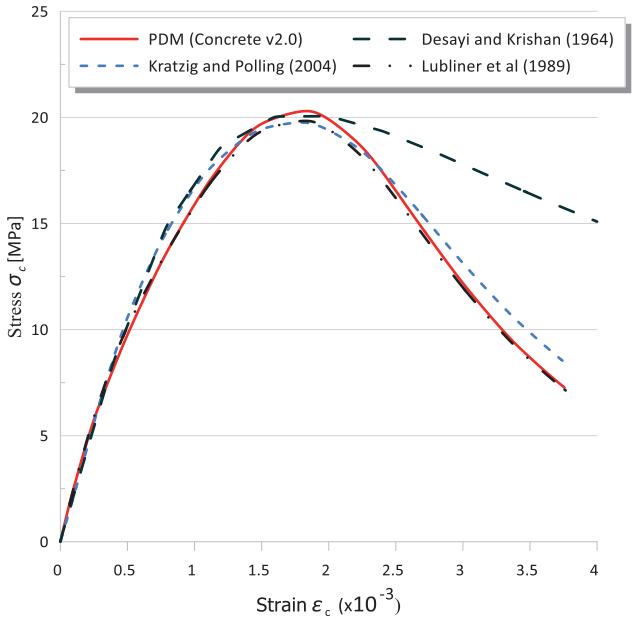

FIGURE 4. Compressive stress–strain curve for f_{cm} = 20 MPa

Source: own work.

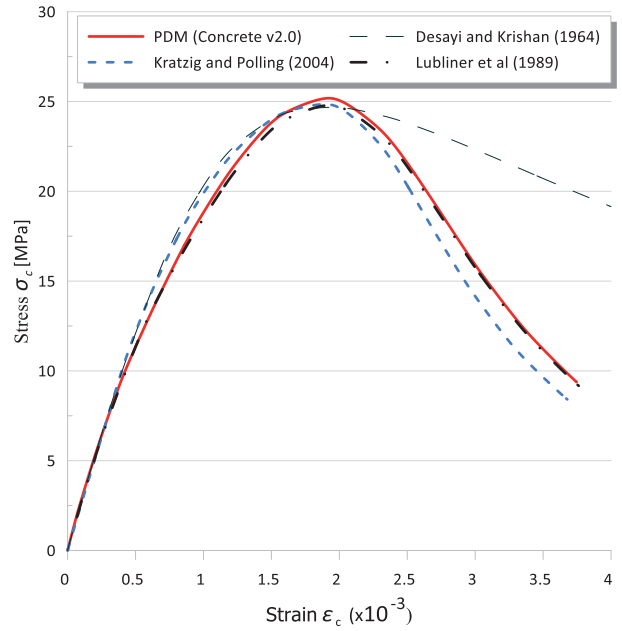

FIGURE 5. Compressive stress–strain curve for f_{cm} = 25 MPa

Source: own work.

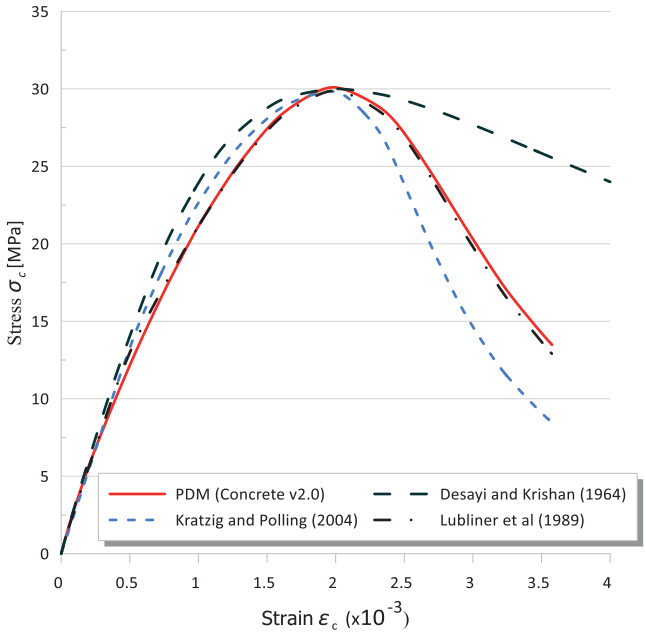

FIGURE 6. Compressive stress–strain curve for f_{cm} = 30 MPa
Source: own work.

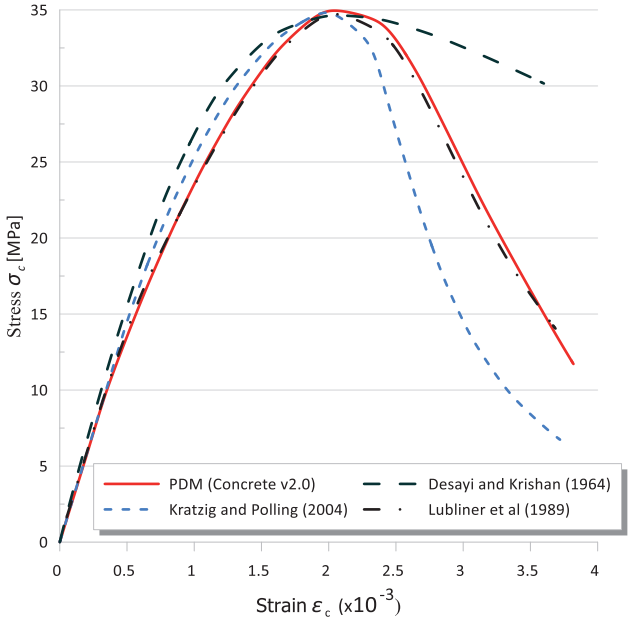

FIGURE 7. Compressive stress–strain curve for f_{cm} = 35 MPa
Source: own work.

Bakhti, R., Benahmed, B., Laib, A. (2023). Investigation for stress–strain curves of the plastic damage model for concrete. *Sci. Rev. Eng. Env. Sci.*, *32* (1), 34–52. DOI 10.22630/srees.4478

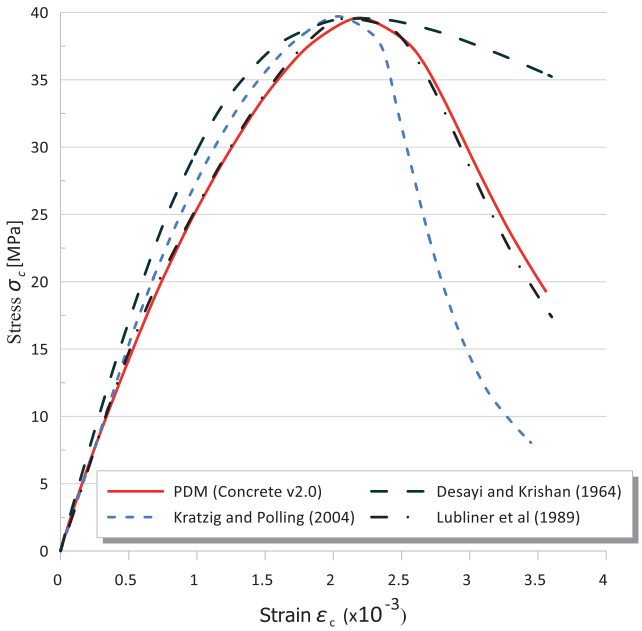

FIGURE 8. Compressive stress–strain curve for f_{cm} = 40 MPa
Source: own work.

For the tension case and in terms of Figures 9–13, the following notes can be made:

– The outcomes of the Barcelona model are consistent with the stress-strain curve generated according to the Lubliner's formula, which can be justified by the adopted hardening function that is identical to Lubliner's formulas.
– Using the decomposition of the tensile stress–strain curve that is illustrated in Figure 2b, the tensile curves of the Barcelona model are entirely consistent with the stress–strain curve generated according to the Thorenfeldt's formula in the first part. As for the second part, the Barcelona model gives results that are partly similar to the Thorenfeldt's formula.

Those observations are based mainly on the fact that the compressive and tensile stress–strain curves of the Barcelona model are calculated according to Lubliner's correlations that are used as a hardening function in our finite element implementation. To address another correlation, a simple modification in the finite element implementation of DPM will be required through re-computing, the derivative of the yield function with respect of stresses, the derivative of the yield function with respect of the inelastic compression strain.

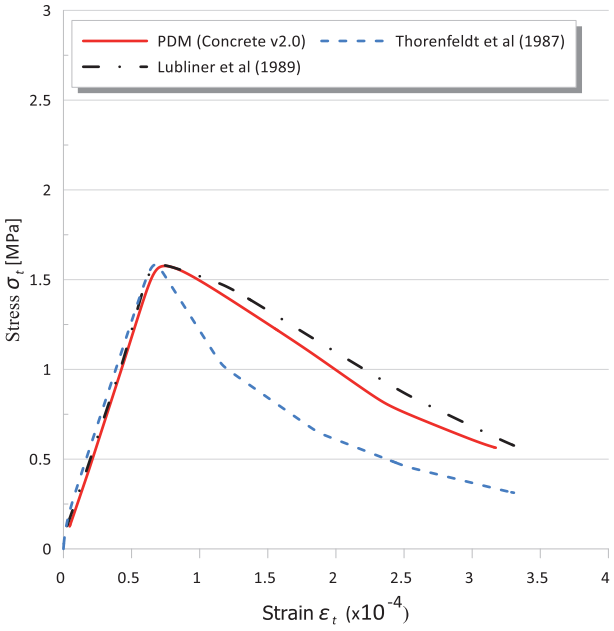

FIGURE 9. Tensile stress–strain curve for f_{cm} = 20 MPa (f_{tm} = 1.58 MPa)
Source: own work.

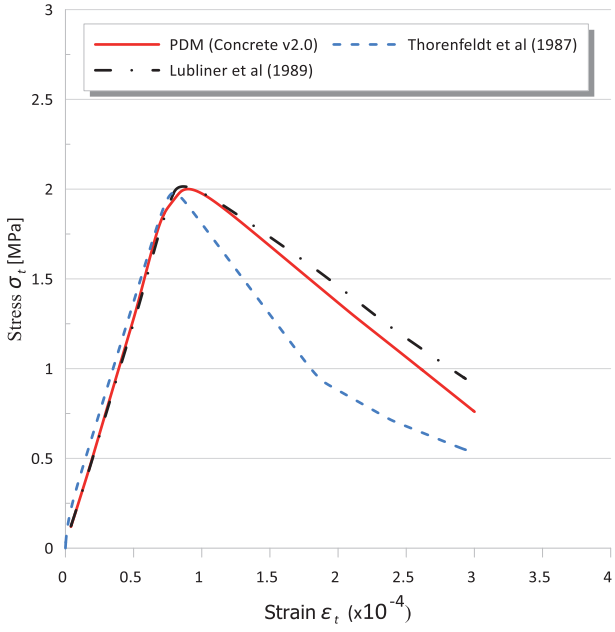

FIGURE 10. Tensile stress–strain curve for f_{cm} = 25 MPa (f_{tm} = 1.99 MPa)
Source: own work.

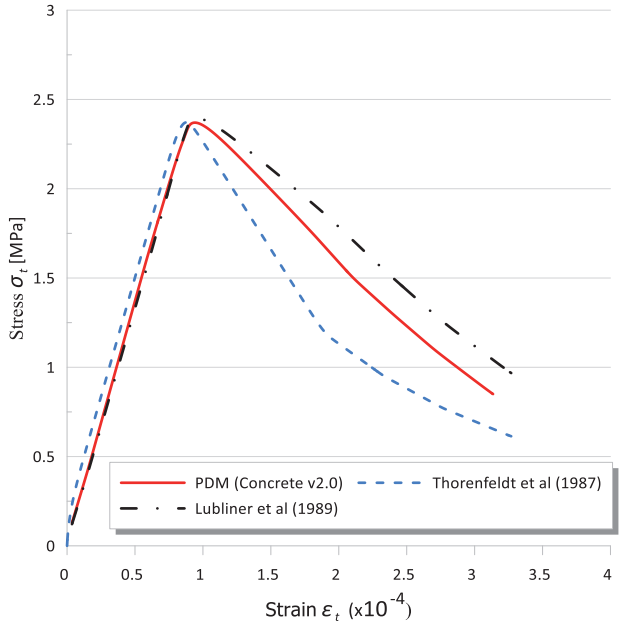

FIGURE 11. Tensile stress–strain curve for f_{cm} = 30 MPa (f_{tm} = 2.37 MPa)
Source: own work.

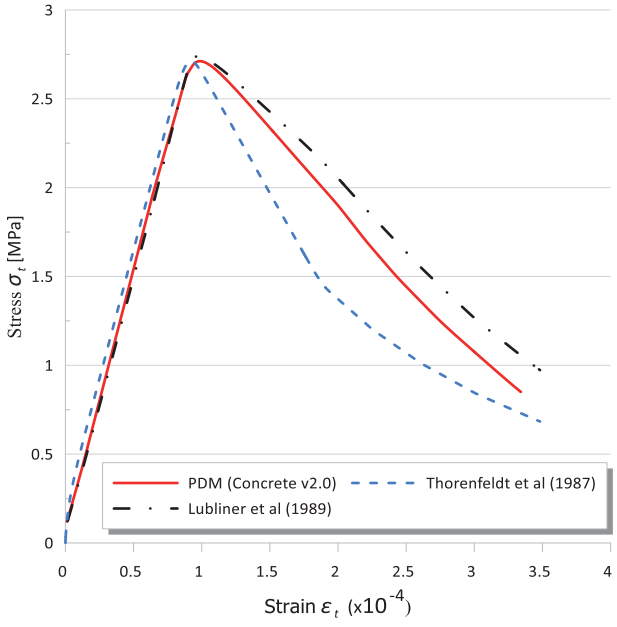

FIGURE 12. Tensile stress–strain curve for f_{cm} = 35 MPa (f_{tm} = 2.71 MPa)
Source: own work.

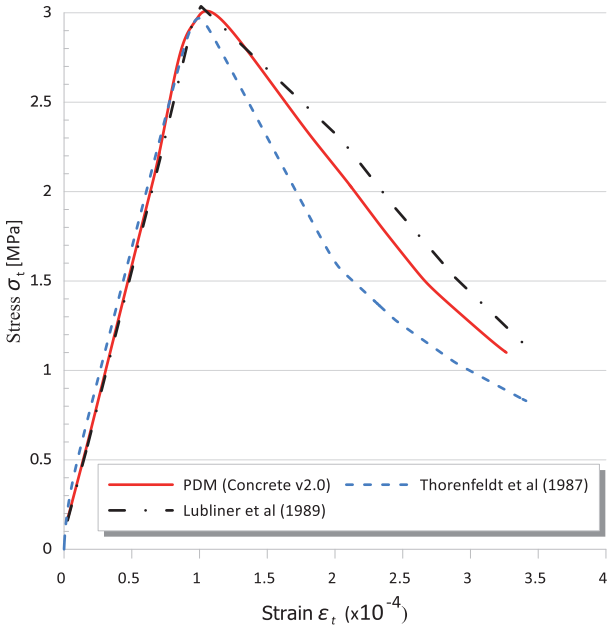

FIGURE 13. Tensile stress–strain curve for f_{cm} = 40 MPa (f_{tm} = 3.04 MPa)
Source: own work.

Conclusions

This paper has provided a comparative study of the stress–strain curves generated according to the Barcelona model and five stress–strain correlations in order to examine the effect of the hardening function in the final outcomes. For the compression case, the outcomes of the Barcelona model were compared with the stress–strain curves of Desayi, Krätzig and Lubliner. The following conclusions can be outlined:

– All curves are relatively close to each other in the ascending part.
– The curves of the Barcelona model are identical to the stress–strain curves generated by the Lubliner's formula.
– For concrete strengths less than 25 MPa, the curves of the Barcelona model are partly consistent with the stress–strain curve generated according to the Krätzig's formula. For values more than 25 MPa, the curves of the Barcelona model move away from the Krätzig's curve depending on the concrete strengths, especially in the descendant part.

– In the descendant part, the difference between the curves of the Barcelona model and of Desayi is significant.

For the tension case, the following conclusions can be made:

– All curves are relatively close to each other in the ascending part.
– The outcomes of the Barcelona model are consistent with the stress–strain curve generated according to the Lubliner's formula.
– The Barcelona model gives results partly similar to the Thorenfeldt's formula, especially in the descendant part.

Consequently, the outcomes of the Barcelona model depend mainly on the hardening function used. In our case, Lubliner's correlations are used as a hardening function in our finite element implementation of DPM (Concrete v. 2.0), which can justify the obtained results. The authors recommend extending the application field of DPM by changing the hardening function (stress–inelastic strain correlation) and re-computing the derivative of the yield function with respect to stresses and the derivative of the yield function with respect to the inelastic compression strain.

References

Ahmed, B., Voyiadjis, G. Z. & Park, T. (2020). Damaged plasticity model for concrete using scalar damage variables with a novel stress decomposition. *International Journal of Solids and Structures*, *191*, 56–75.

Alfarah, B., López-Almansa, F. & Oller, S. (2017). New methodology for calculating damage variables evolution in Plastic Damage Model for RC structures. *Engineering Structures*, *132*, 70–86.

Bakhti, R., Benahmed, B., Laib, A. & Alfach, M. T. (2022). New approach for computing damage parameters evolution in plastic damage model for concrete. *Case Studies in Construction Materials*, *16*, e00834.

Bhartiya, R., Sahoo, D. R. & Verma, A. (2021). Modified damaged plasticity and variable confinement modelling of rectangular CFT columns. *Journal of Constructional Steel Research*, *176*, 106426.

Comité euro-international du béton & Fédération internationale du béton [CEB-FIP] (2010). *Model Code 2010*. London: Thomas Telford.

Desayi, P. & Krishnan, S. (1964). Equation for the stress-strain curve of concrete. *Journal Proceedings*, *61* (3), 345–350.

Dvorkin, E. N., Cuitiño, A. M. & Gioia, G. (1989). A concrete material model based on non-associated plasticity and fracture. *Engineering Computations*, *6*, 281–294.

Han, D. J. & Chen, W. F. (1986). Strain-space plasticity formulation for hardening-softening materials with elastoplastic coupling. *International Journal of Solids and Structures*, *22* (8), 935–950.

Javanmardi, M. R. & Maheri, M. R. (2019). Extended finite element method and anisotropic damage plasticity for modelling crack propagation in concrete. *Finite Elements in Analysis and Design*, *165*, 1–20.

Krätzig, W. B. & Pölling, R. (2004). An elasto-plastic damage model for reinforced concrete with minimum number of material parameters. *Computers & Structures*, *82* (15–16), 1201–1215.

Lee, J. & Fenves, G. L. (1998). Plastic-damage model for cyclic loading of concrete structures. *Journal of Engineering Mechanics*, *124* (8), 892–900.

Liu, Z., Zhang, L., Zhao, L., Wu, Z. & Guo, B. (2022). A damage model of concrete including hysteretic effect under cyclic loading. *Materials*, *15* (14), 5062.

Lu, D., Meng, F., Zhou, X., Wang, G., & Du, X. (2022). Double scalar variables plastic-damage model for concrete. *Journal of Engineering Mechanics*, *148* (2), 1–52.

Lubliner, J., Oliver, J., Oller, S. & Oñate, E. (1989). A plastic-damage model for concrete. *International Journal of Solids and Structures*, *25* (3), 299–326.

Menetrey, P. & Willam, K. J. (1995). Triaxial failure criterion for concrete and its generalization. *Structural Journal*, *92* (3), 311–318.

Meng, H., Yang, W. & Yang, X. (2022). Real-time damage monitoring of double-tube concrete column under axial force. *Arabian Journal for Science and Engineering*, *47*, 12711–12728.

Minh, H. L., Khatir, S., Wahab, M. A. & Cuong-Le, T. (2021). A concrete damage plasticity model for predicting the effects of compressive high-strength concrete under static and dynamic loads. *Journal of Building Engineering*, *44*, 103239.

Oller, S., Oñate, E., Oliver, J. & Lubliner, J. (1990). Finite element nonlinear analysis of concrete structures using a "plastic-damage model". *Engineering Fracture Mechanics*, *35* (1–3), 219–231.

Othman, H. & Marzouk, H. (2018). Applicability of damage plasticity constitutive model for ultra-high performance fibre-reinforced concrete under impact loads. *International Journal of Impact Engineering*, *114*, 20–31.

Ottosen, N. S. (1977). A failure criterion for concrete. *Journal of the Engineering Mechanics Division*, *103* (4), 527–535.

Paliwal, B., Hammi, Y., Moser, R. D., & Horstemeyer, M. F. (2017). A three-invariant cap-plasticity damage model for cementitious materials. *International Journal of Solids and Structures*, *108*, 186–202.

Poliotti, M. & Bairán, J. M. (2019). A new concrete plastic-damage model with an evolutive dilatancy parameter. *Engineering Structures*, *189*, 541–549.

Ren, W., Sneed, L. H., Yang, Y. & He, R. (2015). Numerical simulation of prestressed precast concrete bridge deck panels using damage plasticity model. *International Journal of Concrete Structures and Materials*, *9* (1), 45–54.

Silva, M. A. L., Gamage, J. C. P. H. & Fawzia, S. (2019). Performance of slab-column connections of flat slabs strengthened with carbon fiber reinforced polymers. *Case Studies in Construction Materials*, *11*, e00275.

SIMULIA (2010). *Abaqus analysis user's manual. Volume III: Materials version 6.10*. Vélizy-Villacoublay: Dassault Systémes.

Thorenfeldt, E. (1987). Mechanical properties of high-strength concrete and applications in design. In I. Holand (Ed.), *Utilization of high strength concrete*. Proceedings: symposium in Stavanger, Norway, June 15-18, 1987 (pp. 149–159). Trondheim: Tapir.

Vermeer, P. A. & De Borst, R. (1984). Non-associated plasticity for soils, concrete and rock. *HERON*, *29* (3), 3–64.

Xiao, Y., Chen, Z., Zhou, J., Leng, Y. & Xia, R. (2017). Concrete plastic-damage factor for finite element analysis: Concept, simulation, and experiment. *Advances in Mechanical Engineering*, *9* (9), 1–10.

Summary

Investigation for stress–strain curves of the plastic damage model for concrete. The Barcelona model is one of the most widespread models used in the nonlinear finite element method for simulating the real behavior of concrete. The strong robustness of this model can be attributed to two main reasons, the first one being its ability to account for the elastic stiffness degradation induced by plastic straining and the second one the aptness of considering the stiffness recovery effects under cyclic loading. This model was examined in the paper by comparing the generated stress–strain diagrams with several analytical solutions from the literature. The comparing process in the compression and tension cases with the closed-form solutions of Desayi, Krätzig, Lubliner and Thorenfeldt proved that the Barcelona model provided identical outcomes with Lubliner's formula, which was used as the hardening function in the finite element implementation of this model. What is more, this model provided the same curves in case of the others in the ascending branches, and for the descending branch, this study proved that the outcomes of the Barcelona model are completely different from the ones of Desayi in the compression case and slightly similar to Thorenfeldt's curves in the tension case.

Scientific Review Engineering and Environmental Sciences (2023), 32 (1), 53–68

Sci. Rev. Eng. Env. Sci. (2023), 32 (1) https://srees.sggw.edu.pl

ISSN 1732-9353 (suspended) eISSN 2543-7496 DOI 10.22630/srees.4614

Received: 17.01.2023
Accepted: 12.02.2023

Oleksandr BORYSIUK[1]✉ https://orcid.org/0000-0002-0508-4851

Roman TRACH[1, 2] https://orcid.org/0000-0001-6654-9870

[1]National University of Water and Environmental Engineering, Ukraine
[2]Warsaw University of Life Sciences – SGGW, Institute of Civil Engineering, Poland

Calculation of the strength of reinforced concrete beams strengthened with composite materials

Keywords: reinforced concrete beam, testing of strength, composite materials, fiber--reinforced polymer (FRP)

Introduction

Nowadays, the question of improving the reliability and durability of structures and buildings remains urgent. During the operation of constructions, structures and buildings, there is a need to strengthen the load-bearing elements. This may occur due to the expiration of its service, changes in the structural design of the element, damage and non-operable or emergency state, increased operational loads, errors in design, construction and use of defective materials. There is also a tendency to strengthen buildings and structures during their restoration, especially those that are architectural monuments or have architectural value. This is explained by the fact that the replacement of structures is not always possible and sometimes not economically advantageous compared to their strengthening.

✉roman_trach@sggw.edu.pl

A popular and effective option to restore "old" buildings and structures in limited conditions of the construction site is the superstructure of one or more floors with the attic and replanning and arranging apartments with superior comfort. But even the use of modern lightweight building materials in the superstructure of buildings still requires strengthening of the bearing elements.

Industrial and civil engineering is characterized by the extensive use of reinforced concrete constructions, which is one of the main bearing elements of buildings and structures (Chen & Teng, 2001; Adhikary & Mutsuyoshi, 2004). Reinforced concrete bending elements (beams, slabs, trusses, etc.) were widely used in the past. Among the methods of strengthening reinforced concrete bending elements, one can choose two ways: strengthening the compressed zone of the concrete and the tensile zone of the section.

Research on the reliability assessment of strengthened concrete structures has been actively pursued since the beginning of the 21st century, primarily taking into account the effectiveness of the strengthening methods themselves, as well as the increase in the amount of work on the restoration and reconstruction of load-bearing elements of buildings and structures around the world (Islam, Mansur & Maalej, 2005; Kim, Ghannoum & Jirsa, 2016).

The strength of reinforced concrete structures deteriorates due to extreme environmental impacts and various types of loads. Effective retrofitting methods can allow elements to regain their structural strength. Different conventional and progressed strengthening methods, external prestressing, section enlargement and bonding of steel plates and modern materials such as externally bonded fiber-reinforced polymers (FRP), have been implemented for the rehabilitation of reinforced concrete structures.

Fiber-reinforced polymer (FRP) has been one of materials most often used for external reinforcement for about 30 years, and external bonding of FRP is currently the most common strengthening method. This type of polymer has the advantages of simplicity of construction, high strength, high resistance to corrosion and fatigue, and high strength-to-weight ratio.

A modern and effective way to strengthen structures of the tensile zone is to use the external reinforcing in the form of composite bands and liners (Trach et al., 2022). Strengthening reinforced concrete structures by glued external composite reinforcement on the basis of carbon fibers (CFRP) is a widely common practice. Strengthening structures in the tensile zone allows both to eliminate defects, acquired by the structure being in operation, and to increase the bearing capacity and rigidity of the element. The externally bonded carbon fiber-reinforced plastic (CFRP) has often been used due to its cost-effectiveness, high corrosion resistance, improved struc-

tural performance under critical loading conditions, high strength-to-weight ratio, and flexibility in use and low thermal conductivity. The strengthening of undershear members with CFRP is an effective method to increase the shear capacity (Bourget, El-Saikaly & Chaallal, 2017).

El-Mandouh, Hu, Shim, Abdelazeem and ELsamak (2022) examined various methods of increasing the torsional strength of reinforced concrete beams. An experimental study was conducted using six different strengthening systems: wrapped aluminum strips with anchor bolts, wrapped stainless steel strips with anchor bolts, wrapped glass fiber reinforced polymer (GFRP), one layer of the wrapped steel wire, and two layers of the wrapped steel wire along the beam. The results showed that the ultimate torque of the beam strengthened with aluminum wrapped strips and the beam strengthened with stainless steel wrapped strips was greater than the control beam by about 32% and 40%, respectively. The ultimate torque of beams strengthened with GFRP, single-layer wrapped steel wire mesh, and double-layer wrapped steel wire mesh along the beam exceeds the control beam by about 62%, 118%, and 163%, respectively.

The textile reinforced concrete (TRC) system is actively used to repair and strengthen worn reinforced concrete structures. Kim, You and Ryu (2021) proposed an enhanced method of installing the TRC system by cementing to strengthen the worn reinforced concrete structures. Four reinforced concrete slabs were strengthened with one layer of carbon textile mesh and 20-milimeter thick cement mortar. Specimens of the strengthened TRC plates were tested for bending and then the test results were compared with the results of the non-strengthened specimen and the theoretical solutions.

Park, Park and Hong (2021) explored the method of strengthening using the textile-reinforced mortar (TRM) – a structural reinforcing material in which a textile consists of fibers with high level of strength and chemical resistance. It is attached to the masonry surface and reinforced concrete structures using a cement mortar matrix. The strength limit of the TRM beam was determined taking into account the possibility of premature failure and the experimental results of four other studies on various samples. The authors of this study proposed a method to evaluate the flexural behavior of TRM beams considering a premature failure due to bond uncertainty and attempts to determine under the working load.

Also, Park, You, Park and Hong (2022) researched the flexural behavior of TRM-strengthened beams and their fatigue performance using carbon and alkali resistant (AR) glass textiles after 200 000 loading cycles. The TRM-reinforced beams were subjected to an optimization strengthening method that checked whether the textile was straightened. According to the test results, the strengthening

efficiency of TRM-strengthened beams under cyclic loading was lower than under monotonic loading, except for the straightened carbon textile sample.

Clearly, carbon fiber reinforced polymers (CFRP) have shown significant potential in the repair and rehabilitation of damaged reinforced concrete structures. Currently, several schemes for strengthening reinforced concrete structures with carbon fiber have been studied and applied in a practical manner.

Haroon, Moon and Kim (2021) designed and executed a test program to evaluate the potential use and shear performance of bidirectional CFRP-strengthened rectangular RC beams. A total of 18 beams were designed and tested for the purpose of evaluating various CFRP strengthening characteristics such as strengthening time, presence of CFRP anchors, CFRP layout, etc. The bidirectional CFRP scheme allowed for a more uniform distribution of stirrup deformation compared to the unidirectional CFRP layout at the same load level, which increased the effectiveness of the transverse reinforcement. In addition, the contribution of the CFRP material to the shear was tested according to the CFRP hardening time.

The research of Wang, Ellingwood and Zureick (2010) is more advanced than the previous study, from the point of view of taking into account the joint work of the elements of the reinforced concrete structure and the approach to assessing its reliability. They proposed a method for assessing the reliability of bending reinforced concrete elements strengthened by external fastening of FRP composites. The most important advantage of this technique is that it is applied to strengthened reinforced concrete elements with insufficient bending strength. This study clearly demonstrated the possibility of developing a method for determining the reliability of bending reinforced concrete elements strengthened under the action of load with FRP plates, based on reaching the boundary state in accordance with the American building codes ACI 318-05 (American Concrete Institute [ACI], 2017). In turn, FRP-plates are included in the structure work at a certain stage and increase its strength and deformability. Moreover, in order to assess the reliability of strengthened structures, the scientists in their research used not only reinforced concrete beams as bending elements, but also slabs.

However, along with the progressive solutions developed in all of the works above, the problem of assessing the reliability of structures strengthened under the action of the load remaining open. The authors (Koutas & Triantafillou, 2013; Borysiuk, Ziatiuk, Lysyuk & Yevtushenko, 2018; Karavan, Borysiuk & Filipchuk, 2022a) conducted a number of experimental studies that allow for a more realistic assessment of the performance of strengthened reinforced concrete bending elements.

Material and methods

Stress and strain state of normal sections of the bending reinforced concrete element with single reinforcing, which is strengthened by the layer of any type of concrete h_{cf} in thickness in the compressed zone, and in the tensile zone it is strengthened by the carbon band in dimension of $b_{sf} \times h_{sf}$ is given at Figure 1.

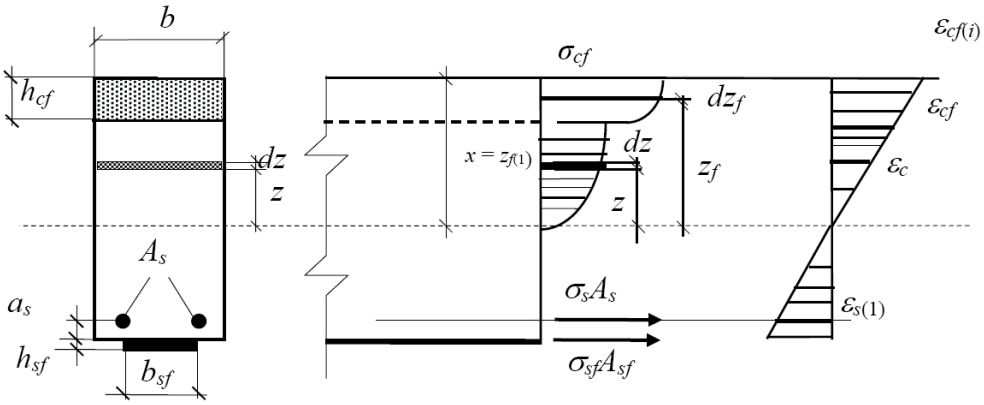

FIGURE 1. Stress and strain state of normal section of the bending reinforced concrete element strengthened in the compressed and tensile zones

Source: own elaboration.

In addition to the established prerequisites (Borysiuk & Ziatiuk, 2020; Karavan, Borysiuk & Filipchuk, 2022b) for the strengthened elements, we assume that: bonding the strengthening materials with concrete of the strengthening structure provides reliable joint work of adjacent fibers, the cross-section is considered as solid; when strengthening the tensile zone by carbon bands, the resultant force in the band is applied at the joint level (Norris, Saadatmanesh & Ehsani, 1997); mechanical condition of concrete in compression is described by dependence.

$$\sigma_c = f_{(ck),(cd)} \sum_{k=1}^{5} a_k \left(\frac{\varepsilon_c}{\varepsilon_{c1}} \right)^k = f_{(ck),(cd)} \left[a_1 \frac{\varepsilon_c}{\varepsilon_{c1}} + a_2 \left(\frac{\varepsilon_c}{\varepsilon_{c1}} \right)^2 + a_3 \left(\frac{\varepsilon_c}{\varepsilon_{c1}} \right)^3 a_4 \left(\frac{\varepsilon_c}{\varepsilon_{c1}} \right)^4 + a_5 \left(\frac{\varepsilon_c}{\varepsilon_{c1}} \right)^5 \right]. \quad (1)$$

Borysiuk, O., Trach, R. (2023). Calculation of the strength of reinforced concrete beams strengthened with composite materials. *Sci. Rev. Eng. Env. Sci.*, *32* (1), 53–68. DOI 10.22630/srees.4614

The destruction of the element can occur when deformations are achieved in the extreme fibers of the material of strengthening boundary values ε_{cfu1}, and in tensile zone there may be a rupture of the strengthening material as a result of reaching the boundary deformations ε_{fu} therein; when exceeding deformations in the strengthening materials in the tensile zone, the value $\varepsilon_{f0}(\varepsilon_{f0} = f_{yf}/E_f)$ – the stresses in it are taken to be $\sigma_{sf} = f_{yf}$.

At a given deformation of the extreme compressed fiber of the strengthening material $\varepsilon_{cf(1)}$ according to the Bernoulli hypothesis (Fig. 1), the deformations in other materials can be determined thanks to the formulas (Borysiuk, Karavan & Sobczak-Piąstka, 2019):

$$\varepsilon_{s(1)} = \frac{\varepsilon_{cf(1)}}{z_{f(1)}}\left(h - z_{f(1)} - a_s\right), \tag{2}$$

$$\varepsilon_{sf(1)} = \frac{\varepsilon_{cf(1)}}{z_{f(1)}}\left(h - z_{f(1)}\right), \tag{3}$$

$$\varepsilon_{cf} = \frac{\varepsilon_{cf(1)}}{z_{f(1)}} z_f; \varepsilon_c = \frac{\varepsilon_{cf(1)}}{z_{f(1)}} z, \tag{4}$$

$$\varepsilon_{cfc} = \frac{\varepsilon_{cf(1)}}{z_{f(1)}}\left(z_{f(1)} - h_{cf}\right), \tag{5}$$

where ε_{cfc} is a deformation of the adjacent fiber of strengthening concrete and existing concrete.

Values z and dz when $\varepsilon_{c(1)} = \varepsilon_{cf(1)}$, and then z_f and dz_f are defined by formulas:

$$z_f = \frac{z_{f(1)}}{\varepsilon_{cf(1)}} \varepsilon_{cf}; dz_f = \frac{z_{f(1)}}{\varepsilon_{cf(1)}} d\varepsilon_{cf}. \tag{6}$$

The z value can also be expressed as follows $z = z_f - h_{cf}$, and when $z_f \leq h_{cf}$, take $z_f = 0$.

For the strengthened section, the balance conditions in general form can be viewed as:

$$M_{cf(1)} + M_{c(1)} + M_{sf(1)} + M_{s(1)} - M = 0, \tag{7}$$

$$S_{cf(1)} + S_{c(1)} = S_{sf(1)} + S_{s(1)}, \tag{8}$$

where: M; $M_{cf(1)}$; $M_{c(1)}$; $M_{sf(1)}$; $M_{s(1)}$ – values according to the bending moment from the action of the external loads and internal force moments in the compressed strengthening concrete and the primary concrete, in the tension band of strengthening and in the main reinforcement at $\varepsilon_{cf} = \varepsilon_{cf(1)}$; $S_{cf(1)}$; $S_{c(1)}$; $S_{sf(1)}$; $S_{s(1)}$ – internal forces in the compressed concrete of strengthening, in the primary concrete, in the strengthening material and in the tensile reinforcement A_s at $\varepsilon_{cf} = \varepsilon_{cf(1)}$.

Forces in the compressed concrete of strengthening can be found using a formula at a given deformation of the compressed extreme fiber – $\varepsilon_{cf(1)}$

$$S_{cf(1)} = b\int_{z_{f(1)}-h_{cf}}^{z_{f(1)}} \sigma_{cf} dz_f = b\frac{z_{f(1)}}{\varepsilon_{cf(1)}}\int_{\varepsilon_{cfc(1)}}^{\varepsilon_{cf(1)}} \sigma_{cf} d\varepsilon_f. \tag{9}$$

And then, in the concrete of the element which is strengthening

$$S_{c(1)} = b\int_{0}^{z_{f(1)-h_{cf}}} \sigma_c dz = b\frac{z_{(1)}}{\varepsilon_{cf(1)}}\int_{0}^{\varepsilon_{cfc(1)}} \sigma_c d\varepsilon_c. \tag{10}$$

After integration and mathematical transformation of Eqs (7) and (8) and taking into account Eq. (1) we get:

$$S_{cf(1)} = \omega_f f_{cfm} b z_{f(1)}; S_{c(1)} = \omega f_{cm} b z_{f(1)}, \tag{11}$$

where: f_{cfm} – average prism strength of strengthening concrete; ω – coefficient determined by the formula $\omega = \sum_{k=1}^{5} \frac{a_k}{k+1}\left(\frac{\varepsilon_{c(1)}}{\varepsilon_{c1,cm}}\right)^k$ when $\varepsilon_{c(1)} = \varepsilon_{cf(1)}$; ω_f – coefficient determined by the formula

$$\omega_f = \sum_{k=1}^{5} \frac{a_k}{k+1}\left(\frac{\varepsilon_{cf(1)}^{k+1} - \varepsilon_{cfc(1)}^{k+1}}{\varepsilon_{cf1}^{k+1}}\right), \tag{12}$$

where: ε_{cf1} – deformation under maximum stresses in the diagram of mechanical condition of strengthening concrete.

Borysiuk, O., Trach, R. (2023). Calculation of the strength of reinforced concrete beams strengthened with composite materials. *Sci. Rev. Eng. Env. Sci.*, *32* (1), 53–68. DOI 10.22630/srees.4614

Internal forces in the reinforcement and in the strengthening band are determined by the following formulas:

$$S_{s(1)} = A_s\sigma_{s(1)} = A_sE_s\varepsilon_{s(1)} = A_sE_s\frac{\varepsilon_{cf(1)}}{z_{f(1)}}\left(h - z_{f(1)} - a_s\right), \tag{13}$$

$$S_{sf(1)} = A_{sf}\sigma_{sf(1)} = A_{sf}E_f\varepsilon_{sf(1)} = A_{sf}E_f\frac{\varepsilon_{cf(1)}}{z_{f(1)}}\left(h - z_{f(1)}\right). \tag{14}$$

In the same way, to determine the bending moment in the normal section of the element about the zero axis at a given deformation of the extreme compressed fiber, we can obtain the formulas:

$$M_{cf(1)} = b\int_{z_{f(1)}-h_{cf}}^{z_{f(1)}}\sigma_{cf}z_f dz_f = b\left(\frac{z_{f(1)}}{\varepsilon_{cf(1)}}\right)^2\int_{\varepsilon_{cfc(1)}}^{\varepsilon_{cf(1)}}\sigma_{cf}\varepsilon_{cf}d\varepsilon_f = \beta_f f_{cfm}bz_{f(1)}^2, \tag{15}$$

$$M_{cf(1)} = b\int_0^{z_{f(1)}-h_{cf}}\sigma_c z dz = b\left(\frac{z_{f(1)}}{\varepsilon_{cf(1)}}\right)^2\int_0^{\varepsilon_{cfc(1)}}\sigma_c\varepsilon_c d\varepsilon_c = \beta f_{cm}bz_{(1)}^2, \tag{16}$$

$$M_{s(1)} = A_sE_s\varepsilon_{s(1)} = A_sE_s\frac{\varepsilon_{cf(1)}}{z(1)}\left(h - z_{f(1)} - a_s\right)^2, \tag{17}$$

$$M_{sf(1)} = A_{sf}E_f\varepsilon_{sf(1)} = A_{sf}E_f\frac{\varepsilon_{cf(1)}}{z_{f(1)}}\left(h - z_{f(1)}\right)^2, \tag{18}$$

where the β coefficient is determined by the formula

$$\beta = \sum_{k=1}^{5}\frac{a_k}{k+2}\left(\frac{\varepsilon_{c(1)}}{\varepsilon_{c1,cm}}\right)^k \quad \text{at} \quad \varepsilon_{c(1)} = \varepsilon_{cf(1)}, \tag{19}$$

whereas the β_f coefficient – by the formula

$$\beta_f = \sum_{k=1}^{5}\frac{a_k}{k+2}\left(\frac{\varepsilon_{cf(1)}^{k+2} - \varepsilon_{cfc(1)}^{k+2}}{\varepsilon_{cf1}^{k+2}}\right). \tag{20}$$

Maximum (breaking) bending moment (M_u) is found by a joint solution of Eqs (7) and (8) considering values of the internal forces at Eqs (9), (11), (12), and (13)–(18), calculating them at $M = M_u$. The maximum criterion is used for this purpose. In order to do that, the values of the moments are determined when the extreme deformation of strengthening concrete ε_{cf} with certain step, for example at $0.1\varepsilon_{cf1}$, is being changed. At each step, the problem is solved by the successive method of approximation, for which it is possible to take the height of the compressed zone $x = z_{(1)} = 0.5$d at the first step and check the statement of Eq. (7). If the difference between the left and the right parts of Eq. (7) is less than 5%, then we can assume that the $z_{(1)}$ value is correct. If the difference between them exceeds 5%, then it is necessary to make a correction of the z value until the equation statement (8) is satisfied. We find the value of the M moment from the determined z value of Eq. (6). These calculations are repeated at each step.

Based on the performed calculations, a complex of indicators of stress and strain state of the normal section (deformations of the materials and stresses in them, forces, curvature, etc.) is obtained at each stage of the calculations, which can be shown in table form and in the diagram of the mechanical condition of the section. The maximum (breaking) moment is selected from the table or defined as the maximum in the diagram of the mechanical condition of the normal section.

The balance equation presented above can be used in the calculations of the normal section's strength at the boundary states of the first group under the action of the calculated moment from the external loading (M_{Ed}), at that, the above formulas use the calculated values of the strength and deformation characteristics of the materials. In this case, the strength of the normal strengthened section of the bending element will be provided, when the following equations is fulfilled

$$M_{Ed} \le \beta_f f_{cfd} b z_{f(1)}^2 + \beta f_{cd} b z_{f(1)}^2 + A_{sf} E_f \frac{\varepsilon_{cf(1)}}{z_{f(1)}} \left(h - z_{f(1)}\right)^2 + A_s E_s \frac{\varepsilon_{cf(1)}}{z_{(1)}} \left(h - z_{f(1)} - a_s\right)^2, \quad (21)$$

$$\omega_f f_{cfd} b z_{f(1)} + \omega f_{cd} b z_{(1)} = A_s E_f \frac{\varepsilon_{cf(1)}}{z_{f(1)}} \left(h - z_{f(1)}\right) + A_s E_s \frac{\varepsilon_{cf(1)}}{z_{f(1)}} \left(h - z_{f(1)} - a_s\right). \quad (22)$$

Results and discussion

To carry out the experimental research, eight 2000 mm long beams with a 200 × 100 mm cross-section were produced from concrete, which has the prism strength $f_{cm,prism}$ = 13.9 MPa. Beams are reinforced by two rods with a 10 mm

Borysiuk, O., Trach, R. (2023). Calculation of the strength of reinforced concrete beams strengthened with composite materials. *Sci. Rev. Eng. Env. Sci.*, *32* (1), 53–68. DOI 10.22630/srees.4614

diameter of the A500C class. The 6 mm diameter cross roads of the A240C class are placed with the 50 mm spacing (Figs 2 and 3).

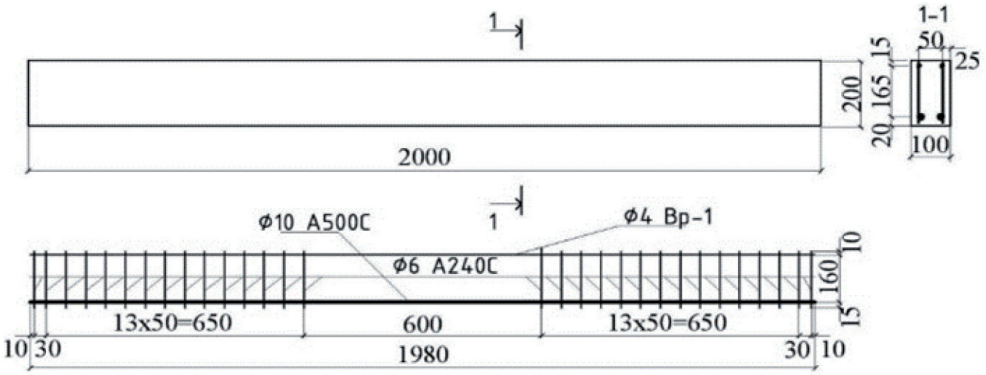

FIGURE 2. Structural scheme of non-strengthened analyzing beams
Source: own elaboration.

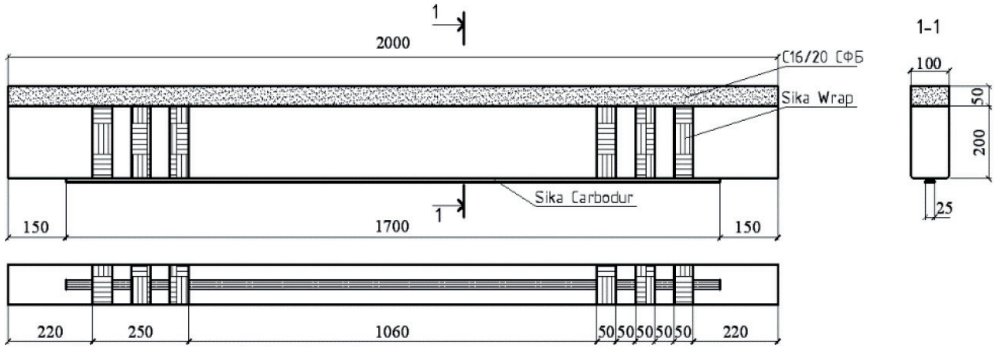

FIGURE 3. Scheme of strengthening analyzing beams by the band and by the concrete
Source: own elaboration.

The calculation of the bearing capacity of the normal section, conducted according to the above-described method (for non-strengthened beams), shows a fine precision of the results. Divergence of the theoretical results of the calculation, compared to the experimental data, accounts for 1.5% and 3%. This approach fully takes into account all factors that affect the bearing capacity of the normal section of the beam.

When determining the theoretical value of the breaking moment according to the above method, the following material characteristics were assumed: the yield point for the reinforcement f_{yk} = 500 MPa; modulus of elasticity $E_s = 21 \cdot 10^4$ MPa;

concrete deformations under maximum stresses in the deformation diagram $\varepsilon_{c1} = 0.00161$; boundary deformations of the concrete compression $\varepsilon_{cu1} = 0.0044$.

Two beams (B-1, B-2) were tested without strengthening (Fig. 2), the rest were strengthened in the tensile zone by gluing the carbon band Sika with the cross section 25 × 5 mm, which was anchored by the cross-section reinforcement in the form of SikaWrap® liner strips. In the compressed zone, two beams (B-3, B-4) were strengthened by a layer of fine-grained concrete ($f_{cfm,prism} = 13.5$ MPa) 50 mm thick, and two beams (B-5, B-6) – by a layer of steel fiber concrete with a fiber content of 3% ($f_{cfm,prism} = 16.4$ MPa), also 50 mm thick (Fig. 3). Testing of the beams were performed by the scheme of the simple bending (Karavan, Borysiuk & Filipchuk, 2022b). According to the calculations, the theoretical breaking moment of the non-strengthened beams was $M_{teor} = 13.6$ kN·m^{-1}, the experimental one – $M_{exp} = 13.4$ kN·m^{-1}, 14.0 kN·m^{-1}. Divergence between the experimental value of the breaking moment in the normal section of the beam and the theoretical value accounted for 3%.

Two beams strengthened by the fine-grained concrete in the compressed zone (Fig. 4) and by the carbon band in the tensile zone were destructed under the action of the external moment 21.13 kN·m^{-1} and 21.52 kN·m^{-1} accordingly, which on the average is $M_u = 21.32$ kN·m^{-1}.

Two beams, strengthened by the steel fiber concrete in the compressed zone (Fig. 4), and in the tensile zone by the carbon band, were destructed under the action of the external moment 20.91 and 21.96 kN·m^{-1} accordingly, which on the average is $M_{u,BPsfb} = 21.4$ kN·m^{-1}.

When determining the breaking theoretical moment, we took the following strengthening material characteristics into consideration: the yield point of the carbon band $f_f = 3\,100$ MPa; modulus of elasticity of the band $E_f = 16.5 \cdot 10^4$ MPa; average prism strength of the steel fiber concrete $f_{cfm} = 16.4$ MPa; steel fiber concrete deformations at maximum stresses in the deformation diagram $\varepsilon_{cf1} = 0.00166$; boundary deformations of the concrete in compression $\varepsilon_{cfu1} = 0.00434$.

During the experiment, the deformations in the compressed zone of the concrete and the stretched reinforcement were recorded, the width of the opening of cracks and deflections of the structure were observed. When calculating the load-bearing capacity, the actual values of the prism strength of the concrete were substituted in the formula, and the actual values of the yield points of the reinforcement were taken as the calculated resistance of the reinforcement.

The test of the beams turned out to be 10% of the theoretically calculated bearing capacity. In order to remove the readings of the devices, to fix the development and change the width of the opening of the cracks, after applying each degree of load, exposures of 5–10 min were made.

Borysiuk, O., Trach, R. (2023). Calculation of the strength of reinforced concrete beams strengthened with composite materials. *Sci. Rev. Eng. Env. Sci.*, *32* (1), 53–68. DOI 10.22630/srees.4614

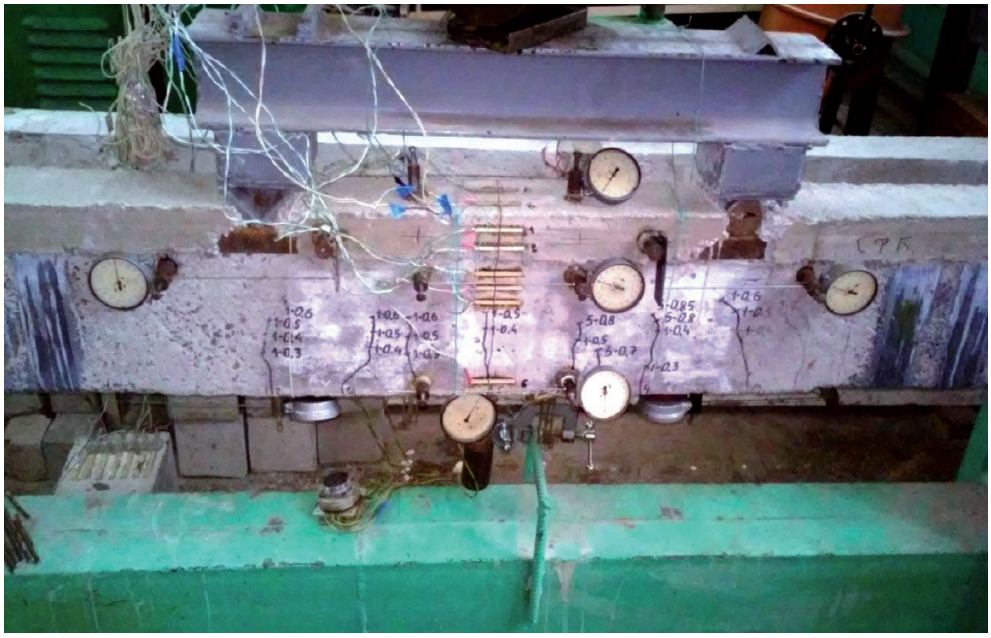

FIGURE 4. Overall view of testing the strengthened beams
Source: own elaboration.

The calculation of the strength of the normal sections of the beams, strengthened in the compressed and tensile zones by the steel fiber concrete and composite materials accordingly, showed a decrease in theoretical results. As the calculation does not consider anchorage of the band, it only takes into account the bearing capacity of the strengthening section. The experimental indicators exceeded theoretical 1.23, …, 1.33.

According to the experimental data it was stated that due to anchoring of the bands by the liner, and increased strength characteristics of the steel fiber concrete, the bearing capacity of the normal sections of the reinforced concrete beams increased compared to the non-strengthened ones by 40–60%.

When calculating the strength of the normal strengthened section of the bending element, it is proposed to introduce the coefficient that takes into account an increase of the bearing capacity of the normal sections of the strengthened reinforced concrete beams by anchoring the bands of strengthening, into Eq. (17). Formula (21) will take the following form

$$M_{Ed} \le \left[\beta_f f_{cfd} b z_{f(1)}^2 + \beta f_{cd} b z_{(1)}^2 + A_{sf} E_f \frac{\varepsilon_{cf(1)}}{z_{f(1)}} \left(h - z_{f(1)} \right)^2 + A_s E_s \frac{\varepsilon_{cf(1)}}{z_{(1)}} \left(h - z_{f(1)} - a_s \right)^2 \right] P_{CFRP}^{SFC}, \quad (23)$$

β – coefficient determined by Eq. (19) when $\varepsilon_{c(1)} = \varepsilon_{cf(1)}$; β_f – coefficient calculated using Eq. (20); P_{CFRP}^{SFC} – coefficient that takes into account an increase of bearing capacity strength of the normal sections of the strengthened reinforced concrete beams when anchoring the strengthening bands, and it is assumed by the experimental data. If the data are absent, the value of this coefficient can equal 1.25.

The results of experimental research and comparison with theoretical calculations are presented in Table 1.

TABLE 1. Results of experimental research

Beam	Strengthening elements cross section area		Internal steel reinforcement area	Experimental bending moment	Calculated bending moment*	Divergence with experimental value	Calculated bending moment according to the proposed method	Divergence with the experimental value
	A_{sf} [cm^2]	A_{cf} [cm^2]	A_s [cm^2]	M^{exp} [kN·m^{-1}]	M^{norm} [kN·m^{-1}]	δ [%]	M × P_{CFRP}^{SFC} [kN·m^{-1}]	δ [%]
B-1	0	0	1.57	13.4	13.6	1.5	13.2	–1.5
B-2	0	0	1.57	14.0	13.6	–2.9	13.2	–5.7
B-3	1.25	50	1.57	21.13	18.3	–14.4	21.25	0.6
B-4	1.25	50	1.57	21.52	18.3	–15.0	21.25	–1.3
B-5	1.25	50	1.57	21.96	19.0	–13.5	21.62	–1.6
B-6	1.25	50	1.57	20.91	19.0	–9.8	21.62	3.3

*According to the Ukrainian standard DSTU-NB V. 1.2-18:2016 (DP UkrNDTS, 2017).

Source: own elaboration.

Conclusions

The use of modern and highly efficient materials, namely fiber concrete and composite materials based on the carbon fibers, to strengthen the compressed and tensile zones of the reinforced concrete bending structures, is a promising trend in view of the advantages of these materials over the traditional ones because they can be easily and quickly set up and be reliable in the further operation. The calcu-

lation of the strengthened bending reinforced concrete elements in the compressed and tensile zones of the section based on carbon fiber reinforced plastics and fiber concrete for the first group of boundary states, which we suggested, gives good results from all currently proposed methods.

Acknowledgements

This article is dedicated to the bright memory of the author Oleksandr Borysiuk (1954–2023). Rest in peace.

References

Adhikary, B. B. & Mutsuyoshi, H. (2004). Behavior of concrete beams strengthened in shear with carbon-fiber sheets. *Journal of Composites for Construction*, *8* (3), 258–264. https://doi.org/10.1061/(ASCE)1090-0268(2004)8:3(258)

American Concrete Institute [ACI] (2017). *Building code requirements for structural concrete* (ACI 318-05). Farmington Hills, MI: American Concrete Institute.

Borysiuk, O., Karavan, V. & Sobczak-Piąstka, J. (2019). Calculation of the normal section strength, rigidity and crack resistance of beams, strengthened by carbon-fiber materials. *AIP Conference Proceedings*, *2077* (1), 020008. https://doi.org/10.1063/1.5091869

Borysiuk, O. & Ziatiuk, Y. (2020). Experimental research results of the bearing capacity of the reinforced concrete beams strengthened in the compressed and tensile zones. In *Proceedings of EcoComfort 2020* (pp. 63–70). Cham: Springer International Publishing.

Borysiuk, O. P., Ziatiuk, Y. Y., Lysyuk, M. O. & Yevtushenko V. S. (2018). Strengthening and calculation analysis of bending reinforced concrete elevents. *Resource-Economic Materials, Constructions, Buildings and Structures*, *36*, 341–348. https://doi.org/10.31713/budres.v0i36.284

Bourget, S., El-Saikaly, G. & Chaallal, O. (2017). Behavior of reinforced concrete T-beams strengthened in shear using closed carbon fiber-reinforced polymer stirrups made of laminates and ropes. *ACI Structural Journal*, *114* (5), 1087. https://doi.org/10.14359/51700786

Chen, J. F. & Teng, J. G. (2001). Anchorage strength models for FRP and steel plates bonded to concrete. *Journal of Structural Engineering*, *127* (7), 784–791. https://doi.org/10.1061/(ASCE)0733-9445(2001)127:7(784)

DP UkrNDTS (2017). *Nastanova shchodo obstezhennya budivel i sporud dlya vyznachennya ta otsinky yikh tekhnichnoho stanu* [*Instructions on the inspection of buildings and structures to determine and assess their technical condition*] (DSTU-NB V. 1.2-18:2016). Kyyiv.

El-Mandouh, M. A., Hu, J. W., Shim, W. S., Abdelazeem, F. & ELsamak, G. (2022). Torsional improvement of RC beams using various strengthening systems. *Buildings*, *12* (11), 1776. https://doi.org/10.3390/build)ings12111776

Haroon, M., Moon, J. S. & Kim, C. (2021). Performance of reinforced concrete beams strengthened with carbon fiber reinforced polymer strips. *Materials*, *14* (19), 5866. https://doi.org/10.3390/ma14195866

Islam, M. R., Mansur, M. A. & Maalej, M. (2005). Shear strengthening of RC deep beams using externally bonded FRP systems. *Cement and Concrete Composites*, *27* (3), 413–420. https://doi.org/10.1016/j.cemconcomp.2004.04.002

Karavan, V. V., Borysiuk, O. P. & Filipchuk, S. (2022a). Technical condition and remaining resource of reinforced concrete bridges on automobile roads in the city of Rivne. *Resource--Economic Materials, Constructions, Buildings and Structures*, *39*, 237–244. https://doi.org/10.31713/budres.v0i39.26

Karavan, V. V., Borysiuk, O. P. & Filipchuk, S. (2022b). Technical condition of the reinforced concrete bridge on the T-14-04 Chervonograd – Rava-Ruska road. *Resource-Economic Materials, Constructions, Buildings and Structures*, *40*, 251–259. https://doi.org/10.31713/budres.v0i40.29

Kim, C., Ghannoum, W. M. & Jirsa, J. O. (2016). Behavior of reinforced concrete panels strengthened with carbon fiber-reinforced polymers. *ACI Structural Journal*, *113* (5), 1077. https://doi.org/10.14359/51689031

Kim, H. Y., You, Y. J., & Ryu, G. S. (2021). Reinforced concrete slabs strengthened with carbon textile grid and cementitious grout. *Materials*, *14* (17), 5046. https://doi.org/10.3390/ma14175046

Koutas, L. & Triantafillou, T. C. (2013). Use of anchors in shear strengthening of reinforced concrete T-beams with FRP. *Journal of Composites for Construction*, *17* (1), 101–107. https://doi.org/10.1061/(ASCE)CC.1943-5614.0000316

Norris, T., Saadatmanesh, H. & Ehsani, M. R. (1997). Shear and flexural strengthening of R/C beams with carbon fiber sheets. *Journal of Structural Engineering*, *123* (7), 903–911. https://doi.org/10.1061/(ASCE)0733-9445(1997)123:7(903)

Park, J., Park, S. K. & Hong, S. (2021). Evaluation of flexural behavior of textile-reinforced mortar-strengthened RC beam considering strengthening limit. *Materials*, *14* (21), 6473. https://doi.org/10.3390/ma14216473

Park, J., You, J., Park, S. K. & Hong, S. (2022). Flexural Behavior of Textile Reinforced Mortar-Strengthened Reinforced Concrete Beams Subjected to Cyclic Loading. *Buildings*, *12* (10), 1738. https://doi.org/10.3390/buildings12101738

Trach, R., Moshynskyi, V., Chernyshev, D., Borysiuk, O., Trach, Y., Striletskyi, P. & Tyvoniuk, V. (2022). Modeling the quantitative assessment of the condition of bridge components made of reinforced concrete using ANN. *Sustainability*, *14* (23), 15779. https://doi.org/10.3390/su142315779

Wang, N., Ellingwood, B. R. & Zureick, A. H. (2010). Reliability-based evaluation of flexural members strengthened with externally bonded fiber-reinforced polymer composites. *Journal of Structural Engineering*, *136* (9), 1151–1160. https://doi.org/10.1061/(ASCE)ST.1943-541X.0000199

Borysiuk, O., Trach, R. (2023). Calculation of the strength of reinforced concrete beams strengthened with composite materials. *Sci. Rev. Eng. Env. Sci.*, *32* (1), 53–68. DOI 10.22630/srees.4614

Summary

Calculation of the strength of reinforced concrete beams strengthened with composite materials. Currently, in view of the previous theoretical and experimental researches, the regulatory documents for the calculation of reinforced concrete elements strengthened by composite materials and the calculation and design of fiber reinforced concrete structures are in force in Ukraine and in the world. Simultaneous strengthening of the compressed and tensile zones has not been sufficiently studied. Therefore, further research of reinforced concrete elements, strengthened by modern and highly efficient materials, such as steel fiber concrete and composite materials, is of great theoretical and practical importance. The urgency of the study is due to the obvious need to improve the method of calculation of the reinforced concrete bending elements after simultaneously strengthening compressed and tensile zones.

Scientific Review Engineering and Environmental Sciences (2023), 32 (1), 69–86

Sci. Rev. Eng. Env. Sci. (2023), 32 (1) https://srees.sggw.edu.pl

ISSN 1732-9353 (suspended) eISSN 2543-7496 DOI 10.22630/srees.4506

Received: 11.10.2022
Accepted: 30.01.2023

Layth Abdul Rasool ALASADI✉ https://orcid.org/0000-0001-6244-7965
Tagreed Hameed KHLIF https://orcid.org/0000-0002-0429-796X
Fadhel Abdulabbas HASSAN https://orcid.org/0000-0003-1020-5133
University of Kufa, Faculty of Engineering, Department of Structures and Water Resources, Iraq

Experimental investigation for the local scour around V-shaped spur-dikes

Keywords: local scour, clearwater conditions, V-shaped spur-dyke, checkmark spur-dyke, river training structure, sediment transport

Introduction

Rivers are considered one of the greatest reasons for the existence of human being gathering. They convey and collect downfall as natural flows, and hence rivers are supposed to be the main source of water that must be mastered, restrained, and controlled to meet the requirements of human beings. In general, humans shape their existence alongside the rivers, where these situations have many advantages and disadvantages. One of the disadvantages is the destruction by river floodings and erosion of their banks, so rivers should be controlled in order to minimize their severity. Also, one should know any critical points of rivers and use biological or mechanical ways to reduce erosion, such as river training structures (Espandar & Imam, 1994; Rashad & Kassaf, 2020). The most common and beneficial transversal river training structures are spur-dikes (Al-Yassiry, 2015), i.e. artificial networks situated on river banks at various angles with one edge on the bank and the other edge outstanding into the current. Spur-dikes are constructed and created

✉laitha.alasadi@uokufa.edu.iq

Alasadi, L. A. R., Khlif, T. H., Hassan, F. A. (2023). Experimental investigation for the local scour around V-shaped spur-dikes. *Sci. Rev. Eng. Env. Sci.*, *32* (1), 69–86. DOI 10.22630/srees.4506

for many purposes, such as: directing the flow for the chosen reach, increasing the flow depth for navigation, preventing erosion of rivers banks, establishing river alignment and cross-section, enhancing habitats of riverine aquatic, altering the surrounding view and aiding the accessibility to the river (Jafari & Masjedi, 2015; Rashad, 2021). Spur-dikes are typically made from stone, gravel, rock, earth, sand, or piles. They can be either submerged or non-submerged. The non-submerged ones are made in the case of impermeable spur-dikes since their top is exposed to severe erosion if submerged. On the other hand, spur-dikes can be designed in different plan view shapes, such as I, L, T, hockey, inverted hockey, and curved shapes (Fig. 1).

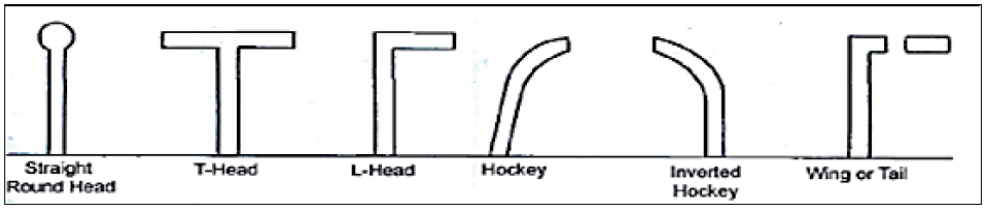

FIGURE 1. Different shapes of spur-dikes
Source: own work.

Against all spur-dike advantages and like any obstruction or hydraulic structure in an alluvial river, the natural river balance will be disturbed when a spur-dike crosses the water. So, as a result, a significant disruption in the flow pattern around the structure foundation will take place. This disruption leads to the scouring process initiation that ends with spur-dikes instability and time, which then leads to the failure in spur-dikes foundations. For hydraulic engineers, the local scour around spur-dykes is essential in the design process to ensure safety and economic purposes. Over the years, numerous researchers studied the most efficient factors affecting the scour process and the maximum exploration depth (Khsaf, 1991). His experimental study on a series of impermeable spur-dikes took place in the laboratory flume; it stated that the higher the scouring depth, the bigger the Froude number, degree of inclination angle and opening ratio. Kurzke, Weitbrecht and Jirka (2002) proved that spur-dike fields mainly generate two eddies; the larger one is in the spur-dike field center and the other in the upper corner of the spur-dike area. Kadota and Suzuki (2010) studied the effect of changing the shape of spur-dikes (L- and T-shapes) on the characters and trends of local scour around them. Through experiments, they proved that the T-shape spur-dikes had smaller local scour in the downstream area and, to some extent, from the spur-dike; a deposition takes place. Al-Yassiry (2015) tested non-traditional shapes of spur-dikes, which are the curved ones, and proved

that these shapes could minimize the local scour to some extent and gave better performance than the traditional shapes. Al Shaikhli and Kadhim (2018) studied the local scour around impermeable spur-dikes, submerged, single and straight in shape, fixed in a non-curved laboratory flume, and have various angle inclinations regarding flow direction. They proved that the horseshoe vortices are the leading cause of scour around spur-dike. The goals of the present study are to use the specific shape of spur-dikes that have the advantages of simple and low cost in construction, manageable scour at spur-dikes heads, large sediment deposits inside spur-dikes fields, and reasonable protection of the banks of rivers. This shape is the checkmark shape, also referred to as the V-shape. Also, this study presents two effective countermeasures for minimizing local scour around this kind of spur-dikes. These countermeasures are spur-dike numbers and the space between them.

Mechanisms of local scour

The scour is mainly defined as a naturalist event resulting from the flowing water's erosive behavior upon the banks and beds of alluvial channels. Scour is also defined as the sediment sweeping near or around structures placed inside the flowing water. So a reduction in the river bed level came from water erosions, which will have a tendency to reveal the structure foundations or carve and transport materials of the banks and bed of streams away from their original locations (Ezzeldin, Saafan, Rageh & Nejm, 2007). Such a phenomenon around any obstructions will progress continuously, leading to undermining and failure in the obstruction's foundations, collapsing all the hindrances and loss of life, nearby lands and properties. As regards the mechanism of the local scour, it should be stated that the existence of a spur-dike structure in the watercourse will cause contraction at the site and hence trigger vortices of the complicated system at the spur-dikes root, which is considered to be the main reason for scouring along with downflow at the spur-dike upstream face (Toro-Escobar, Voigt, Melville, Chiew & Parker, 1998; Fig. 2).

Figure 2 also displays how the horseshoe shaped vortex bumps the sand bed immediately ahead of the spur-dike and then holds up the corroded sediments, which will be transported in the direction of the flow by the main flow itself. There are four

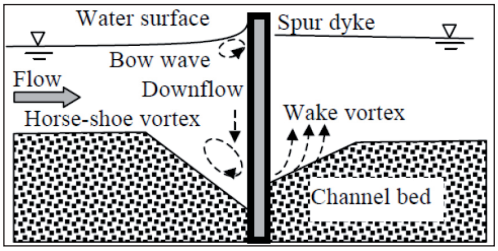

FIGURE 2. Local scour and flow through the section that passes the spur-dike head

Source: Toro-Escobar et al. (1998).

Alasadi, L. A. R., Khlif, T. H., Hassan, F. A. (2023). Experimental investigation for the local scour around V-shaped spur-dikes. *Sci. Rev. Eng. Env. Sci.*, *32* (1), 69–86. DOI 10.22630/srees.4506

serial stages of the scour hole development before reaching their final shape: initiation stage, development stage, stabilization stage, and equilibrium stage. It should be mentioned that the flow conditions control the shifting from one stage to another through time. In explicit water situations where the flow velocity is less than critical velocity, rapid development occurs for scouring until the dimensions of scour holes are no longer expanding and the maximum scouring depth is reached. In the case of live bed scour conditions where the flow velocity is more significant than the critical velocity and flow transports, in general, the bed and sides material. A quick reaching for the depth of scour holes oscillates with time due to the entrance and exit of the eroded sediments from the scour holes (Lagasse & Richardson, 2001; Fig. 3).

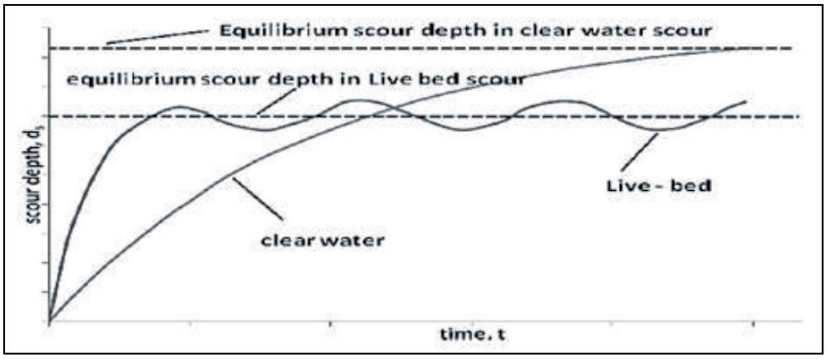

FIGURE 3. Clear-water and live-bed scour conditions
Source: Lagasse and Richardson (2001).

Various methods, like empirical formulas, physical models and theoretical approaches, are used to study and determine the scour depths around spur-dikes. In the present study, a group of physical models was used in a series of experiments. Then the results were used to shape an empirical formula to predict the maximum local scour under specific conditions.

Dimensional analysis

This technique is mathematical and employed in research studies to perform and design experiment models. Using this technique for a V-shaped spur-dike, the maximum depth of the local scour ($d_{s\max}$) at the clear water state located in this spur-dike nose can be inscribed as:

$$d_{s\max} = f\{y, v, v_c, L_g, \rho, \rho_s, g, n, b, d_{50}, \mu, \sigma_g, B, S_\circ\}, \quad (1)$$

where: y – depth of discharge [-], v – speed of the main flow [m·s^{-1}], v_c – critical velocity [m·s^{-1}], L_g – spur-dikes length [m], ρ – fluid density [kg·m^{-3}], ρ_s – bed sediments density [kg·m^{-3}], g – gravitational acceleration, g = 9.80665 [m·s^{-2}], n – number of spur-dikes, b – distance between spur-dikes [mm], d_{50} – median particle size [-], μ – fluid dynamic viscosity [Pa·s], σ_g – geometric standard deviation [-], B – laboratory flume width [m], $S_\circ$ – flume slope [m/m],

By using the Buckingham's π theorem; and after several arrangements and simplifications, Eq. (1) becomes:

$$d_{s\max}/y = f(v/v_c, F_r, n, b/y). \tag{2}$$

The assumptions and principles of transforming Eq. (1) simplified Eq. (2) are explained and described in more detail in the appendix.

The laboratory flume

Figure 4 shows the laboratory flume utilized in this study. It was made of steel stiffeners for the mainframe and glass fiber for the sides, with a total length of 6.6 m and an inner cross-section of 0.4 × 0.4 m. Two flume consists of two

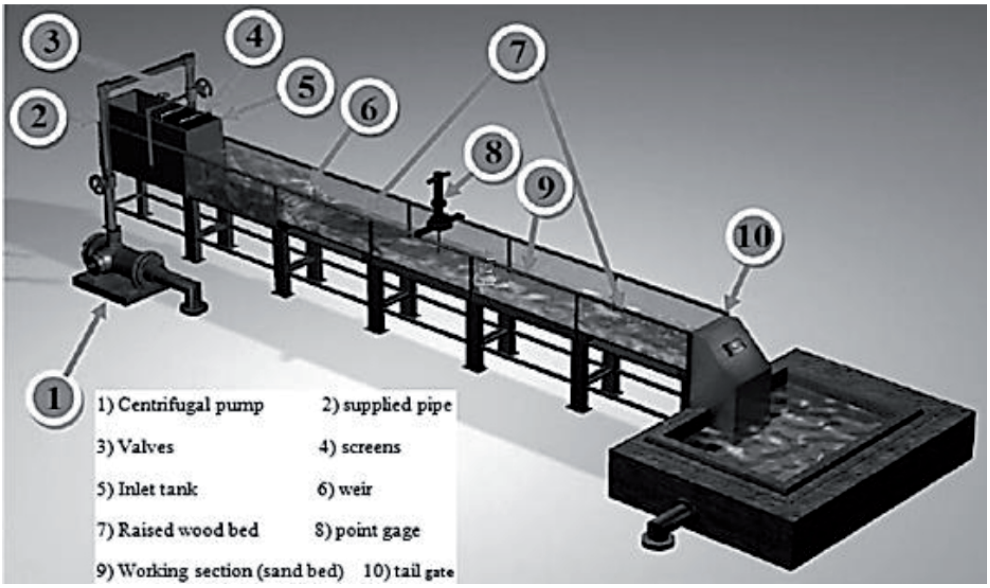

FIGURE 4. The laboratory flume
Source: own work.

Alasadi, L. A. R., Khlif, T. H., Hassan, F. A. (2023). Experimental investigation for the local scour around V-shaped spur-dikes. *Sci. Rev. Eng. Env. Sci.*, *32* (1), 69–86. DOI 10.22630/srees.4506

essential parts; an upstream inlet tank has a 1 m height and the second is a 5.6 m working section.

The middle part of the working section was covered with 0.1 m deep and 2 m long erodible sediments. The other two parts of the operating section were covered with wooden plates to match the level of the middle part. The inlet tank has three screens to prevent contamination with any undesirable debris. The flume had a closed system for supplying water from an underground basin using a centrifugal pump next to the flume. At the end of the flume, an adjustable tailgate was used to control the flow depth in the working section. A fabricated sharp-crested rectangular weir, 0.4 m wide and 0.25 m high, was placed at the upstream flume section to measure the entering discharge to the working section. The weir covered the full rectangular flume width and was made from Plexiglas® fiber. All scour depth measurements are done with a movable point gauge with ±1 mm accuracy transversely and longitudinally above the operating section.

The water discharges applied in this study were obtained by measuring the weir head over it; then, using the weir function – equation (King, Brater, Wei & Lindell, 1996):

$$Q = C_e \, L_e H^{\frac{3}{2}}, \tag{3}$$

where: Q – weir discharge [$m^3 \cdot s^{-1}$], C_e – effective discharge coefficient, $C_e = 1.78 + 0.24^{\frac{H}{P}}$ [-], H – head over weir crest measured before weir by 0.1 m [m], P – weir height from the bed [m], L_e – effective length, $L_e = L + K_L$, in which: L is a length of the weir, and K_L is a length factor, set to 0 [m], H_e – effective head over the weir, $H_e = H + K_H$, in which: K_H – head factor, set to 0.001 [-].

Spur-dike models

This study used a checkmark or V-shaped spur-dikes, 10-milimeter thick, 12-centimeter net high and 13-centimeter long, perpendicular to the flow direction where the length should be not less than 1/3 of the width of the flume (Möws & Koll, 2019; Fig. 5). The models were made of non-swelling polystyrene foam material. They have conducted

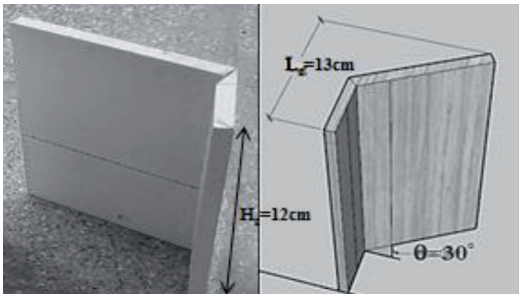

FIGURE 5. The V-shaped spur-dike model
Source: own work.

experiments under three different arrangements (triple, double and single). Also, the distance between them was altered three times ($1L_g$, $1.5L_g$, $2L_g$).

To achieve an adequately established flow, the models were positioned straight up through the sediment stratum in the working section center, where silicon adhesive was used to glue the spur-dikes very well to the inner side of the flume. Figure 6 illustrates a V-shaped spur-dike fixed in its place before beginning the experiments.

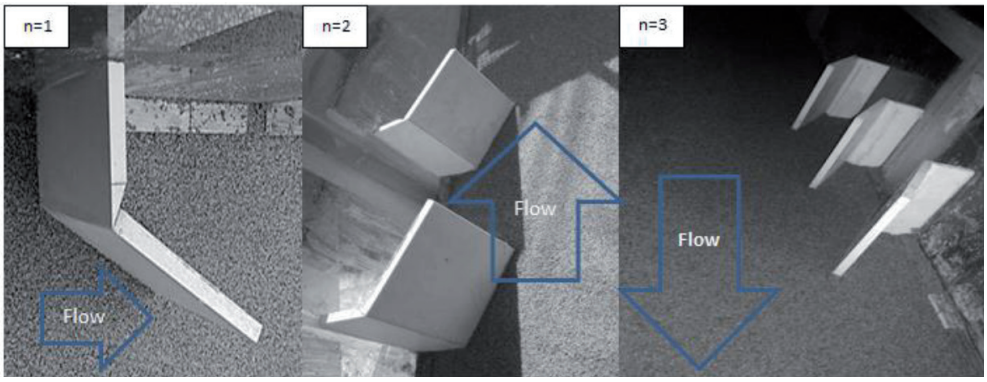

FIGURE 6. Three arrangements for the V-shaped spur-dikes placed in the flume
Source: own work.

Sediment of flume bed

The current work uses the cohesionless uniform sediment as the flume bed. The results of the mechanical sieve analysis should show that this sand had a median particle grains size d_{50} equivalent to 0.7 mm, and since it is not larger than 0.7 mm, there is no rippling formation. The sand size geometric standard deviation (σ_g) was equal to 1.31 to ensure the sediment uniformity that is essential to eliminate the armoring effect, which takes place if the sediment is non-uniform.

The experimental work conditions

The applied conditions for all experiments were clear water flowing in a subcritical steady state on a zero-flume bed. Several experiment sets (56 experiments) were performed, showing the impact of the essential parameters on the whole scouring process and the maximum depth of scour: flow depth (y), flow velocity (v), Froude number (Fr), spur-dikes number (n), and distance between spur-dikes (b).

Alasadi, L. A. R., Khlif, T. H., Hassan, F. A. (2023). Experimental investigation for the local scour around V-shaped spur-dikes. *Sci. Rev. Eng. Env. Sci.*, *32* (1), 69–86. DOI 10.22630/srees.4506

Performed study had some limitations: 400-milimeter width of the flume, 130-milimeter length of the spur-dike, three distances between the spur-dikes (130 mm, 195 mm, 260 mm), three types of tested spur-dikes (single, double, and triple), flow depth ranged from 16 to 46 mm, and lastly flow velocity ranged from 0.151 to 0.222 $m \cdot s^{-1}$.

Each laboratory experiment was performed under specific hydraulic parameters, which were the flow depth and velocity in the flume, as shown in Table 1.

TABLE 1. The studied experimental parameters

Run	Flow depth (y) [mm]	Flow velocity (v) [$m \cdot s^{-1}$]	Critical velocity (v_c) [$m \cdot s^{-1}$]	Distance between spur-dikes (b) [mm]	n	Run	Flow depth (y) [mm]	Flow velocity (v) [$m \cdot s^{-1}$]	Critical velocity (v_c) [$m \cdot s^{-1}$]	Distance between spur-dikes (b) [mm]	n
1	$2.1 \cdot 10^{1}$	$2.22 \cdot 10^{-1}$	$2.436 \cdot 10^{-1}$	–	S	29	$4.6 \cdot 10^{1}$	$1.8 \cdot 10^{-1}$	$2.81 \cdot 10^{-1}$	$1.3 \cdot 10^{2}$	D
2	$2.1 \cdot 10^{1}$	$1.981 \cdot 10^{-1}$	$2.436 \cdot 10^{-1}$	–	S	30	$3.6 \cdot 10^{1}$	$1.8 \cdot 10^{-1}$	$2.7 \cdot 10^{-1}$	$1.3 \cdot 10^{2}$	D
3	$2.1 \cdot 10^{1}$	$1.752 \cdot 10^{-1}$	$2.436 \cdot 10^{-1}$	–	S	31	$2.6 \cdot 10^{1}$	$1.8 \cdot 10^{-1}$	$2.54 \cdot 10^{-1}$	$1.3 \cdot 10^{2}$	D
4	$2.1 \cdot 10^{1}$	$1.514 \cdot 10^{-1}$	$2.436 \cdot 10^{-1}$	–	S	32	$1.6 \cdot 10^{1}$	$1.8 \cdot 10^{-1}$	$2.307 \cdot 10^{-1}$	$1.3 \cdot 10^{2}$	D
5	$4.6 \cdot 10^{1}$	$1.8 \cdot 10^{-1}$	$2.81 \cdot 10^{-1}$	–	S	33	$2.1 \cdot 10^{1}$	$2.22 \cdot 10^{-1}$	$2.436 \cdot 10^{-1}$	$2.6 \cdot 10^{2}$	T
6	$3.6 \cdot 10^{1}$	$1.8 \cdot 10^{-1}$	$2.7 \cdot 10^{-1}$	–	S	34	$2.1 \cdot 10^{1}$	$1.981 \cdot 10^{-1}$	$2.436 \cdot 10^{-1}$	$2.6 \cdot 10^{2}$	T
7	$2.6 \cdot 10^{1}$	$1.8 \cdot 10^{-1}$	$2.54 \cdot 10^{-1}$	–	S	35	$2.1 \cdot 10^{1}$	$1.752 \cdot 10^{-1}$	$2.436 \cdot 10^{-1}$	$2.6 \cdot 10^{2}$	T
8	$1.6 \cdot 10^{1}$	$1.8 \cdot 10^{-1}$	$2.307 \cdot 10^{-1}$	–	S	36	$2.1 \cdot 10^{1}$	$1.514 \cdot 10^{-1}$	$2.436 \cdot 10^{-1}$	$2.6 \cdot 10^{2}$	T
9	$2.1 \cdot 10^{1}$	$2.22 \cdot 10^{-1}$	$2.436 \cdot 10^{-1}$	$2.6 \cdot 10^{2}$	D	37	$4.6 \cdot 10^{1}$	$1.8 \cdot 10^{-1}$	$2.81 \cdot 10^{-1}$	$2.6 \cdot 10^{2}$	T
10	$2.1 \cdot 10^{1}$	$1.981 \cdot 10^{-1}$	$2.436 \cdot 10^{-1}$	$2.6 \cdot 10^{2}$	D	38	$3.6 \cdot 10^{1}$	$1.8 \cdot 10^{-1}$	$2.7 \cdot 10^{-1}$	$2.6 \cdot 10^{2}$	T
11	$2.1 \cdot 10^{1}$	$1.752 \cdot 10^{-1}$	$2.436 \cdot 10^{-1}$	$2.6 \cdot 10^{2}$	D	39	$2.6 \cdot 10^{1}$	$1.8 \cdot 10^{-1}$	$2.54 \cdot 10^{-1}$	$2.6\ 10^{2}$	T
12	$2.1 \cdot 10^{1}$	$1.514 \cdot 10^{-1}$	$2.436 \cdot 10^{-1}$	$2.6 \cdot 10^{2}$	D	40	$1.6 \cdot 10^{1}$	$1.8 \cdot 10^{-1}$	$2.307 \cdot 10^{-1}$	$2.6 \cdot 10^{2}$	T
13	$4.6 \cdot 10^{1}$	$1.8 \cdot 10^{-1}$	$2.81 \cdot 10^{-1}$	$2.6 \cdot 10^{2}$	D	41	$2.1 \cdot 10^{1}$	$2.22 \cdot 10^{-1}$	$2.436 \cdot 10^{-1}$	$1.95 \cdot 10^{2}$	T
14	$3.6 \cdot 10^{1}$	$1.8 \cdot 10^{-1}$	$2.7 \cdot 10^{-1}$	$2.6 \cdot 10^{2}$	D	42	$2.1 \cdot 10^{1}$	$1.981 \cdot 10^{-1}$	$2.436 \cdot 10^{-1}$	$1.95 \cdot 10^{2}$	T
15	$2.6 \cdot 10^{1}$	$1.8 \cdot 10^{-1}$	$2.54 \cdot 10^{-1}$	$2.6 \cdot 10^{2}$	D	43	$2.1 \cdot 10^{1}$	$1.752 \cdot 10^{-1}$	$2.436 \cdot 10^{-1}$	$1.95 \cdot 10^{2}$	T
16	$1.6 \cdot 10^{1}$	$1.8 \cdot 10^{-1}$	$2.307 \cdot 10^{-1}$	$2.6 \cdot 10^{2}$	D	44	$2.1 \cdot 10^{1}$	$1.514 \cdot 10^{-1}$	$2.436 \cdot 10^{-1}$	$1.95 \cdot 10^{2}$	T
17	$2.1 \cdot 10^{1}$	$2.22 \cdot 10^{-1}$	$2.436 \cdot 10^{-1}$	$1.95 \cdot 10^{2}$	D	45	$4.6 \cdot 10^{1}$	$1.8 \cdot 10^{-1}$	$2.81 \cdot 10^{-1}$	$1.95 \cdot 10^{2}$	T
18	$2.1 \cdot 10^{1}$	$1.981 \cdot 10^{-1}$	$2.436 \cdot 10^{-1}$	$1.95 \cdot 10^{2}$	D	46	$3.6 \cdot 10^{1}$	$1.8 \cdot 10^{-1}$	$2.7 \cdot 10^{-1}$	$1.95 \cdot 10^{2}$	T
19	$2.1 \cdot 10^{1}$	$1.752 \cdot 10^{-1}$	$2.436 \cdot 10^{-1}$	$1.95 \cdot 10^{2}$	D	47	$2.6 \cdot 10^{1}$	$1.8 \cdot 10^{-1}$	$2.54 \cdot 10^{-1}$	$1.95 \cdot 10^{2}$	T
20	$2.1 \cdot 10^{1}$	$1.514 \cdot 10^{-1}$	$2.436 \cdot 10^{-1}$	$1.95 \cdot 10^{2}$	D	48	$1.6 \cdot 10^{1}$	$1.8 \cdot 10^{-1}$	$2.307 \cdot 10^{-1}$	$1.95 \cdot 10^{2}$	T
21	$4.6 \cdot 10^{1}$	$1.8 \cdot 10^{-1}$	$2.81 \cdot 10^{-1}$	$1.95 \cdot 10^{2}$	D	49	$2.1 \cdot 10^{1}$	$2.22 \cdot 10^{-1}$	$2.436 \cdot 10^{-1}$	$1.3 \cdot 10^{2}$	T
22	$3.6 \cdot 10^{1}$	$1.8 \cdot 10^{-1}$	$2.7 \cdot 10^{-1}$	$1.95 \cdot 10^{2}$	D	50	$2.1 \cdot 10^{1}$	$1.981 \cdot 10^{-1}$	$2.436 \cdot 10^{-1}$	$1.3 \cdot 10^{2}$	T
23	$2.6 \cdot 10^{1}$	$1.8 \cdot 10^{-1}$	$2.54 \cdot 10^{-1}$	$1.95 \cdot 10^{2}$	D	51	$2.1 \cdot 10^{1}$	$1.752 \cdot 10^{-1}$	$2.436 \cdot 10^{-1}$	$1.3 \cdot 10^{2}$	T
24	$1.6 \cdot 10^{1}$	$1.8 \cdot 10^{-1}$	$2.307 \cdot 10^{-1}$	$1.95 \cdot 10^{2}$	D	52	$2.1 \cdot 10^{1}$	$1.514 \cdot 10^{-1}$	$2.436 \cdot 10^{-1}$	$1.3 \cdot 10^{2}$	T
25	$2.1 \cdot 10^{1}$	$2.22 \cdot 10^{-1}$	$2.436\ 10^{-1}$	$1.3 \cdot 10^{2}$	D	53	$4.6 \cdot 10^{1}$	$1.8 \cdot 10^{-1}$	$2.81 \cdot 10^{-1}$	$1.3 \cdot 10^{2}$	T
26	$2.1 \cdot 10^{1}$	$1.981 \cdot 10^{-1}$	$2.436\ 10^{-1}$	$1.3 \cdot 10^{2}$	D	54	$3.6 \cdot 10^{1}$	$1.8 \cdot 10^{-1}$	$2.7 \cdot 10^{-1}$	$1.3 \cdot 10^{2}$	T
27	$2.1 \cdot 10^{1}$	$1.752 \cdot 10^{-1}$	$2.436 \cdot 10^{-1}$	$1.3 \cdot 10^{2}$	D	55	$2.6 \cdot 10^{1}$	$1.8 \cdot 10^{-1}$	$2.54 \cdot 10^{-1}$	$1.3 \cdot 10^{2}$	T
28	$2.1 \cdot 10^{1}$	$1.514 \cdot 10^{-1}$	$2.436 \cdot 10^{-1}$	$1.3 \cdot 10^{2}$	D	56	$1.6 \cdot 10^{1}$	$1.8 \cdot 10^{-1}$	$2.307 \cdot 10^{-1}$	$1.3 \cdot 10^{2}$	T

S – single spur-dike; D – double spur-dike; T – triple spur-dike.

Source: own work.

It is important to know the time required to obtain the scour equilibrium conditions in all experiments to eliminate the time effect. Therefore, at the beginning, we made four experiments, each with a different flow velocity, where the scour was registered every 15 min by a point gauge to measure the maximum ± scour depth at the upstream nose of the spur-dike. To reach stable conditions, four experiments continued for 360 min until no more scour occurred in case of increasing time. From these four experiments it was observed that almost 95–97% of local scour took place through the first 3.5 h, and for more accuracy, all experiments were done within 4 h to exclude the time effect.

Analysis and discussion of results

Tests were designed to evaluate maximum values. The depth of scouring formed nearby spur-dikes is considered the primary step in designing their foundations. Different configurations are made with V-shaped spur-dikes to examine and study the scour phenomenon.

Flow depth (y). Using a different number of spur-dikes, Figure 7 shows the flow depth influence on scour depth (d_s) where it discerns that increasing flow depth (y)

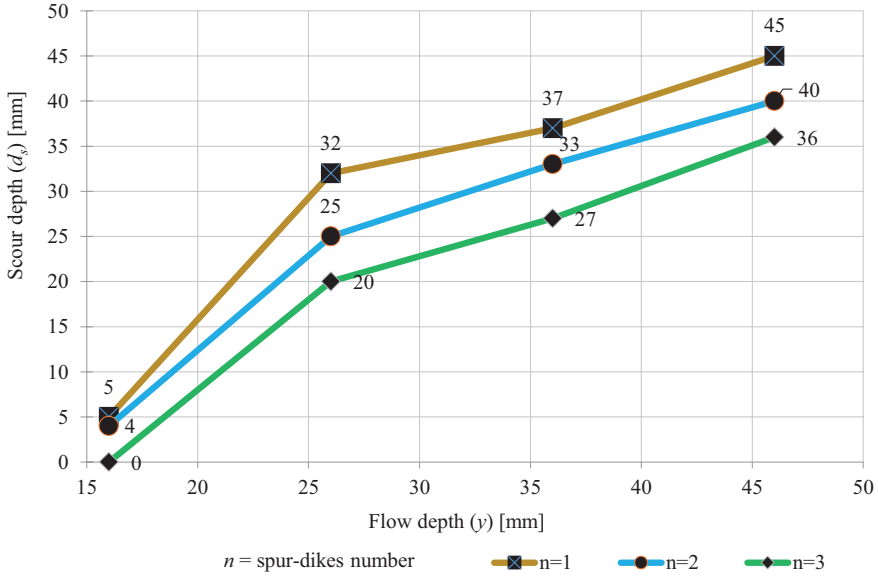

FIGURE 7. Effect of flow depth (y) on scour depth (d_s) development
Source: own work.

Alasadi, L. A. R., Khlif, T. H., Hassan, F. A. (2023). Experimental investigation for the local scour around V-shaped spur-dikes. *Sci. Rev. Eng. Env. Sci.*, *32* (1), 69–86. DOI 10.22630/srees.4506

will increase the propagation of scour, and hence maximum scour depth becomes much deeper, for example, in the case of a single spur-dike (n = 1); then increasing the water depth from 16 to 26 mm will increase the scour depth by almost 80%, increasing the water depth from 26 to 36 mm will increase the scour depth by almost 30%, and increasing the water depth from 36 to 46 mm will increase the scour depth by almost 23%. This scenario occurred while all other influencing parameters were kept constant.

Flow velocity (*V*). In the case of velocity values below the threshold value, the scour depth increases linearly alongside the flow velocity. At the same time, all the remaining parameters are kept steady, as illustrated in Figure 8.

Froude number (*Fr*). Figure 9 depicts the relation between *Fr* and a dimensionless fraction (d_s/y). The plotted figure shows that any increase in *Fr* will increase ds at stable values regarding the remaining factors.

Spur-dikes number (*n*). Figure 10 presents the significant influence of the number of spur-dikes in the decreasing scour process. The other influencing parameters were held constant; the scour depths were reduced when increasing the number of spur-dikes (in the limitation of this study) due to the interference and weakening of the strength of the overlapping horseshoe sort resulting from the sequential

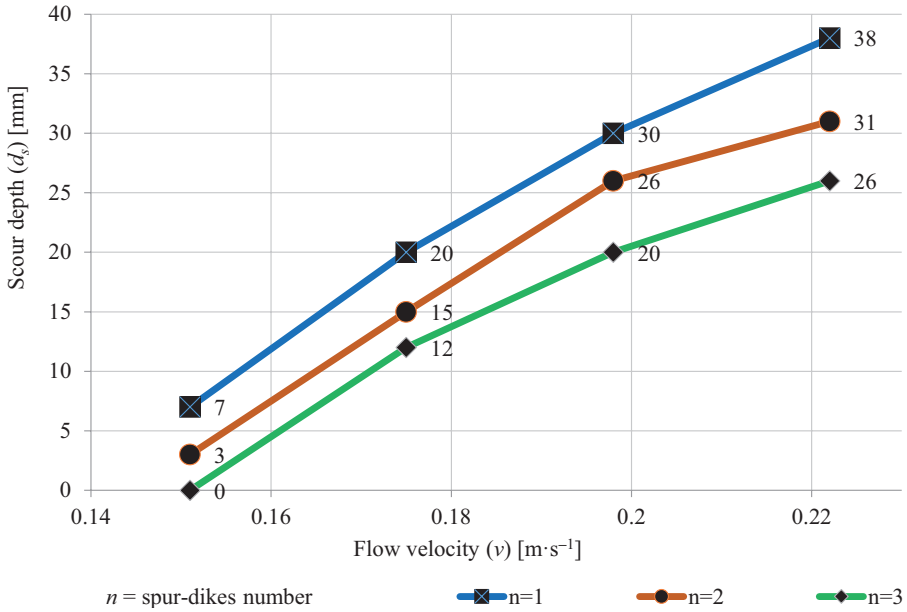

FIGURE 8. Effect of flow velocity (v) change on scour depth (d_s) development

Source: own work.

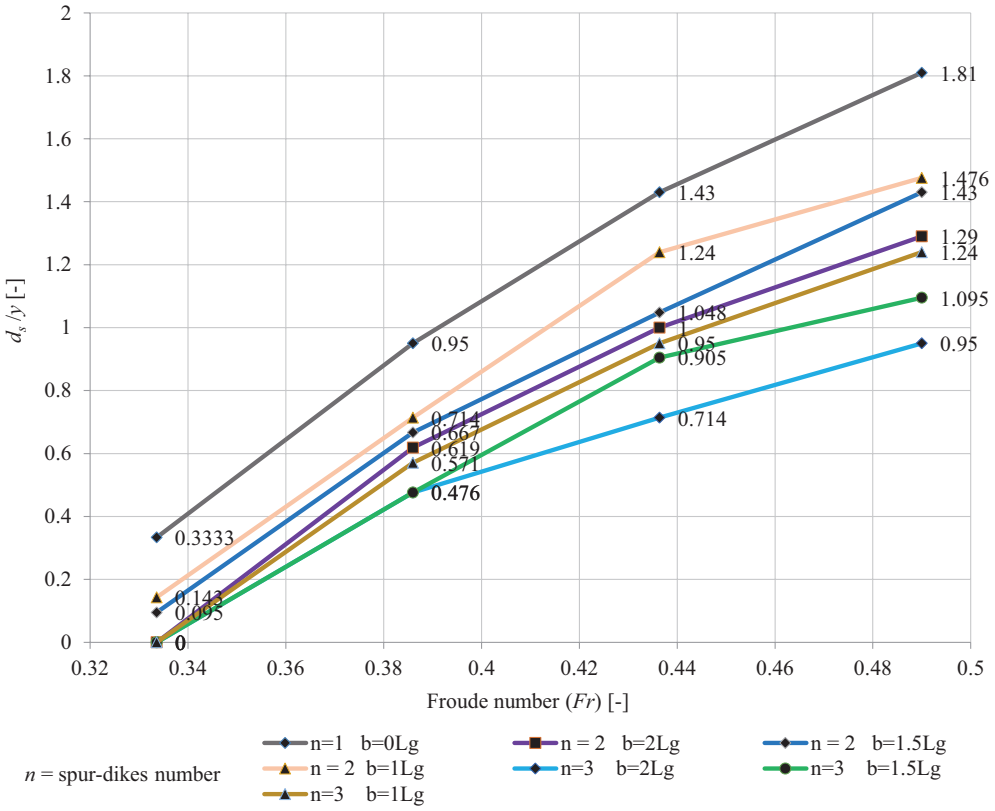

FIGURE 9. Effect of Froude number (Fr) change on dimensionless fraction (d_s/y) development
Source: own work.

spur-dikes. It was found that for maximum values of F_r; when an increasing number of spur-dikes changed from single to double; the decreasing percentage in scour depth was about 29%, whereas it was about 26% when the increasing spur-dikes number changed from double to triple.

Distance between spur-dikes (*b*). Three different distances between spur--dikes, and the triple and double spur-dike configurations were utilized to show the distance change effects on the scour depth. Figure 11 shows the estimation for the scour depth to decrease by a percentage ranged from 3.2 to 10% for each $0.5L_g$ increase in the distance between double spur-dikes, while the scour depth decreased by a percentage ranged from about 11.5 to 13% for each $0.5L_g$ increase in the distance between the triple spur-dikes in the limit of the study and in case of fixing all other studied parameters.

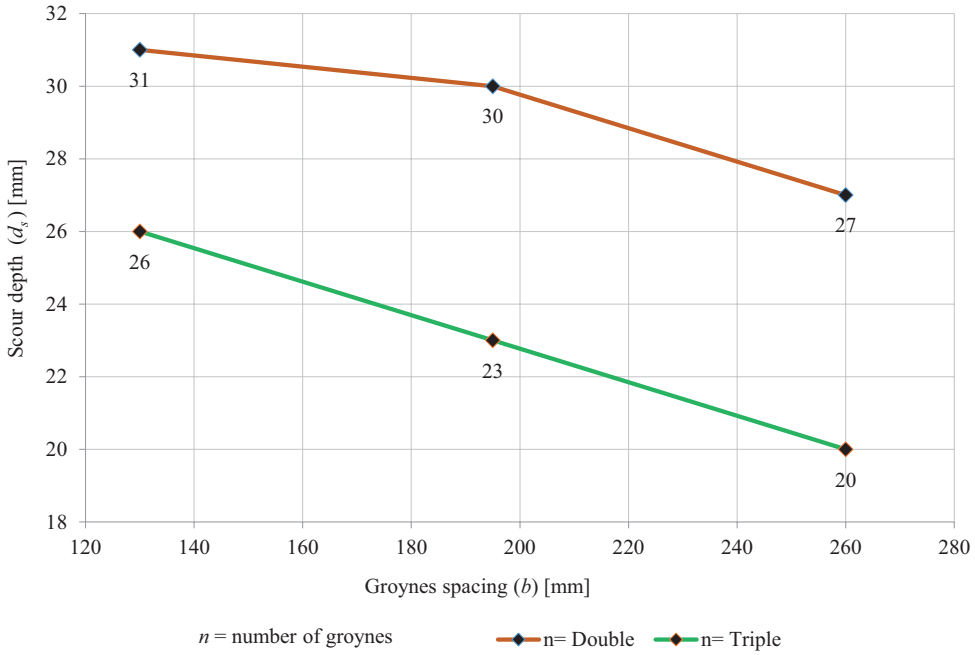

FIGURE 10. Effect of groynes spacing (b) on scour depth (d_s) development
Source: own work.

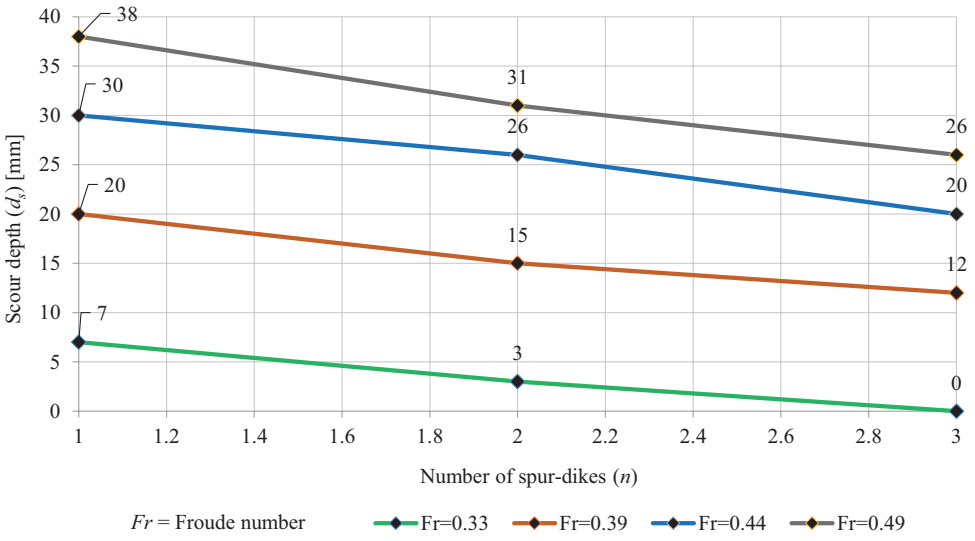

FIGURE 11. Effect of spur-dikes spacing on scour depth (d_s) development
Source: own work.

Comparison with the previous study. The results obtained from this study were compared with a previous study (Al-Yassiry, 2015) that had very similar conditions: the width of the flume in both studies was 40 cm, flow depth ranged from 20 to 21 mm for some studies, flow velocity ranged from 0.222 to 0.23 $m \cdot s^{-1}$ in both studies, with a similar spur-dikes length of 130 mm and similar spur-dikes number. The difference was the shape of spur-dikes to visualize its effect on the maximum scour depth. The results are summarized in Table 2.

TABLE 2. Tests results comparison

n	Distance between spur-dikes (*b*) [mm]	Previous study			Current study
		spur-dikes shape			
		straight	L-head	T-head	V-shape
1	–	58	66	68	38
2	260	55	57	62	27
3	260	55	55	59	20

Source: own work.

Table 2 shows that the V-shaped (checkmark) spur-dikes had the least max values. For the local scour, despite the similar conditions, in fact, the reduction percentage in maximum scour depth was 35–64%, 42–64%, and 44–66% for the straight, L-head, and T-head spur-dikes, respectively, when they compared with the checkmark spur-dikes.

A new formula developing

Utilizing the technique of a dimensional analysis, a dimensionless formula was presented to link the depths of scouring with the studied variables:

$$d_s/y = F(b/y, n, F_r, v/v_c). \tag{4}$$

Then, utilizing the IBM SPSS statistics, the experimental data were analyzed through non-linear regression to produce a formula for calculating the dimensionless fraction (d_s/y) as follows:

$$d_s/y = \left[C_1\left(b/y\right)\right] + \left[C_2\left(Fr^{C_3}\right)\right] + \left[C_4\left(v/v_c^{C_5}\right)\right] + \left(n^{C_6}\right) + C_7, \tag{5}$$

$C_1 = –0.015$, $C_2 = –55.591$, $C_3 = 3.936$, $C_4 = 7.807$, $C_5 = 2.592$, $C_6 = –0.317$, $C_7 = –2.122$.

Alasadi, L. A. R., Khlif, T. H., Hassan, F. A. (2023). Experimental investigation for the local scour around V-shaped spur-dikes. *Sci. Rev. Eng. Env. Sci.*, *32* (1), 69–86. DOI 10.22630/srees.4506

The determination coefficient for Eq. (5) was equal to 0.954. After arrangements and simplifications, the formula changes into:

$$d_s / y = \left[-0.015\left(b / y\right)\right] - \left[55.591\left(Fr^{3.936}\right)\right] + \left[7.807\left(v / v_c^{2.592}\right)\right] + n^{-0.317} - 2.122. \tag{6}$$

To examine Eq. (6) reliability, 20% of the original experimental records were entered into the formula itself, then a comparison between the observed and predicted values of $d_s/_y$ was made. The value of $R^2 = 0.974$ is obtained to reflect the excellent agreement to all records, as shown in Figure 12.

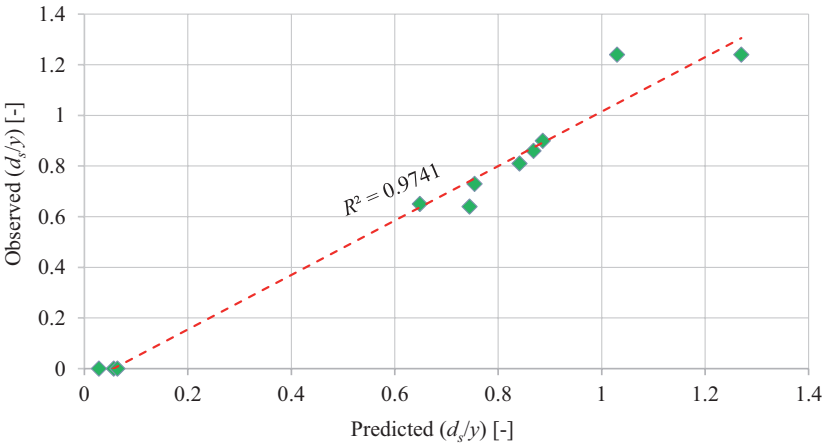

FIGURE 12. Observed and predicted values of dimensionless fraction (d_s/y) comparison
Source: own work.

Conclusions

The following conclusions were observed for the present study:

1. The scour depths changed directly with the Froude number (F_r), mean approach velocity of the flow (v) and flow depth (y). When the distance and number of spur-dikes are constant, the scour depths are increased by the hydraulic conditions. In the case of a single spur-dike ($n = 1$), increasing the water depth from 16 to 26 mm will increase the scour depth by almost 80%, increasing the water depth from 26 to 36 mm will increase the scour depth by almost 30%, and increasing the water depth from 36 to 46 mm will increase the scour depth by almost 23%.

2. In the limitation of this study and for constant flow depth and velocity, the scour depths decreased while increasing the spur-dike number and the distance between them. It was found that for maximum *Fr* values, there was an increasing number of spur-dikes from single to double; the decreasing percentage in scour depth was about 29%, whereas it was about 26% when increasing spur--dikes number from double to triple.
3. The scour depth was estimated to decrease by about 3.2 to 10% for each $0.5L_g$ increase in the distance between double spur-dikes, while the scour depth decreased by about 11.5 to 13% for each $0.5L_g$ increase in the distance between triple spur-dikes in the limit of the study and in case of fixing all the other studied parameters.
4. The deepest scour occurred in the spur-dike nose at the upstream face.
5. The first spur-dike always faces the maximum scour due to its location.
6. The best arrangement for double and triple spur-dikes was when they had a double spur length distance between them. Of course, when the number of spurs is three, it is better because it offers more protection for the river banks.

Data availability statement

Most datasets generated and analyzed in this study are comprised in this submitted manuscript. The other datasets are available on reasonable request from the corresponding author with the attached information.

References

Al Shaikhli, H. I. & Kadhim, K. N. (2018). Development an equations for flow over weirs using MNLR and CFD simulation approaches. *International Journal of Civil Engineering and Technology*, *9* (3), 70–79.

Al-Yassiry, H. H. (2015). *Investigation of local scour around curved groynes* (MSc thesis). Kufa: University of Kufa.

Espandar, R. & Imam, A. (1994). *Erosion control methods in rivers* (technical report). Tehran: Niroo Research Institute.

Ezzeldin, M. M., Saafan, T. A., Rageh, O. S. & Nejm, L. M. (2007). Local scour around spur dykes. In *Eleventh International Water Technology Conference, IWTC11* (pp. 779–795). Sharm El-Sheikh.

Jafari, B. & Masjedi, A. (2015). The effect of slot on scouring around spur dike at 180 degree bend. *Advances in Environmental Biology*, *9* (5), 215–220.

Kadota, A. & Suzuki, K. (2010). Local scour and development of sand wave around T-type and L-type groynes. In S. E. Burns, S. K. Bhatia, C. M. C. Avila & B. E. Hunt (Eds), *Scour and Erosion* (pp. 707–714). Reston: American Society of Civil Engineers.

Khsaf, S. I. (1991). *Experimental investigation of scour and deposition around spur-dikes* (MSc thesis). Baghdad: University of Baghdad.

King, H. W., Brater, E. F., Wei, C. Y. & Lindell, P. E. (1996). *Handbook of hydraulics*. New York: McGraw-Hill.

Kurzke, M., Weitbrecht, V. & Jirka, G. H. (2002). Laboratory concentration measurements for determination of mass exchange between groin fields and main stream. *River Flow*, *1*, 369–376.

Lagasse, P. F. & Richardson, E. V. (2001). ASCE compendium of stream stability and bridge scour papers. *Journal of Hydraulic Engineering*, *127* (7), 531–533.

Möws, R. & Koll, K. (2019). Roughness effect of submerged groyne fields with varying length, groyne distance, and groyne types. *Water*, *11* (6), 1253.

Rashad, B. M. (2021). *An experimental study of local scour around submerged groynes* (MSc thesis). University of Basrah, Basrah.

Rashad, B. M. & Kassaf, S. I. (2020). An investigation of the mechanism of local scour and deposition process around submerged (I-shape) groynes. *Journal of Critical Reviews*, *7* (13), 3204–3219.

Toro-Escobar, C., Voigt Jr, R., Melville, B., Chiew, M. & Parker, G. (1998). Riprap performance at bridge piers under mobile-bed conditions. *Transportation Research Record*, *1647* (1), 27–33.

Appendix

The dimensional analysis in the manuscript was the key to determining the important parameters that affect the maximum scour depth located in the nose of V-shaped spur-dike. The method will be described in detail further.

The maximum depth of scour ($d_{s\max}$) could be inscribed in functional form as (for explanation of the operands see the main text):

$$d_{s\max} = f\{y, v, v_c, L_g, \rho, \rho_s, \mathrm{g}, n, b, d_{50}, \mu, \sigma_g, B, S_\circ\}, \tag{1}$$

$$f_1\{d_{s\max}, y, v, v_c, L_g, \rho, \rho_s, \mathrm{g}, n, b, d_{50}, \mu, \sigma_g, B, S_\circ\} = 0. \tag{1a}$$

Since there are 15 variables ($n = 15$) that contain only three primary units ($m = 3$), 12 will be the number of the dimensionless parameters, which came from $n - \mathrm{m}$; thus:

$$f_2\left(\pi_1, \pi_2, \pi_3, \ldots, \pi_{12}\right) = 0. \tag{1b}$$

Each term has $m + 1 = 3 + 1 = 4$ variables if we assume the common variables v, ρ, and y; so, according to the π-theorem:

$\pi_1 = \rho^{a1}\, v^{b1}\, y^{c1}\, d_{S\max}$, $\pi_2 = \rho^{a2}\, v^{b2}\, y^{c2}\, v_c$, $\pi^3 = \rho^{a3}\, v^{b3}\, y^{c3}\, L_g$,

$\pi_4 = \rho^{a4}\, v^{b4}\, y^{c4}\, \rho_s$, $\pi_5 = \rho^{a5}\, v^{b5}\, y^{c5}\, \mathrm{g}$, $\pi_6 = \rho^{a6}\, v^{b6}\, y^{c6} n$,

$\pi_7 = \rho^{a7}\, v^{b7}\, y^{c7}\, b$, $\pi_8 = \rho^{a8}\, v^{b8}\, y^{c8}\, d_{50}$, $\pi^9 = \rho^{a9}\, v^{b9}\, y^{c9}\, \mu$,

$\pi_{10} = \rho^{a10}\, v^{b10}\, y^{c10}\, \sigma_g$, $\pi_{11} = \rho^{a11}\, v^{b11}\, y^{c11} B$, $\pi_{12} = \rho^{a12}\, v^{b12}\, y^{c12}\, S_\circ$.

Then we take each term and equate the exponents of M, L, and T.

$M^0 L^0 T^0 = (M\, L^{-3})^{a1}\, (LT^{-1})^{b1}\, (L)^{c1}\, L$,

M: $0 = a_1 \rightarrow a_1 = 0$,

L: $0 = 3a1 + b_1 + c_1 \rightarrow b_1 + c_1 = 0$,

T: $0 = -b_1 \rightarrow b_1 = 0$, $c_1 = -1$,

$\therefore\ \pi_1 = \rho^0\, v^0\, y^{-1}\, d_{S\max} \Rightarrow\ \pi_1 = \dfrac{d_{S\max}}{y}$.

In the same way, the other π-terms can be written as:

$$\pi_2 = \frac{v}{v_c}, \pi_3 = \frac{L_g}{y}, \pi_4 = \frac{\rho_s}{\rho}, \pi_5 = Fr, \pi_6 = n, \pi_7 = \frac{b}{y}, \pi_8 = \frac{d_{50}}{y}, \pi_9 = \frac{\mu}{\rho v y}, \pi_{10} = \sigma_g, \pi_{11} = \frac{B}{y}, \pi_1$$

$$\therefore 0 = f_3\left(\frac{d_{S\max}}{y}, \frac{v}{v_c}, \frac{L_g}{y}, \frac{\rho_s}{\rho}, Fr, n, \frac{b}{y}, \frac{d_{50}}{y}, \frac{\mu}{\rho v y}, \sigma_g, \frac{B}{y}, S_\circ\right).$$

Now, the above relationship was made simpler by eliminating constant values terms, also enforcing the assumptions (constant viscosity and relative density, single sediment size), then the functional relation is:

$$f_4\left(\pi_1, \pi_2, \pi_4, \pi_5, \pi_6, \pi_7\right) = 0 \ \text{ or } \ f_4\left(\frac{d_{S\max}}{y}, \frac{v}{v_c}, Fr, n, \frac{b}{y}\right) = 0.$$

In terms of the maximum scour depth:

$$\frac{d_{S\max}}{y} = f_5\left(\frac{v}{v_c}, \frac{L_g}{y}, Fr, n, \frac{b}{y}\right). \tag{2}$$

Alasadi, L. A. R., Khlif, T. H., Hassan, F. A. (2023). Experimental investigation for the local scour around V-shaped spur-dikes. *Sci. Rev. Eng. Env. Sci.*, *32* (1), 69–86. DOI 10.22630/srees.4506

Summary

Experimental investigation for the local scour around V-shaped spur-dikes. Spur-dikes are efficient hydraulic structures that are made for numerous purposes. They have one end on the stream bank and another extending into the current. As a result of the existing spur-dikes in the stream course, the local scour phenomena usually occur around them, leading to several predicaments which have been of great concern to the hydraulic engineers. For the present work, laboratory experiments were carried out to measure the scour depths around several spur-dikes located at different distances for the V-shaped one. The experiments were conducted using physical models installed in a non-curved flume with a bed with uniform cohesion-less sediment of a medium particle size (d_{50} = 0.7 mm). All the models were operated under the subcritical flow of clear-water conditions. The investigations include three spur-dikes (1, 2 and 3) and three distances between them (1, 1.5 and 2 of spur-dike length) as two countermeasures to minimize the local scour depths. The results showed that an increasing number of spur-dikes and the distances between them would decrease the scour depths within the limit of the present study. The experimental data were used to create a new formula of R^2 = 0.954 that reflects a good agreement with the experimentally observed results.

Scientific Review Engineering and Environmental Sciences (2023), 32 (1), 87–98

Sci. Rev. Eng. Env. Sci. (2023), 32 (1) https://srees.sggw.edu.pl

ISSN 1732-9353 (suspended) eISSN 2543-7496 DOI 10.22630/srees.3899

Received: 24.08.2022
Accepted: 05.01.2023

Shahrul Nizam MOHAMMAD[1]✉

Mohamed Khatif Tawaf MOHAMED YUSOF[1]

Muhammad Bazli Faliq MOHD PUAAD[1]

Rozana ZAKARIA[2]

Amin BAKI[3]

[1]MARA Technological University (UiTM), College of Engineering, School of Civil Engineering, Malaysia
[2]University of Technology Malaysia (UTM), Faculty of Engineering, School of Civil Engineering, Malaysia
[3]Envirab Services, Malaysia

Exploring acceptance on benefit of solar farm implementation in Malaysia

Keywords: solar energy, renewable electricity, electricity generation, global warming, climate change, solar photovoltaic

Introduction

Energy is an essential source that is needed for the development and civilization of every country. Energy is used daily to meet human needs for lighting, heating, cooling and transportation. In addition it is also used as input for industrial production (Jeyhun, Shahriyar, Hasan, Serhat & Ridvan, 2020). Despite their contribution to the development of human civilization, fossil fuels are a major contributor to environmental problems, including air pollution, global warming and climate change (Payam & Taheri, 2018). Majority of countries rely on burning fossil fuels to generate

✉shahrul9688@uitm.edu.my

their energy and cause issues such as: supply shortages, supply risk and pricing volatility (Martins, Felgueiras, Smitkova & Caetano, 2019). The adverse effects of climate change are made worse by an over-reliance on fossil fuels, which also raises the pollution levels that permanently harm the atmosphere (Saudi, 2019).

The amount of power produced worldwide has been steadily increasing since 1974. Globally, the average annual growth rate of power output between 2010 and 2018 was 2.5%. 66.3% of the world's gross power production in 2018 came from the production of electricity from combustible fuels such as coal, oil, natural gas, biofuels made of solid biomass and animal products, gas and liquids from biomass, industrial waste, and municipal garbage (U.S. Energy Information Administration [IEA], 2020). The construction sector uses between 20% and 50% of the total energy used globally across many locations. This percentage is higher in highly populated cities, such as Hong Kong, which is more than 60% (Ma & Yu, 2020). As stated by Saidur, Hasanuzzaman, Yogeswaran, Mohammed and Hossain (2010), the construction sector accounts for 36% of CO_2 emissions and 40% of energy consumption in Europe.

Based on research conducted by Ali, Hasanuzzaman, Rahim, Mamun and Obaidellah (2020), due to global temperature that continues to rise, energy consumption in the construction sector increases, especially in terms of air-conditioning. According to earlier studies, the construction industry consumes a significant amount of electricity worldwide, accounting for 40–45% of total electricity consumption in Brazil, the United States of America (USA) and the United Kingdom (Alves, Machado, de Souza & Wilde, 2018). Meanwhile in Asia, it has been recorded that the residential sector came to be the second largest consumer of electricity after the industry and the amount of electricity consumed by the residential sector multiplied from 1971 to 2016 (IEA, 2018). In Southeast Asia, energy consumption is expected to double by 2040, the rise of electricity demand has been among the fastest in the world, increasing by an average of 6% annually. The fastest growing in space cooling usage is one of the contributors to this situation, which is driven by growing incomes and high cooling needs (IEA, 2019).

Many nations continue to generate more power using the traditional power production method of burning fossil fuels. This traditional method releases greenhouse gases and causes air pollution that harms the environment in order to fulfil the growing demand for energy (Hasanuzzaman, Zubir, Ilham & Che, 2016). Burning fossil fuels resulted in the release of dangerous gases, such carbon monoxide, carbon dioxide, nitrogen oxides and sulfur dioxide. A greenhouse gas called carbon dioxide contributes to global warming. Sulfur dioxide can generate acid rain, which harms the aquatic life and plants while also causing respiratory and cardiovascular problems that are more severe in people (EIA, 2022). Various climate change frameworks

have been examined globally over the past few decades aimed at reducing carbon dioxide emissions in order to meet the environmental goals and the socioeconomic needs of the global community (Umar, Ji, Kirikkaleli & Alola, 2021).

People around the world are developing and promoting clean and low carbon energy to respond to the crucial environment issues due to burning fossil fuels to produce energy. Instead, rising prices and limited reserves of fossil energy also worry the industries' players. Therefore, many countries invest in the research and development of renewable energy sources, such as wind energy and solar energy to overcome environmental pollution and the limitation of fossil fuel reserves that lead to the increase in the price of the resources (Payam & Taheri, 2018; Song, Ji, Du & Geng, 2019). Renewable energy is recognized as a very practical means of halting the deterioration of the environment and achieving sustainable development (Kobayashi et al., 2013). Southeast Asia has enormous potential for renewable energy, especially solar energy due to its location to the equator and year-round exposure to solar radiation. However, only about 15% of the region's overall energy needs are now met by renewable energy production. The contribution of solar photovoltaic and wind energy is still minimal despite lowering the costs of the renewable energy technology, while several markets are increasingly putting frameworks in place to better facilitate the deployment of renewable energy (IEA, 2020).

It has been discovered that PV technology is technologically reliable, geographically distributed and has a significant potential for providing sustainable energy sources for producing electricity. Photovoltaic system technology has advanced to become practical, effective and increasingly affordable (Mohammad et al., 2013). Malaysia is perfectly suited to produce solar photovoltaic energy due to its equatorial location, year-round sunshine exposure and high irradiation level. Sunlight is a limitless source of clean energy that can be used to create power. The little moving parts and long lifespan of the technical solar energy equipment, on the other hand, result in the extremely cheap operational expenses for solar panels.

In Malaysia, initiatives to enhance the share of solar and other renewable energy sources in the country's energy mix were established under the National Renewable Energy Policy Action Plan (Sustainable Energy Development Authority Malaysia [SEDA], 2009). This initiative was strengthened in 2015 as part of the Paris Climate Change Conference (COP21) of the United Nations, where the nation committed to reducing its greenhouse gas emissions by up to 40% from their 2005 levels by 2020. The Eleventh Malaysia Plan (2016–2020) set a national goal to achieve an installed capacity of 2,080 MW produced by green energy sources by 2020, up from 243.4 MW in 2014 (Economic Planning Unit, 2015). Solar PV installations produced around 1%, or 227.5 MW, of Malaysia's

total installed electrical capacity in 2016, with the remaining 1% coming from all other green energy sources. Future national goals include the intensification of the development and utilization of renewable energy resources, which include solar PV to meet the target of 31% of the total installed capacity by 2025 (Economic Planning Unit, 2021).

The higher education institution reflects a small town that consists of many buildings, including offices, dwellings, a small hospital, recreation facilities, etc. that characterize a bigger community. College and university campuses consume a huge amount of electricity on a daily basis to run buildings and facilities used by the staff, students and visitors. The higher education institution is a role model to an external community and its activities impact the society, environment and economy. As a result, the large energy demands of these higher education institutions as well as the growing concerns regarding conventional fossil fuel toxic wastes, numerous institutions are struggling to aggressively apply renewable energy projects, such as the PV system in their campuses. Constructing a commercial scale PV system on campus can be a golden opportunity for higher education institutions to highlight their determination toward sustainability. In some interpretations, a PV system on campus gives an impression of forward thinking and being a green institution for the staff, students and visitors (Jo, Ilves, Barth & Leszczynski, 2017). Therefore, the objectives of this study are to determine the financial opportunities of the solar farm implementation as well as to analyze the benefit of the solar farm implementation towards the society and environment.

Material and methods

Data were collected through a questionnaire survey given to the respondents whose job scope directly involved the solar energy. This survey only involved people that have knowledge and experience in solar energy to ensure the accuracy and reliability of the collected data. 34 respondents that took parts in the survey. Most of the respondents in this study were people who work in the government sector, higher education institution, consultant company and contractor company where they were directly involved in solar energy as illustrated in Figure 1.

In this questionnaire survey, majority of the respondents involved were degree holders, who constituted 76% of all respondents. On the other hand, there were three respondents with a master's degree that responded to this survey. In addition, 11% of respondents held a diploma. Respondents who held a certificate were the minority, constituting only 3% of all respondents. Figure 2 illustrates the composition of the

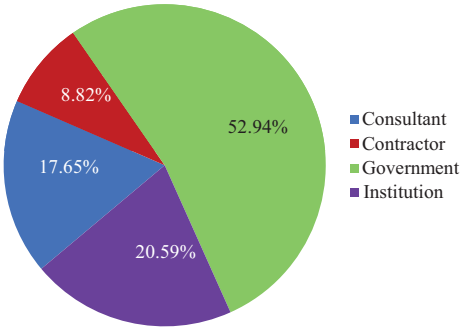

FIGURE 1. Fraction of the respondents based on type of company

Source: own studies.

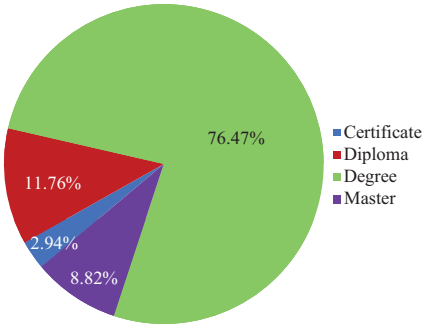

FIGURE 2. Fraction of respondents based on education level

Source: own studies.

respondents based on their education. Based on the education level of the respondents, it was expected that they had sufficient knowledge to give an opinion in this questionnaire survey.

All collected data and information were analyzed by using the average index (*AI*) value to determine the level of agreement of respondents through their feedback answers. The frequency analysis was used in analyzing the frequencies and *AI* value of the respondents relating to the variables in the questionnaires. In order to analyze the data, the average index analysis was used to determine the level of significance of the data. Table 1 shows the average index and level of significance. The average index was calculated based on the equation, as follows:

TABLE 1. Average index and level of importance

Average index (*AI*)	Level of importance or evaluation
$1.00 \leq AI < 1.50$	not important/strongly disagree
$1.50 \leq AI < 2.50$	less important/disagree
$2.50 \leq AI < 3.50$	neutral
$3.50 \leq AI < 4.50$	important/agree
$4.50 \leq AI \leq 5.00$	very important/strongly agree

Source: own studies.

$$average\ index = \frac{\sum \alpha_i x_i}{\sum x}, \tag{1}$$

where: a_i – constant expressing the weight given to i, x_i – frequency of response for i = 1, 2, 3, 4, 5 and illustrated as follows: x_1 – frequency of the response 'strongly disagree' and corresponding to 1; x_2 – frequency of the response 'disagree' and corresponding to 2; x_3 – frequency of the response 'average' and corresponding to 3; x_4 –frequency of the response 'agree' and corresponding to 4; x_5 – frequency of the response 'strongly agree' and corresponding to 5.

Mohammad, Sh. N., Mohamed Yusof, M. K. T., Mohd Puaad, M. B. F., Zakaria, R., Baki, A. (2023). Exploring acceptance on benefit of solar farm implementation in Malaysia. *Sci. Rev. Eng. Env. Sci.*, *32* (1), 87–98. DOI 10.22630/srees.3899

Results and discussion

Financial opportunities of solar farm implementation

The benefits of the solar farm implementation in Malaysia are determined through the respondents' perception who were involved in the solar energy industry. The analysis of benefits of the solar farm implementation is presented in a descriptive analysis form as shown in Figure 3. In this research, the agreement level is determined based on the mean score acquired from the respondents' responses. The element is only considered significant when the mean score of the element equals 3.4 or more.

Figure 3 shows the analyzed data from the survey. It was found that long-term financial savings identified the financial opportunities the most because solar energy is free and it is available all year long in Malaysia. What is more, solar farms have less rotating equipment compared to a conventional fossil fuel generator, hence the maintenance cost is lower over the long-term operation. The free and non-depleting energy source was the second most identified financial opportunity. The price of fossil fuels shows the incremental trend over the years due to the growing demand and depletion of resources. It is different for solar farms, it will only need solar energy to generate electricity and there will be no issue regarding the price as it is a free and non-depleting source of energy.

Solar farm implementation will encourage the establishment of more businesses related to solar energy in the country. Solar farms are a new method of generating electricity in Malaysia compared to the fossil fuel electric generator. Therefore, it will create a new demand of business in the solar energy technology and attract foreign direct investment into the country to meet the country's aspiration to implement the solar farms in generating clean electricity. The solar technology company will flourish to meet the country's demand regarding the implementation of solar farms. Based on the conducted survey, the low risk investment and fast installation process obtained the lowest average index value of under 3.5. It is because solar farm technology is still new in Malaysia and there will be a lot of uncertainties associated with the high risk of investment. Many investors are still afraid to make investments and still carefully observe the operation of solar farms in generating electricity in order to get the investment return back. It is believed that once the business and technology of solar farm are mature in Malaysia, the risk will gradually decrease and it will attract many investors who will get involved in solar farms to generate electricity. Over time, expertise and technology in constructing solar farms will keep improving and the installation of solar farms can be accelerated in the future.

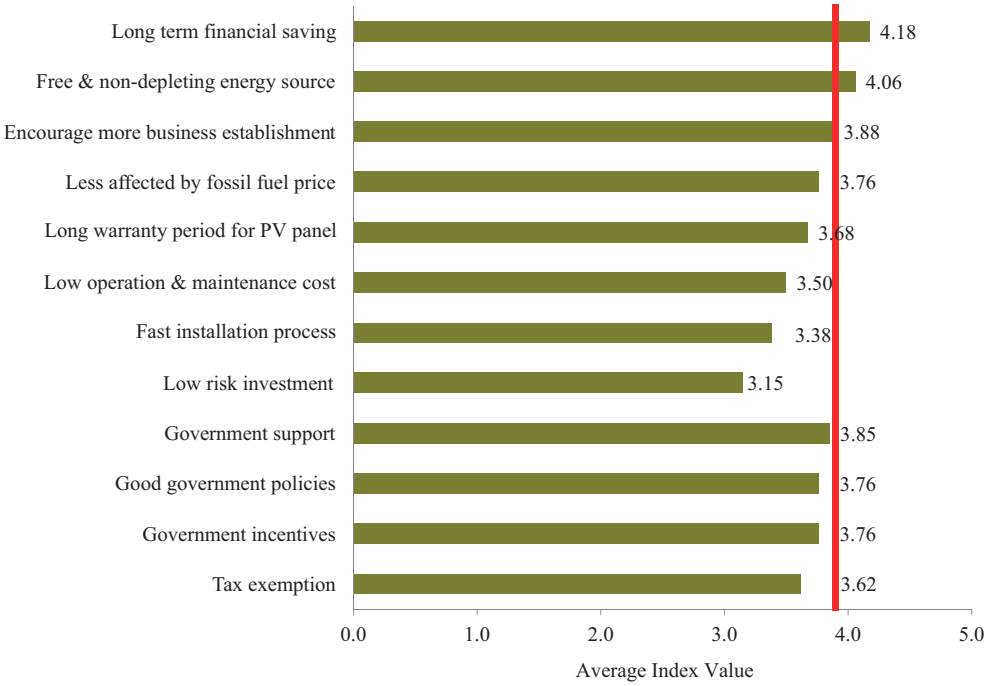

FIGURE 3. Mean score of financial opportunities of solar farm implementation
Source: own studies.

Benefit of solar farm implementation toward society

The survey included five elements being asked for the benefit of the solar farm implementation towards the society. The elements were as follows: less noise during operation, safe operation environment, being a role model to others, creation of job opportunities, and improving the level of health. Based on the analysis of the collected data, the top three elements were: less noise during operation with the highest average index value of 4.24, followed by safe operation environment with the score of 4.15, and then by being a role model to others with a score of 4.15.

Figure 4 shows the benefits of the solar farm implementation towards the social aspect for the society. Conventional fossil fuel power plant produces a high level of noise due to high speed of rotating equipment, such as turbine in generating electricity, which will disrupt the nearby community. However, electricity is generated directly from the solar energy conversion in solar farms by the means of a photovoltaic panel and there will be less rotating equipment that can produce noise, hence no noise issues in the surrounding area. Solar farms also create safe operation environ-

Mohammad, Sh. N., Mohamed Yusof, M. K. T., Mohd Puaad, M. B. F., Zakaria, R., Baki, A. (2023). Exploring acceptance on benefit of solar farm implementation in Malaysia. *Sci. Rev. Eng. Env. Sci.*, *32* (1), 87–98. DOI 10.22630/srees.3899

FIGURE 4. Benefit of solar farm implementation toward social
Source: own studies.

ment where workers are exposed only to limited risks because they will not have to deal with high temperature and high-pressure operations that usually take place in conventional fossil fuel power plants.

Other than that, the implementation of solar farms can also be a role model to others so that more parties will have the confidence to get involved in solar farms as a method to generate electricity. When many parties participate in the solar farm investment to generate electricity, solar energy will become more common to the public and will get accepted in the society. At the same time, locals will draw the benefits through the creation of new jobs that will improve the economy standard of the local community. Furthermore, solar farms will boost the establishment of other supply chain business, where each one will require human capital to support the growth of the solar farm industry. Lastly, solar farms can improve the level of health of the public due to zero carbon emissions because solar farms do not burn any fuel during the operation of generating electricity. In order to generate electricity, solar energy is directly converted into electric power and it does not produce pollution during the operation, hence the health level of people around the solar farm will not be affected.

Benefit of solar farm implementation toward environment

In the survey that was conducted on the benefit of solar farms towards the environment, there were six elements that required feedback from the respondents. The elements were as follows: reduced greenhouse gas (GHG) emissions, being environmentally friendly, clean energy, conservation of natural resources, utilization of brownfield sites, and no massive deforestation. Figure 5 depicts the mean score of benefits of solar farm implementation to the environment. The figure shows that

FIGURE 5. Mean score of environmental benefits of solar farm implementation
Source: own studies.

generally solar farms are more environmentally friendly compared to conventional fossil fuel power plants in generating electricity to fulfil human needs for energy. There are lots of benefits of solar farm implementation to the environment. Reduced GHG emissions are the element that scores the highest with the mean score of 4.53 based on the responses of the respondents.

Firstly, the implementation of solar farms can reduce greenhouse gas (GHG) emissions to the environment because it will not burn any fuels that can produce GHGs, such as carbon monoxide. Secondly, the solar farm implementation is environmentally friendly as it will not pollute water, air and soil of the solar farm site. It has been proven that a PV panel that is used in a solar farm directly changes the solar energy into the electric energy without emitting any emissions during the process. Next, the implementation of solar farms will lead to the generation of clean energy whereby the carbon footprint of the generation of electricity through solar farms is low compared to fossil fuel power plants. Moreover, the use of solar farms to generate electricity can conserve natural resources such as coal, diesel and natural gas, so that it can reduce the dependency on fossil fuels in generating electricity. Furthermore, solar farms can be implemented to utilize brownfield sites where other constructions cannot take place, such as abandoned landfills and factories. Therefore, all brownfield sites in Malaysia can be fully utilized to produce clean energy in order to protect our environment.

However, respondents' feedback on no massive deforestation is not significant with the score of only 3.0, which is less than 3.5. It is because in order to implement solar farms a huge area of land will be required. If the solar farm is to be implemented in the rural area, then deforestation needs to be done to clear the site, so that the solar farm can be constructed. Hence, when it comes to deforestation,

it still needs to be done to construct the solar farm just like any other conventional fossil fuel power plant. Besides other benefits that can be offered by solar farms in generating electricity, the forest will be affected by the construction of solar farm. Therefore, the selection of the site for the construction of the solar farm plays an important role to the environmental protection. The authorities that are involved in decision-making regarding the site selection must consider all factors to balance the benefit of the solar farm and the side impact to the forest.

Conclusions

Solar PV was been introduced decades ago as a solution for clean energy and environment issues. In developing solar farms, huge amount of money is needed for the initial capital cost. Therefore, finances constitute the main criteria that needs to be taken into consideration in a high investment decision. Based on the conducted research, there are numerous financial benefits of solar farm implementation in Malaysia. For example, the investment in solar farms provides long term financial saving as a result of lesser dependency on fossil fuels. Furthermore, solar energy is a free energy source from the sun, and it will allow more businesses related to solar energy to be established in the country in order to meet the demands. Proper implementation of solar farms can enhance the country's role in the PV technology and simultaneously open the opportunities for local talents to be involved in the solar panel technology.

Furthermore, the solar farm implementation gives benefits in the social aspect. For instance, there will be less noise from solar farms because there will be very little rotating equipment in the power plants, thus the solar farm can be installed near the community. The solar farm also offers a safe operation environment to the personnel as explosions will be less likely because the plant generates electricity without burning any fossil fuels. Eventually, there will be no smoke and carbon emissions during the operation of the solar farm in generating electricity because PV panels directly convert solar energy into electric energy and this clean power plant will bring benefits to the human health.

In addition, benefits in environmental conservation are a strong advantage of solar farm implementation. For example, implementation of solar farms in generating electricity helps to reduce GHG emissions and conserve natural sources. Nowadays, environment issue is of a global concern because our world is facing global warming and natural disasters that affect human life. Thus, people believe that solar farm system is a solution to tackle environmental issues and at the same time provide reliable energy for daily activities. By implementing solar farm system in generating energy, Malaysia contributes to protecting the environment by reducing pollution in power plants.

Acknowledgements

This work was technically supported by Universiti Teknology Mara (UiTM) Cawangan Johor Kampus Pasir Gudang.

References

Ali, S. B. M., Hasanuzzaman, M., Rahim, N. A., Mamun, M. A. A. & Obaidellah, U. H. (2021). Analysis of energy consumption and potential energy savings of an institutional building in Malaysia. *Alexandria Engineering Journal*, *60* (1), 805–820.

Alves, T., Machado, L., Souza, R. de & Wilde, P. (2018). Assessing the energy saving potential of an existing high-rise office building stock. *Energy and Buildings*, *173*, 547–561.

Economic Planning Unit, Prime Minister's Department (2015). *Eleventh Malaysia Plan, 2016––2020.* Kuala Lumpur: Economic Planning Unit, Prime Minister's Department.

Economic Planning Unit, Prime Minister's Department (2021). *Twelfth Malaysia Plan, 2021––2025.* Kuala Lumpur: Economic Planning Unit, Prime Minister's Department.

Hasanuzzaman, M., Zubir, U., Ilham, N. & Che, H. (2016). Global electricity demand, generation, grid system, and renewable energy polices: a review. *Wiley Interdisciplinary Reviews: Energy and Environment*, *6* (3), 222.

Jeyhun, I. M., Shahriyar, M., Hasan, D., Serhat, Y. & Ridvan, A. (2020). Elasticity analysis of fossil energy sources for sustainable economies: A case of gasoline consumption in Turkey. *Energies*, *13* (3), 731.

Jo, J., Ilves, K., Barth, T. & Leszczynski, E. (2017). Implementation of a large-scale solar photovoltaic system at a higher education institution in Illinois, USA. *AIMS Energy*, *5* (1), 54–62.

Kobayashi, T., Kanematsu, H., Hashimoto, R., Morisato, K., Ohashi, N., Yamasaki, H. & Takamiya, S. (2013). Study on environment and energy using belonging materials. *International Journal of Sustainable Development & World Policy*, *2* (4), 50–58.

Ma, Y. X. & Yu, C. (2020). Impact of meteorological factors on high-rise office building energy consumption in Hong Kong: from a spatiotemporal perspective. *Energy and Buildings*, *228*, 110468.

Martins, F., Felgueiras, C., Smitkova, M. & Caetano, N. (2019). Analysis of fossil fuel energy consumption and environmental impacts in European countries. *Energies*, *12* (6), 964.

Mohammad, S., Zakaria, R., Omar, W., Abd Majid, M. Z., Saleh, A. L., Mustaffar, M., Zin, R. M. & Jainudin, N. (2013). Potential of solar farm development at UTM campus for generating green energy. *Applied Mechanics and Materials*, *479–480*, 553–558.

Payam, F. & Taheri, A. (2018). Challenge of fossil energy and importance of investment in clean energy in Iran. *Journal of Energy Management and Technology*, *2* (1), 1–8.

Saidur, R., Hasanuzzaman, M., Yogeswaran, S., Mohammad, H. A. & Hossain, M. S. (2010). An end-use energy analysis in a Malaysian Public Hospital. *Energy*, *35* (12), 4780–4785.

Saudi, M. H. M. (2019). The role of renewable, non-renewable energy consumption and technology innovation in testing Environmental Kuznets Curve in Malaysia. *International Journal of Energy Economics and Policy*, *9* (1), 299–307.

Song, Y., Ji, Q., Du, Y. J., & Geng, J. B. (2019). The dynamic dependence of fossil energy, investor sentiment and renewable energy stock markets. *Energy Economics*, *84*, 104564.

Sustainable Energy Development Authority Malaysia [SEDA] (2009). *National renewable energy policy and action plan.* Kuala Lumpur: SEDA.

Umar, M., Ji, X., Kirikkaleli, D. & Alola, A. (2021). The imperativeness of environmental quality in the United States transportation sector amidst biomass-fossil energy consumption and growth. *Journal of Cleaner Production*, *285*, 124863.

U.S. Energy Information Administration [EIA] (2018). *World energy balances: overview*. Retrieved from: https://webstore.iea.org/world-energy-balances-2018-overview [accessed 23.08.2022].

U.S. Energy Information Administration [EIA] (2019). *Southeast Asia Energy Outlook 2019*. Retrieved from: https://www.iea.org/reports/southeast-asia-energy-outlook-2019 [accessed 23.08.2022].

U.S. Energy Information Administration [EIA] (2020). *Electricity information: overview*. Retrieved from: https://www.iea.org/reports/electricity-information-overview [accessed 23.08.2022].

U.S. Energy Information Administration [EIA] (2022). *Electricity explained*. Retrieved from: https://www.eia.gov/energyexplained/electricity/electricity-and-the-environment.php [accessed 23.08.2022].

Summary

Exploring acceptance on benefit of solar farm implementation in Malaysia. Implementation of solar farms to generate electricity is still low in Malaysia, where only 1%, or 227.5 MW of the total installed electrical capacity in Malaysia was produced from solar PV installations in 2016. Renewable energies, e.g. solar energy, have been adopted in many countries to generate electricity as a response to global environment issues. The aim of this study is to determine financial opportunities and benefits of solar farm implementation towards the society and the environment. Data were acquired through a literature review and questionnaire survey that was conducted among the respondents that are directly involved in the solar energy. Long-term financial savings constitute the most identified financial opportunities for the implementation of solar farms in generating clean electricity. Implementation of solar farms will encourage more businesses related to solar energy to be established in the country and will lead to new business opportunities. Solar farms are far better than conventional fossil fuel power plants in terms of the environmental effect and also reduce the health effects on the society during the electric generating process.

Instruction for Authors

The journal publishes in English languages, peer-reviewed original research, critical reviews and short communications, which have not been and will not be published elsewhere in substantially the same form. Author of an article is required to transfer the copyright to the journal publisher, however authors retain significant rights to use and share their own published papers. The published papers are available under the terms of the principles of Open Access Creative Commons CC BY-NC license. The submitting author must agree to pay the publication charge (see Charges).

The author of submitted materials (e.g. text, figures, tables etc.) is obligated to restricts the publishing rights. All contributors who do not meet the criteria for authorship should be listed in an Acknowledgements section of the manuscript. Authors should, therefore, add a statement on the type of assistance, if any, received from the sponsor or the sponsor's representative and include the names of any person who provided technical help, writing assistance, editorial support or any type of participation in writing the manuscript.

Uniform requirements for manuscripts

The manuscript should be submitted by the Open Journal System (OJS) at https://srees.sggw.edu.pl/about/submissions. All figures and tables should be placed near their reference in the main text and additionally sent in a form of data files (e.g. Excel, Visio, Adobe Illustrator, Adobe Photoshop, CorelDRAW). Figures are printed in black and white on paper version of the journal (color printing is combined with an additional fee calculated on a case-by-case basis), while on the website are published in color.

The size of the manuscript should be limited up to 10 pages including overview, summary, references and figures (the manuscript more than 13 pages is unacceptable); Please set the text format in single column with paragraphs (A4 paper format), all margins to 25 mm, use the font Times New Roman, typeface 12 points and line spacing one and half.

The submitted manuscript should include the following parts:

- name and SURNAME of the author(s) – up to 5 authors
- affiliation of the author(s), ORCID Id (optional)
- title of the work
- key words
- abstract (about 500 characters)
- text of the paper divided into: Introduction, Material and Methods, Results and Discussion, Conclusions, References and Summary
- references in APA style are listed fully in alphabetical order according to the last name of the first author and not numbered; please find the details below
- post and mailing address of the corresponding author:

  Author's address:
  Name, SURNAME
  Affiliation
  Street, number, postal code, City
  Country
  e-mail: adress@domain

- Plagiarism statement (https://srees.sggw.edu.pl/copyright)

Reference formatting

In the Scientific Review Engineering and Environmental Sciences the APA 6th edition style is used.

Detailed information

More information can be found: https://srees.sggw.edu.pl